UNIVERSITÉ LAVAL

Découplage de la proprioception et de l'actionnement des manipulateurs robotiques sériels comme court-circuit au critère de raideur élevée

Thèse

Xavier Garant

Doctorat en génie mécanique
Philosophiæ doctor (Ph. D.)

Québec, Canada

Découplage de la proprioception et de l'actionnement des manipulateurs robotiques sériels comme court-circuit au critère de raideur élevée

Thèse

Xavier Garant

Sous la direction de:

Clément Gosselin, directeur de recherche

Résumé

Cette thèse présente une méthode de proprioception alternative pour les manipulateurs robotiques sériels. Cette méthode ne dépend pas de la position des actionneurs et ne nécessite donc pas d'hypothèse de corps rigides. Cela permet, d'une part, d'envisager un paradigme différent pour la conception de robots légers et flexibles, mieux adaptés aux applications d'interaction physique-humain robot. D'autre part, cela permet de transformer la déformation de la structure du robot, habituellement perçue comme un désavantage, en un outil de détection des intentions de l'usager pendant une tâche d'interaction.

Le premier chapitre présente la conception du système de rétroaction non colocalisée pour manipulateurs sériels flexibles. Le dispositif est une chaîne sérielle et passive d'encodeurs et de membrures légères, disposée en parallèle avec le manipulateur. Ce bras de mesure découple la proprioception du manipulateur de ses actionneurs en fournissant de l'information sur la pose réelle de son organe terminal, qui tient compte de la flexibilité des membrures et des articulations. Un schéma de commande dans l'espace des tâches, mettant à profit cette rétroaction additionnelle, est conçu et testé en simulation. Finalement, les résultats de simulation sont validés à l'aide d'un manipulateur expérimental léger à trois degrés de liberté, équipé d'un bras de mesure à cinq degrés de liberté.

Le second chapitre présente une méthode permettant l'interaction physique humain-robot de façon intuitive avec les manipulateurs flexibles grâce au système de mesure précédemment mentionné. En mesurant la déviation de l'organe terminal par rapport à la base, toute la structure du manipulateur devient une interface potentielle d'interaction, peu importe si la flexion provient des membrures ou des articulations. Le schéma de commande proposé est basé sur un simple asservissement des vitesses articulaires et ne requiert que la connaissance de la matrice jacobienne rigide du manipulateur. L'approche est validée en simulation sur un modèle simplifié, ainsi qu'expérimentalement sur un prototype physique de robot sériel à trois degrés de liberté avec articulations et membrures flexibles.

Le troisième et dernier chapitre présente une généralisation des concepts reliés aux actionneurs a élasticité en série (*series elastic actuators*, SEA) pour la commande en force de manipulateurs à articulations et membrures flexibles à plusieurs degrés de liberté. En utilisant la mesure de la pose de l'organe terminal, toute la structure d'un manipulateur peut être consi-

dérée comme un SEA. Une approche par éléments de raideur localisés (*lumped stiffness*) est proposée pour modéliser la raideur du manipulateur. Ce faisant, les schémas de commande développés pour l'interaction physique humain-robot avec les SEA peuvent être transposés à la commande en impédance de manipulateurs flexibles. Un résultat connu sur la raideur maximale passivement réalisable avec les SEA à un degré de liberté est généralisé pour les structures flexibles à plusieurs degrés de liberté. Finalement, les schémas de commande proposés sont validés expérimentalement.

Abstract

This thesis presents an alternative proprioception method for flexible serial robotic manipulators. This method is independent from the actuators and requires no rigid body assumption. This enables, on one hand, a different design paradigm for lightweight and flexible robots, that are better suited for physical human-robot interaction (pHRI) applications. On the other hand, this allows structural deflection, usually perceived as a disadvantage, to be transformed into a tool enabling user intent detection during an interaction task.

The first chapter presents the design of a non-collocated feedback system for flexible serial manipulators. The device is a passive serial chain of encoders and lightweight links, mounted in parallel with the manipulator. This measuring arm effectively decouples the manipulator's proprioception from its actuators by providing information on the actual end-effector pose, accounting for both joint and link flexibility. With this additional feedback, a task-space position controller is devised and tested in simulation. Finally, the simulation results are validated with an experimental 3-DoF lightweight manipulator prototype equipped with a five-joint measuring arm.

The second chapter presents a method enabling intuitive pHRI with flexible robots using an end-point sensing device. The device is a passive serial chain of encoders and lightweight links, mounted in parallel with the manipulator. By measuring the deflection of the end-effector relative to the base, the whole body of the manipulator becomes a potential interaction interface, whether the compliance stems from the links or the joints. The proposed control scheme is a simple joint velocity control that only requires knowledge of the rigid-body Jacobian matrix of the manipulator. The approach is validated both in simulation on a simplified model and experimentally on a physical 3-DoF flexible-link flexible-joint serial robot.

The third and final chapter proposes a task-space generalisation of series elastic actuation concepts for flexible-link flexible-joint robots with any number of degrees of freedom. Using end-point sensing, the whole body of the flexible manipulator can effectively be considered a task-space series elastic actuator (SEA). A lumped stiffness approach based on the virtual joint method is used to establish an elastostatic model of the flexible manipulator. A simple methodology is proposed in order to identify the elastostatic model parameters. This allows force control of the robot, with notable applications in physical human-robot interac-

tion through admittance and impedance control schemes. A known result on the maximum passively renderable stiffness for single degree-of-freedom (dof) SEAs is generalised to n-dof flexible structures, providing bounds on the renderable stiffness matrix that apply to any causal controller. Finally, the task-space control schemes derived from the SEA literature are implemented and validated on a 3-dof flexible-link flexible-joint manipulator prototype.

Table des matières

Liste des tableaux

Liste des figures

Je le regardais, les mains dans les poches, et je lui ai
souri mais je ne lui ai rien dit parce qu'à quoi bon,
c'était un jeune mec de trente ans qui avait
encore tout à apprendre.

Momo, *La vie devant soi* (Romain Gary)

Remerciements

La machine tiédit. L'heure est au bilan. Par chance, je n'ai jamais eu de penchant particulier pour la mélancolie. J'aime par ailleurs le kitsch des remerciements.

À Clément, avec le recul que cela commande, je me permets de décerner l'un des titres les plus honorables qui soient, à hauteur d'homme : celui de mentor. Il n'est pas donné à tous de rencontrer une telle figure et l'on ne peut que se réjouir de ce coup du sort. C'est une chance inouïe que d'avoir pu compter sur ton expérience, ta passion et ton infatigable bonne humeur au cours de ces sept années de stage, de maîtrise et de doctorat. Ces dernières ont été ponctuées de ce qui s'apparentait, pour moi, à de véritables sauts dans l'inconnu, qui n'étaient pas sans donner le vertige. Je réalise aujourd'hui que dans ces moments charnières, tu n'as jamais manqué une occasion de m'encourager. Un rien parfois, quelques mots, mais qui auraient pu en valoir mille. Pour cela, et pour tant d'autres choses, je te dis autant de fois merci.

Merci à Simon, sans qui je n'aurais pu aspirer à réaliser ne serait-ce qu'une fraction du travail accompli ces quatre dernières années. Au creux de la pandémie, tu as été la pierre angulaire de la complexe opération que devenait soudainement la réalisation d'un doctorat à forte dimension expérimentale.

Un mot également pour Alexandre et Philippe, qui se sont, entre autres, toujours prêtés au jeu des références et des recommandations. Sans vous, je me dois de le souligner, le champ des possibles se serait drôlement rétréci. Trouvez, dans ce simple remerciement, toute l'estime que je porte pour ceux qui, comme vous, s'efforcent d'ouvrir des horizons.

Je tiens à souligner l'hospitalité de Jérémie, Gabrielle, Déric et Mariane. Merci d'avoir permis à cette thèse de prendre vie.

Karolane, merci d'être ma complice, de me faire rire et d'être une source de bonheur intarissable.

Famille, amis et collègues, votre contribution a cela de paradoxal qu'elle est probablement la plus importante, tout en étant la plus difficile à décrire en termes justes. Certaines choses se passent de mot. C'est peut-être ce qui fait leur beauté. Soyez convaincus qu'il y a un peu de

vous en ces lignes et pour tous les souvenirs accumulés, mais aussi pour ceux à venir, je vous remercie du fond du coeur.

Enfin, cher lecteur, merci de faire vivre cet ouvrage. Sachez que chaque lettre de chaque mot en ces pages y a été couchée avec le soin dont seul un esprit humain sait faire preuve. L'avenir saura nous informer du bien-fondé de cette remarque. Dans l'intervalle, je vous prie de considérer cette attention comme une marque de respect à votre égard.

Avant-propos

Le présent ouvrage est écrit suivant la forme d'une thèse par articles. Chaque chapitre représente donc un article scientifique rédigé en cours d'études, dans le cadre de la recherche entreprise pour l'obtention du grade. Les informations relatives à chaque article sont présentées ci-dessous :

Chapitre 1

Titre : *Non-collocated Proprioceptive Sensing for Lightweight Flexible Robotic Manipulators.*
Type d'article : Article de périodique, IEEE/ASME Transactions on Mechatronics.
État de publication : Publié le 11 avril 2023. DOI : 10.1109/TMECH.2023.3263108
Contribution : Auteur principal. Réalisation des travaux et rédaction de l'article.
Coauteurs : Clément Gosselin. Supervision des travaux et révision de l'article.
Modification : Aucune.

Chapitre 2

Titre : *Whole-body Intuitive Physical Human-Robot Interaction with Flexible Robots Using Non-collocated Proprioceptive Sensing.*
Type d'article : Article de périodique, IEEE Robotics and Automation Letters.
État de publication : Accepté le 3 janvier 2024 (première soumission le 11 avril 2023).
Contribution : Auteur principal. Réalisation des travaux et rédaction de l'article.
Coauteurs : Clément Gosselin. Supervision des travaux et révision de l'article.
Modification : Aucune.

Chapitre 3

Titre : *Generalising series elastic actuation to n-dof flexible-link flexible-joint robot control using end-point sensing.*

Type d'article : Article de périodique, International Journal of Robotics Research.

État de publication : Soumis le 20 décembre 2023.

Contribution : Auteur principal. Réalisation des travaux et rédaction de l'article.

Coauteurs : Clément Gosselin. Supervision des travaux et révision de l'article.

Modification : Aucune.

Introduction

Contexte et problématique

Plusieurs grands principes de la robotique collaborative sont en opposition directe avec les paradigmes qui ont toujours orienté la robotique classique. En effet, cette science a mûri au 20^{e} siècle dans les environnements très structurés du monde manufacturier. On peut donc s'attendre à ce que d'un tel choc d'idées surgissent des remises en question fondamentales, dont les retombées se traduisent souvent en avenues de recherche intéressantes.

En l'occurrence, la collaboration humain-robot implique une forte composante d'interaction entre l'opérateur et la machine, de laquelle découle forcément un partage de la zone de travail. Dans ce contexte, il devient essentiel de trouver des moyens d'assurer la sécurité de l'être humain et on retrouve, dans la littérature scientifique et en industrie, différentes stratégies pour y parvenir. À l'heure actuelle, l'avenue la plus commune consiste essentiellement à appliquer un facteur d'échelle aux robots classiques pour ainsi réduire leur taille et leur charge utile. On réduit aussi leur vitesse de déplacement, de façon à diminuer l'énergie cinétique et permettre un certain temps de réaction aux humains. Cette tendance est très présente en industrie, où elle est parfois jumelée à d'autres solutions de *commande*, ou logicielles, mettant à profit des capteurs additionnels pour détecter les contacts, comme des capteurs d'efforts ou des revêtements tactiles.

Dans le présent ouvrage, il est plutôt proposé d'explorer une idée innovante permettant d'améliorer les qualités *intrinsèques* des manipulateurs robotiques dans un contexte d'interaction humain-robot. Notamment, on propose de se départir du paradigme de raideur élevée qui a toujours orienté la conception des robots jusqu'ici.

Délaisser le critère de raideur élevée permet, d'abord, d'envisager des robots beaucoup plus légers. Une masse réduite entraîne, comme pour une vitesse réduite, un réduction de l'énergie cinétique du robot. Il en résulte donc un niveau de danger moindre lors d'impacts. Cependant, réduire la masse du robot comporte d'autres avantages intéressants. D'une part, ceci permet d'augmenter « mécaniquement » la bande passante du système, qui est un critère de performance primordial pour l'interaction humain-robot. D'autre part, il n'est pas exagéré de croire qu'une masse suffisamment réduite des membrures du robot pourrait permettre l'utili-

sation de moteurs à entraînement direct, ou de réducteurs de vitesse à faible rapport. Enfin, la flexibilité structurelle d'un robot permet de découpler l'inertie réflétée à son organe terminal de l'inertie (généralement grande) de ses actionneurs.

Le principal problème est que le modèle mathématique d'un manipulateur robotique, se basant uniquement sur la position des actionneurs articulaires, avec comme hypothèse de base que les membrures sont des corps rigides, n'est plus valide. En effet, dans le cas d'un manipulateur flexible, la position réelle de l'organe terminal diffère de façon significative de la position théorique prévue par le modèle rigide. Par ailleurs, un modèle qui tient compte des flexibilités structurelles est beaucoup plus complexe et difficile à mettre en oeuvre en pratique. Le critère de raideur élevée est donc dominant dans la conception de robots sériels, afin de respecter les exigences de précision et de répétabilité inhérentes à un vaste éventail de tâches robotisées.

Objectif des travaux de recherche

L'objectif de la recherche est donc d'explorer un nouveau paradigme de conception des robots sériels délaissant le critère de raideur élevée au profit d'autres critères tels que la masse en mouvement ainsi que la bande passante d'interaction, tout en maintenant autant que possible la fonctionnalité des manipulateurs classiques.

Objectifs spécifiques

1. Concevoir une méthode de mesure de la pose (position et orientation) de l'organe terminal du robot qui soit indépendante des articulations.
2. Concevoir une méthode de commande du mouvement du robot adaptée à cette nouvelle stratégie de mesure.
3. Concevoir une méthode de commande pour l'interaction physique humain-robot adaptée à cette nouvelle stratégie de mesure.

Méthodologie et plan de la thèse

La méthodologie employée pour atteindre les objectifs se présente comme suit.

D'abord, le chapitre 1 traite des objectifs 1 et 2 et, d'un point de vue global, jette les bases du projet de recherche. On y retrouve donc

— une revue de la documentation scientifique pertinente pour l'étude de solutions alternatives de mesure de la pose des robots sériels ;
— une formalisation de la cinématique du problème ;
— une présentation de la solution de mesure retenue, de sa conception et de sa fabrication ;

— l'élaboration d'un schéma de commande des mouvements du robot dans l'espace des tâches mettant à profit la nouvelle solution de mesure ;
— la présentation détaillée du montage expérimental utilisé pour le reste des travaux de recherche ;
— la validation expérimentale du schéma de commande en vitesse proposé.

Ensuite, le chapitre 2 traite de l'objectif 3 et, plus spécifiquement, explore l'idée d'utiliser la mesure de la déformation du robot pour détecter l'intention de l'utilisateur. On y présente une méthode permettant à un humain de guider un robot flexible par des mouvements libres en interagissant physiquement avec celui-ci. On y retrouve donc

— les hypothèses simplifiant l'étude du robot ;
— l'étude d'un schéma de commande basé sur la mesure de déformation du robot ;
— la validation du schéma de commande en simulation ainsi qu'à l'aide du montage expérimental.

Le chapitre 3 traite également de l'objectif 3, mais présente une méthode permettant d'imposer un comportement dynamique lors de l'interaction. On y retrouve

— une revue de la documentation sur l'asservissement de structures flexibles, notamment des actionneurs a élasticité en série (*series elastic actuators*, SEA) ;
— une analogie entre le système à l'étude et les SEA ;
— une méthologie de modélisation des flexibilités du robot ;
— la présentation de schémas de commande adaptés des SEA pour l'interaction physique ;
— la validation expérimentale du schéma de commande.

Enfin, le présent ouvrage se conclut sur une synthèse des travaux de recherche entrepris et des résultats obtenus, puis aborde les futures avenues de recherche.

Chapitre 1

Non-Collocated Proprioceptive Sensing for Lightweight Flexible Robotic Manipulators

1.1 Résumé

Cet article présente la conception d'un système de rétroaction non colocalisée pour manipulateurs sériels flexibles. Le dispositif est une chaîne sérielle et passive d'encodeurs et de membrures légères, disposée en parallèle avec le manipulateur. Ce bras de mesure découple la proprioception du manipulateur de ses actionneurs en fournissant de l'information sur la pose réelle de son organe terminal. Cette mesure tient donc compte de la flexibilité des membrures et des articulations. La redondance cinématique de la chaîne de mesure permet une opération sécuritaire dans un contexte d'interaction physique humain-robot. Un modèle d'erreur simple est présenté afin de valider la pertinence du système proposé pour des applications de commande robotique. La faisabilité technique du dispositif est d'abord démontrée par la fabrication d'un assemblage articulation-encodeur puis d'un prototype de bras de mesure à géométrie plane. Grâce à cette rétroaction additionnelle, un schéma de commande dans l'espace des tâches est conçu et testé en simulation. Finalement, les résultats de simulation sont validés à l'aide d'un manipulateur expérimental léger à trois degrés de liberté, équipé d'un bras de mesure à cinq degrés de liberté.

1.2 Abstract

This paper presents the design of a non-collocated feedback system for flexible serial manipulators. The device is a passive serial chain of encoders and lightweight links, mounted in parallel with the manipulator. This measuring arm effectively decouples the manipulator's proprioception from its actuators by providing information on the actual end effector pose,

accounting for both joint and link flexibility. The kinematic redundancy of the measuring chain allows for safe operation in the context of human-robot interaction. A simple yet effective error model is introduced to assess the suitability of the proposed sensor system in the context of robotic control. The practicality of the device is first demonstrated by building a physical joint-encoder assembly and a simplified planar measuring arm prototype. With this additional feedback, a task-space position controller is devised and tested in simulation. Finally, the simulation results are validated with an experimental 3-DoF lightweight manipulator prototype equipped with a five-joint measuring arm.

1.3 Introduction

It is a well known fact that the classical manipulator architecture, with collocated proprioceptive sensors and actuators, rapidly faces serious challenges as soon as flexible components are introduced in its structure (Kiang et al., 2015). This appears as a considerable inconvenience in the context of modern robotic applications. Notably, for the purpose of physical human-robot interaction (pHRI), lightweight (and flexible) robots are desirable for safety reasons.

Indeed, a typical manipulator's only means of measuring its own end effector pose is through the feedback of its actuators' displacement. The pose can theoretically be reconstructed from sensory input, assuming both rigid links and joints. While benign in appearance, this assumption has been guiding robot design for decades. In order for the physical manipulator to conform to this principle, stiffness is one of the prime design criteria. In consequence, the robot must carry additional mass whose sole purpose is to ensure adequate link stiffness. Yet, in the context of interactive applications with humans, mobile mass has been known for some time to carry considerable drawbacks (Haddadin et al., 2008; Haddadin and Croft, 2016; Steinecker et al., 2022).

To move this mass with precision, stiff actuators with high transmission ratios are required. This comes at the cost of a very high reflected inertia (García et al., 2020) and low bandwidth. One possible improvement is to relocate the motors (which make up a major part of the total mass) at the base of the robot (De Santis et al., 2008). In recent years, there has also been much research interest in reducing transmission ratios to direct-drive (Wen et al., 2021) or quasi-direct drive levels (Gealy et al., 2019) to improve the inherent safety of manipulators. At the same time, others have looked into introducing compliance in the manipulator structure to reduce the reflected inertia and reflected stiffness (Toxiri et al., 2018).

In general, control strategies for flexible manipulators can be divided in two main categories: open-loop model-based control, or closed-loop sensor-based control (Kiang et al., 2015). In this case, the terms open-loop or closed-loop implicitly refer to whether deflection feedback is used or not. Open-loop control of flexible manipulators has been largely studied and

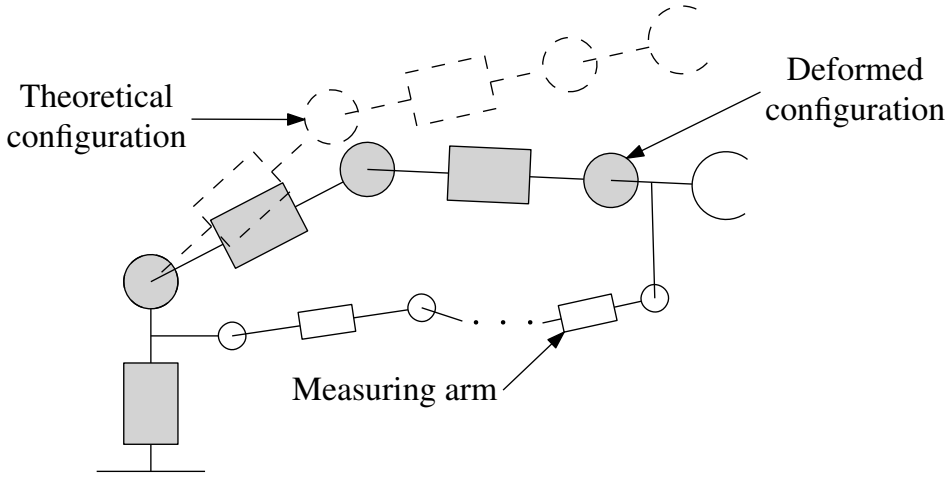

Figure 1.1 – Schematic representation of a flexible manipulator in a theoretical configuration (dashed white), deformed configuration under load (solid grey) and measuring arm (solid white).

is known to be a complex problem, owing to the very nonlinear and non-minimum phase dynamics (Cannon and Schmitz, 1984; Sayahkarajy et al., 2016; Berger and Lanza, 2021). Thus, this paper focuses on feedback-based approaches to flexible manipulator control.

Common feedback options for deflection sensing in manipulators include strain gauges, accelerometers, and vision systems or range sensors. Strain gauges provide direct information on link deformation, but commonly face challenges related to noise and thermal sensitivity (Feliu-Talegon and Feliu-Batlle, 2021). In addition, strain gauges only measure the local deformation of single *links*, and cannot compensate alone for flexible *joints*. Accelerometers, on the other hand, can provide 'total' deformation information by measuring the acceleration at various points along the manipulator (Staufer and Gattringer, 2012). However, as it is well known, these sensors are also prone to noise and biases, complicating the extraction of position and velocity signals (Subedi et al., 2022). Finally, vision systems and range sensors can provide precise deflection measurements of both flexible link and flexible joint manipulators (Hussein, 2015). They however come at the cost of additional delays in the control loop and reduced bandwidth, while also requiring more involved calibration methods (Oliveira et al., 2020). Moreover, vision-based control involves additional abstraction layers dedicated to image processing and feature extraction (Sahu et al., 2020).

In this paper, a sensor system in the form of a passive measuring arm (as illustrated schematically in Figure 1.1) is further developed, with a focus on pHRI applications. The proposed system only relies on encoder signals and therefore does not require computer vision, strain gauges or inertial measurement units. The intent of this system is to provide fast and reliable end effector deflection information, with minimal interference in the interaction between the manipulator and human operator. Using terminology from the closely related field of soft

robotics, the proposed sensor system could therefore be considered a 'soft sensor', according to the definition in Chen et al. (2017).

Some patents have conceptually explored the idea of adding a measuring arm in parallel between manipulator links (Flemming, 1977; Slocum, 1984; Grädener and Rokeach, 2019), but fall short in regard to the practicality of such an undertaking. One such practical consideration lies in assessing the precision that can be expected from the sensor system. This problem was first tackled mathematically in Gong (2005), which found that a simulated measuring arm could theoretically return nanometre level measurements, given very high precision joint encoders. These results were however never experimentally validated and therefore also minimised potential practical pitfalls such as interference between the manipulator and measuring arm, or the combined singularity loci of the integrated robotic unit.

To the best of the author's knowledge, the first and only practical implementation of a measuring arm in the literature was in Merckaert et al. (2018). Merckaert *et al.* introduced the idea of using tip deflection sensing with the intent to design the manipulator based on strength rather than stiffness. They aptly proved that the deformation can be compensated for, at least in the direction of gravity. They also made a strong case for the safety improvements that this method could yield by reducing the mass of the manipulator. In its current state, however, their sensor system can only tolerate and detect in-plane (2D) tip deflection, thus ignoring out-of-plane forces or torsion inducing moments.

In light of the scarce literature, this paper aims to bring the state of the art on this concept closer to a fully functional and practical sensor system. To this end:

— A basic kinematic structure is proposed for the integrated manipulator-measuring arm unit. Kinematic constraints specific to this application are outlined and design guidelines are provided.
— Kinematic redundancy is leveraged to circumvent otherwise challenging kinematic problems, while also making the device inherently safe for human interaction.
— With its higher degree of freedom (DoF) count, the sensor system is intended to measure the deviation of the robot's end effector pose in all directions.
— A mathematical framework based on differential kinematics is proposed in order to characterise the device's precision. This assessment proves that the pursuit of this design is relevant considering the current technological means and expected orders of magnitude of manipulator reach and payload.

This paper is structured as follows. Section 1.4 introduces the proposed kinematic structure of the integrated robotic unit comprising the manipulator and measuring arm. Section 1.5 then briefly outlines the forward kinematics of the measuring arm. In Section 1.6, a mathematical model based on differential kinematics is proposed to assess the precision of the

device. Section 1.7 discusses the practical requirements and constraints that guide the design process of the physical sensor unit. In Section 1.8, a practical method is devised to simultaneously assemble and calibrate the unit. A working planar measuring arm prototype is then experimentally validated in Section 1.9. A position control scheme that takes advantage of the sensor device's feedback is introduced in Section 1.10. Section 1.11 then shows simulation results using this controller on a virtual flexible manipulator. Section 1.12 presents the design of an integrated robotic unit prototype consisting of a 3-DoF lightweight manipulator equipped with a measuring arm. The experimental validation of this proof of concept is finally discussed in Section 1.13. Conclusions are drawn in Section 1.14.

1.4 Kinematic Architecture

As observed in the literature, in its simplest form, the proposed integrated robotic unit comprises a serial manipulator and a measuring arm extending from the *fixed* base to the end effector of the manipulator, in parallel.

Let us define A and B, the workspace domains of the manipulator and the measuring arm, respectively. Then, in order for the integrated unit to operate freely, the following condition must be met:

$$B \supset A \tag{1.1}$$

which is more restrictive than what is proposed in Gong (2005). Indeed, in this application, A and B cannot be equal. Practically, the outer limits of B correspond to a singular configuration where the measuring arm is completely extended. Theoretically, in this configuration, external forces would exceptionally be able to generate undesirable internal efforts in the passive measuring arm.

If condition (1.1) is met, the workspace domain C of the integrated unit is then

$$C = A \cap B \Rightarrow A. \tag{1.2}$$

However, in order to determine the real usable workspace, the singular domain of the integrated unit must be subtracted from C. The singular domain, noted $\overline{C}$, is given as

$$\overline{C} = \overline{A} \cup \overline{B} \tag{1.3}$$

where $\overline{A}$ and $\overline{B}$ are the singular domains of the manipulator and measuring arm, respectively.

Additionally, one must also consider the workspace regions that cannot be reached due to interference between the manipulator and measuring arm. Mathematically characterising these interference regions is not trivial.

Concretely, condition (1.1) also implies that the Cartesian DoF count of the measuring arm must be greater than or equal to the number of DoFs of the manipulator's end effector.

However, while this is true in the rigid case, additional conditions apply when considering a flexible manipulator. Indeed, with any number of flexible links and joints, every link along the manipulator can move in six spatial dimensions relative to the base. Therefore, the number of joints m of the measuring arm must meet the following condition:

$$m \geq 6 - k \tag{1.4}$$

where k is the number of DoFs allowed by the connection between the tip of the measuring arm and the manipulator's end effector. For instance, a rigid connection would minimally require a 6-joint measuring arm, while a spherical joint connection would minimally require a 3-joint measuring arm, irrespective of the manipulator's architecture. Of course, in this case a spherical connection would only allow the measurement of position deviations, ignoring orientation error.

It is the authors' belief that the aforementioned non-trivial kinematic constraints are one of the main reasons holding back the development of such a sensor system dedicated to flexible manipulators. Therefore, it is proposed to circumvent these issues with the following relaxations:

— In the context of pHRI, minimising moving mass is critical while stationary mass generally does not pose any risk. Therefore, the fixed base link l_0 and first joint j_1 of the manipulator can be made arbitrarily massive, ergo arbitrarily rigid.

— In accordance with the preceding statement, the base of the measuring chain can be attached to the first moving link l_1 of the robot, as close as possible to joint j_1, without compromising accuracy or precision.

The resulting kinematic structure proposed for the integrated robotic unit is graphically represented in Figure 1.2. The benefit of this architecture is that it greatly reduces the risk of interference between the manipulator and measuring arm. Indeed, in this case the measuring arm does not span the first joint of the manipulator, which is generally responsible for the largest amplitude movements of the end effector.

To further mitigate the risk of interference, it is also proposed to take advantage of kinematic redundancy. Thus, condition (1.4) becomes

$$m > 6 - k. \tag{1.5}$$

This allows the measuring arm to conform to the manipulator in a situation where interference would typically occur. It also virtually prevents the measuring arm from reaching singular configurations, by providing alternative joint arrangements for every Cartesian pose. Moreover and perhaps even more importantly, this grants compliance to the measuring arm when interacting with humans and thus greatly reduces pinching or squeezing risks. The more redundant joints there are, the safer pHRI becomes with the integrated unit, the ideal case being a measuring arm that behaves somewhat like a chain or cable.

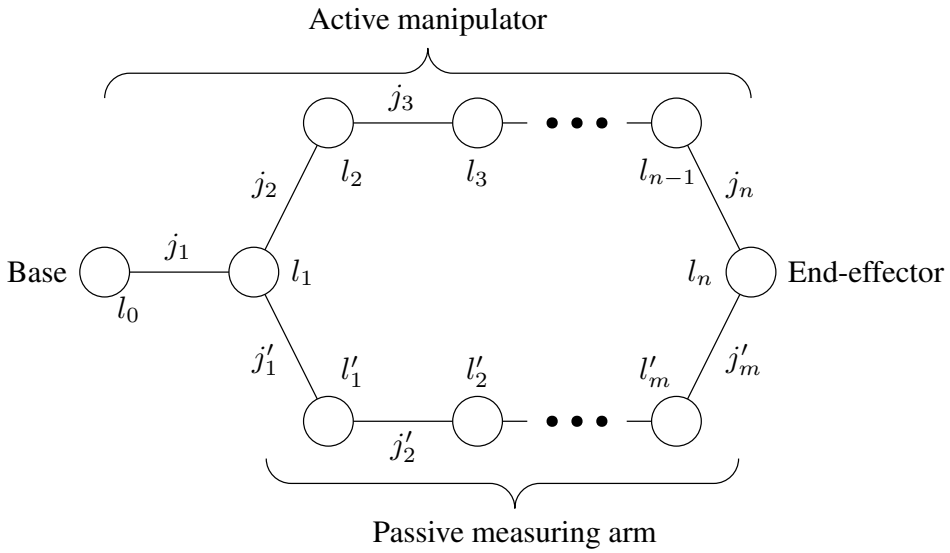

Figure 1.2 – Graph of the proposed kinematic structure for the robotic unit comprising a manipulator and a measuring arm. Bodies l_i are represented by nodes. Joints j_i are represented by edges.

1.5 Forward Kinematics

This section details the forward kinematics of the measuring chain. It is worth noting that for the purpose of controlling a robotic manipulator, the inverse kinematics of the passive measuring arm are irrelevant. Therefore, the inverse kinematics are omitted in this paper.

As a result of the assumptions presented in Section 1.4, the measuring chain's end point position in the fixed reference frame, noted $\mathbf{x}$, can be written as

$$\mathbf{x} = \mathbf{f}_k(\boldsymbol{\theta}, \boldsymbol{\phi}) \tag{1.6}$$

$$\mathbf{x} = \mathbf{c}_1 + \sum_{i=1}^{m} \mathbf{a}'_i \tag{1.7}$$

where $\mathbf{f}_k(\boldsymbol{\theta}, \boldsymbol{\phi})$ represents the forward kinematics, $\boldsymbol{\theta}$ is the array of joint positions and $\boldsymbol{\phi}$ stands for the Denavit-Hartenberg (D-H) parameters. Vector $\mathbf{c}_1$ is a slight modification of the classical D-H method and defines the position of the origin of frame $1'$ with respect to frame 1, expressed in the base reference frame (frame 1). Then, following D-H conventions, vector $\mathbf{a}'_i$ defines the position of the origin of frame $i'+1$ with respect to frame i', expressed in frame 1.

1.6 Kinematic Sensitivity Error Model

Establishing the error model of a sensor is crucial in assessing its suitability as a feedback device to be used in a control system. In this section, a simple but effective error model is derived, based on well-known serial manipulator equations.

in Gong (2005), the following first order Taylor expansion is introduced to model the kinematic error of the measuring arm:

$$\delta\mathbf{x} = \frac{\partial \mathbf{f}_k(\boldsymbol{\theta}, \boldsymbol{\phi})}{\partial \boldsymbol{\theta}} \delta\boldsymbol{\theta} + \frac{\partial \mathbf{f}_k(\boldsymbol{\theta}, \boldsymbol{\phi})}{\partial \boldsymbol{\phi}} \delta\boldsymbol{\phi} \tag{1.8}$$

where $\delta\mathbf{x}$ is the Cartesian position error and $\delta\boldsymbol{\theta}$ and $\delta\boldsymbol{\phi}$ are the errors on joint coordinates and D-H parameters, respectively. The method in Gong (2005) relies on deriving an analytic expression for $\delta\mathbf{x}$ by symbolically differentiating the terms in (1.8). This process can be tedious and increases in complexity with the number of DoFs, which are expected to be high in the case of the measuring arm.

1.6.1 Joint Error

Clearly, considering the serial architecture of the measuring arm, it can be observed that the first term on the right hand side of (1.8) is simply equivalent to the product of the Jacobian matrix $\mathbf{J}$ of the measuring arm, and a small joint displacement $\Delta\boldsymbol{\theta}$. Here, $\mathbf{J}$ is defined in the usual sense such that

$$\dot{\mathbf{x}} = \mathbf{J}\dot{\boldsymbol{\theta}} \tag{1.9}$$

or

$$\Delta\mathbf{x} \simeq \mathbf{J}\Delta\boldsymbol{\theta} \tag{1.10}$$

for small values of joint displacements $\Delta\boldsymbol{\theta}$ yielding small Cartesian displacements $\Delta\mathbf{x}$.

Moreover, by delving further into differential kinematics, the notion of kinematic sensitivity can be introduced to simplify the error analysis of the measuring arm. Many indices have been proposed in the literature in order to compare the performance of manipulator architectures. However, the kinematic sensitivity index, presented in Cardou et al. (2010), is of particular interest in the present case because it directly relates to the Cartesian resolution of the measuring chain.

The idea behind this index is to find compatible joint displacements $\Delta\boldsymbol{\theta}$ of unit ∞-norm that yield a global extremum of $\Delta\mathbf{x}$, given equation (1.10). Writing this problem in terms of dimensionally homogeneous arrays leads to

$$\sigma_{\omega,\infty} = \max_{\|\Delta\boldsymbol{\theta}\|_\infty = 1} \|\mathbf{J}_\omega \Delta\boldsymbol{\theta}\|_\infty = \|\mathbf{J}_\omega\|_\infty \tag{1.11}$$

$$\sigma_{x,\infty} = \max_{\|\Delta\boldsymbol{\theta}\|_\infty = 1} \|\mathbf{J}_x \Delta\boldsymbol{\theta}\|_\infty = \|\mathbf{J}_x\|_\infty \tag{1.12}$$

where $\sigma_{\omega,\infty}$ and $\sigma_{x,\infty}$ are the maximum magnitude rotation and displacement, respectively, and

$$\mathbf{J} \equiv \begin{bmatrix} \mathbf{J}_\omega \\ \mathbf{J}_x \end{bmatrix}. \tag{1.13}$$

Here, $\mathbf{J}_\omega$ and $\mathbf{J}_x$ are the Jacobian sub-matrices respectively associated with the rotational and translational coordinates. These matrices can be numerically computed for any given configuration of the measuring arm.

In fact, any p-norm can be used with this index. However, the ∞-norm is a direct consequence of the common assumption that in any given configuration, the joint displacements $\Delta\boldsymbol{\theta}$ can take any value in an interval bounded by $\pm\Delta\theta_{max}$. This statement is then directly equivalent to

$$\|\Delta\boldsymbol{\theta}\|_\infty \leq \Delta\theta_{max} \tag{1.14}$$

or

$$\|\Delta\boldsymbol{\theta}\|_\infty \leq 1 \tag{1.15}$$

with normalised units. Thus, if we consider

$$\Delta\theta_{max} = \sigma_\theta \tag{1.16}$$

where σ_θ is the encoder resolution in radians, we can extract physical meaning from (1.11) and (1.12). Indeed, when multiplying $\sigma_{x,\infty}$ or $\sigma_{\omega,\infty}$ with $\Delta\theta_{max}$, one finds the actual physical maximum rotation and position displacement, respectively Σ_ω and Σ_x, in coherent units:

$$\Sigma_\omega = \sigma_\theta\|\mathbf{J}_\omega\|_\infty \tag{1.17}$$

$$\Sigma_x = \sigma_\theta\|\mathbf{J}_x\|_\infty \tag{1.18}$$

This result is effectively equivalent to an upper bound on the Cartesian resolution of the system *in a given configuration*, since its physical interpretation is the maximum allowable end point displacement before any movement is registered by the proprioceptive sensors.

This information can then be used for instance, as a threshold to discriminate significant tip deflections from random noise when operating the robotic unit. Indeed, this method has the advantage that (1.17) and (1.18) can easily be numerically computed in real-time. This is also true for more complex kinematic architectures, whereas the method in Gong (2005) progressively becomes more involved with a higher DoF count.

While this is considered out of the scope of this paper, if necessary, various approaches can be taken to determine an average or *global* Cartesian resolution of the measuring arm. For instance, one can discretise the entire joint space or a subset of it, and loop over each array of joint values in either a predetermined or randomised fashion. This method however faces the limitation of a rapidly increasing computational cost, with the total number of arrays equal to d^n, where d is the number of discretisations and n is the number of joints. A perhaps more interesting avenue consists in taking into account the fact that the workspace of the measuring arm is constrained by the workspace of the robotic manipulator, plus any significant deformation of the manipulator. Thus, one can discretise the resulting subset of the original measuring arm workspace and compute the inverse kinematics for an arbitrary number of configurations at every selected point.

1.6.2 D-H Parameter Error

To avoid the derivation of the second term in (1.8), it is possible to measure the actual values of the D-H parameters. Thus, instead of defining manufacturing and assembly tolerances on these dimensions, we can assume their values to either be virtually exact, or having such small error that the second term in (1.8) is negligible in relation to the first term (Gong, 2005). One practical method for doing so is presented in Section 1.8.

1.7 Sensor System Design

In the following section, the principles guiding the mechanical and electronic design of the measuring arm are presented.

First and foremost, it is crucial to minimise the mass of the system. This ensures that the measuring arm has a negligible impact on the dynamics of the manipulator.

Second, the form factor of both the encoders and the links of the measuring arm must be small enough to allow adequate mobility. To limit the bulkiness of the system, the size of the joints was limited to a maximum diameter of 30 mm.

Third, the encoders must provide absolute positions. Indeed, because the measuring chain is redundant and its joints are not actuated, the usual process of zeroing incremental encoders by returning to a known configuration is impractical. Furthermore, the sensors must be carefully selected according to their resolution and accuracy. As discussed in Section 1.6, one can rely on differential kinematics in order to define the required joint resolution as a function of a desired Cartesian resolution.

Fourth, in order to avoid the introduction of delays in the control system, the sampling rate of the measuring arm as a whole must be equal to or greater than 1 kHz. From experience, the authors determined that such a rate is sufficient in the context of real-time control for most robotic applications.

The resulting design, which takes into account all of the above design constraints, is shown in Figure 1.3. The joints are made of ABS eyelets sandwiched between radial and axial ball bearings. A small aluminium shaft runs axially through the assembly. The shaft is threaded at one end to pre-constrain the bearings and ensure minimal axial play. The links between the joint assemblies are made of carbon fibre tubes that are bonded to the plastic eyelets. The joint assembly has a mass of 35 g. The carbon fibre tubes have a linear mass of 0.13 g/cm.

Finding commercially available sensors (encoders) that provide sufficient resolution while satisfying the desired form factor is not trivial. The sensors mounted on the joints are CUI AMT-21 14-bit absolute encoders. These encoders provide a good commercial solution with a high resolution relative to their small size. They have a short 100 μs position update time

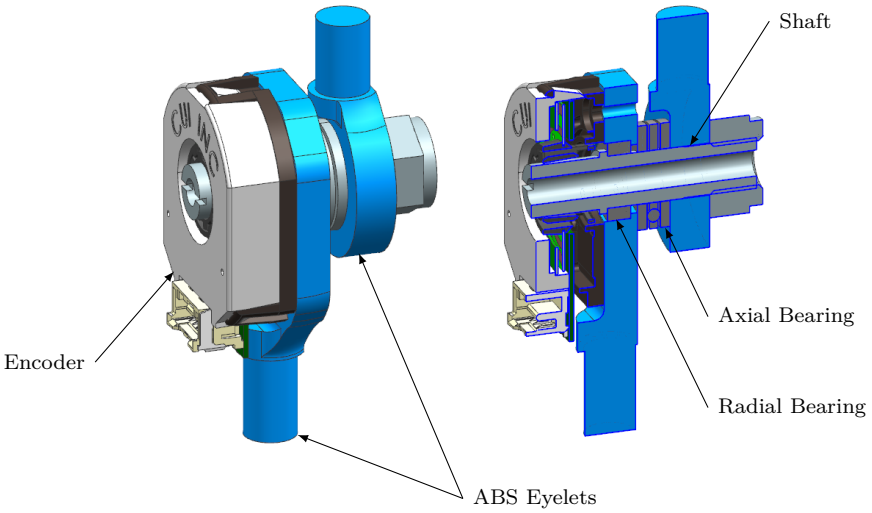

Figure 1.3 – Design of the joint-encoder assembly. 3D model (left) and section view (right).

and a fast 2 Mbps communication speed. The encoders communicate over an RS-485 bus. This simplifies cable routing (the bus is comprised of only four wires, power included) and provides basic protection against noise, through differential signalling. The data from all the encoders are collected and processed on the fly through one microcontroller and forwarded to the main CPU in under 300 μs end-to-end, which is fast enough for real-time control.

1.8 Build and Calibration

The absolute encoders at each joint of the measuring arm must be calibrated at least once before they can return relevant information. To accomplish this, one practical method is to build an assembly and calibration jig. An example of such a jig is presented in Figure 1.4. The jig consists of a metal plate with precisely machined holes into which pegs (precision dowel pins) are inserted. The joints of the measuring arm have through holes centred on their rotation axis with a diameter that matches the pegs. Thus, the joint assemblies can be fitted on the jig with minimal play, in the order of a few microns. Prior to assembly, the relative position of each hole in the jig is measured via a coordinate measuring machine (CMM). This directly translates to precise actual values of D-H parameters. Once the joints are assembled on the jig, carbon fibre tubes, which are used as the links of the measuring arm, are fitted and bonded in place. This completes the building process.

Since the relative position of each joint is known through the CMM measurements, the actual angular position of each joint can be computed. This allows the assembly jig to simultaneously serve as a calibration jig. Indeed, with the measuring arm assembled on the jig in a known configuration, each joint can be zeroed to a known value. This can also prove useful in case of a potential failure after which the measuring arm must be recalibrated.

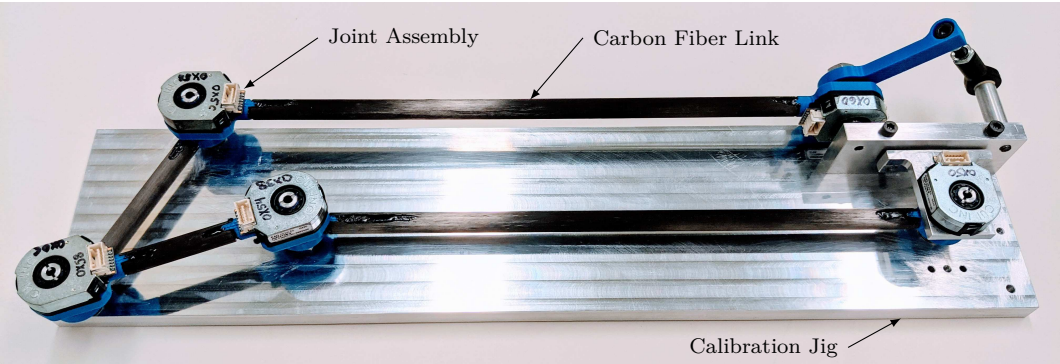

Figure 1.4 – Example of a 5-joint measuring arm prototype mounted on an assembly and calibration jig.

1.9 Experimental Validation of the Measuring Arm

In order to validate the practicality of the proposed sensor system concept and construction method, the prototype shown in Figure 1.4 was tested against ground truth measurements. Only the first four joints of the prototype were used to measure 2D positions. Thus, with four joints dedicated to a 2D position measuring task, this device has two redundant degrees of freedom. The link lengths of this prototype (in millimetres) are $\{l'_1 \quad l'_2 \quad l'_3 \quad l'_4\} = \{340 \quad 80 \quad 80 \quad 300\}$. These geometric parameters were chosen to match the dimensional order of magnitude of typical manipulators in the 5-7 kg payload range.

The experimental setup is shown in Figure 1.5. Concretely, the intent of this setup is to validate that the sensor system can accurately measure position variations. When taking measurements, the displacement of the end point of the kinematic chain is constrained to remain parallel to either the X or Y axis in the base reference frame. To ensure this constraint, the base of the kinematic chain is kept fixed to one edge of a precisely ground machinist square, while the end point is slid by hand along the other edge. During the tests, the redundant DoFs of the measuring arm are unconstrained and the links are free to move on the work surface. The ground truth displacement measurement is given by a plunger type dial indicator, which is also aligned on the precision square. The precision square has a maximum deviation of 0.003 mm, while the dial indicator has a rated accuracy of ± 0.03 mm.

The Cartesian position of the measuring arm's end point is computed using the sensor values and forward kinematics. After each test run, the difference between the final and initial positions is calculated, yielding the measured end point displacement.

The results are shown in Table 1.1. Five configurations were tested with the indicated measured displacements. The maximum resolution was computed in the initial configuration with the method shown in Section 1.6. It is worth restating that this number is an upper bound only achievable by considering an extreme case where every joint rotates by up to a full en-

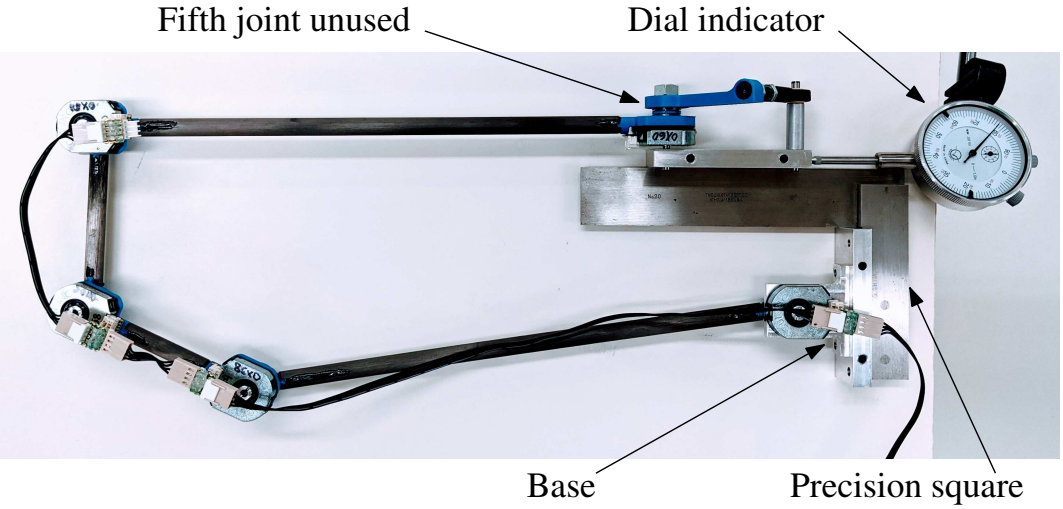

Figure 1.5 – Experimental setup with functional 4-DoF planar measuring arm (fifth joint unused). The end point is fixed to an aluminium block. The block slides along the precision square, constraining the movement of the end point.

coder resolution tick, moving the end point in an arbitrary direction. In the actual direction of movement, the precision of the measuring arm is in practice much higher. Still, the maximum resolution remained close to 0.4 mm in each configuration. This sub-millimetre resolution is adequate in the context of pHRI with a flexible manipulator, with expected displacements on the order of a few millimetres to a few centimetres. The measuring arm also proved to be accurate at measuring displacements in the centimetre range, with relative errors under 1%. A small displacement of 2-3 mm showed a slightly higher relative error. This is expected, as a constant uncertainty, such as a resolution error, yields a greater relative difference on a small measurement.

Table 1.1 – Experimental Validation of the 4-DoF Planar Measuring Arm

Initial Configuration [deg]	**Resolution [mm]**	**Displacement Δx [mm]**		**Error Norm [mm]**	
	Computed (Max)	Ground Truth	Measured	Absolute	Relative
$\boldsymbol{\theta} = [\ -7.18 \quad 31.23 \quad -122.10 \quad -81.19]^T$	0.42	$[-15.26 \quad 0]^T$	$[-15.4 \quad 0.4]^T$	0.42	0.94%
$\boldsymbol{\theta} = [\ \ 9.58 \quad 104.51 \quad 67.04 \quad -151.60]^T$	0.38	$[\ 22.88 \quad 0]^T$	$[\ 23.1 \quad 0.2]^T$	0.30	0.96%
$\boldsymbol{\theta} = [-77.41 \quad -48.31 \quad -53.39 \quad -90.56]^T$	0.41	$[\ 0 \quad 12.70]^T$	$[\ 0.1 \quad 12.8]^T$	0.14	0.78%
$\boldsymbol{\theta} = [-93.42 \quad 16.95 \quad -116.04 \quad -76.93]^T$	0.42	$[\ 0 \quad 12.70]^T$	$[\ 0.2 \quad 12.7]^T$	0.20	0.12%
$\boldsymbol{\theta} = [-92.92 \quad 14.13 \quad -114.32 \quad -76.56]^T$	0.42	$[\ 0 \quad 2.54]^T$	$[-0.3 \quad 2.4]^T$	0.33	5.02%

1.10 Model-Free Trajectory Tracking in Task Space

With the practicality of the sensor device demonstrated, the next step towards a fully functional robotic unit is the design of a position control scheme. This control scheme must naturally take advantage of the non-collocated feedback of the actual end effector pose provided by the measuring arm.

Consider the general dynamic model of a flexible robotic manipulator:

$$\mathbf{M}(\mathbf{q}_r, \mathbf{q}_f) \begin{bmatrix} \ddot{\mathbf{q}}_r \\ \ddot{\mathbf{q}}_f \end{bmatrix} + \mathbf{h}(\mathbf{q}_r, \mathbf{q}_f, \dot{\mathbf{q}}_r, \dot{\mathbf{q}}_f) + \mathbf{g}(\mathbf{q}_r, \mathbf{q}_f) + \mathbf{K}(\mathbf{q}_r, \mathbf{q}_f) \begin{bmatrix} \mathbf{q}_r \\ \mathbf{q}_f \end{bmatrix} = \begin{bmatrix} \boldsymbol{\tau}_m \\ \mathbf{0} \end{bmatrix} \tag{1.19}$$

where $\mathbf{q}_r$ is the vector of joint variables ('rigid' coordinates), $\mathbf{q}_f$ is the vector of deformation variables, $\mathbf{M}$ is the generalised inertia matrix, $\mathbf{h}$ is the vector of Coriolis and centrifugal terms, $\mathbf{g}$ is the vector of gravitational terms, $\mathbf{K}$ is the stiffness matrix of the system, and $\boldsymbol{\tau}_m$ is the vector of actuator torques applied at the joints.

The objective is to find a time-varying torque input $\boldsymbol{\tau}_m$ such that the actual pose of the manipulator, noted $\mathbf{x}_f$, converges to the desired task space pose $\mathbf{x}_d$. However, while the values of $\mathbf{q}_r$ and $\dot{\mathbf{q}}_r$ are given by the motor encoders, the values of $\mathbf{q}_f$ are unknown. Thus, the actual end effector pose of the flexible manipulator, given by

$$\mathbf{x}_f = \mathbf{f}(\mathbf{q}_r, \mathbf{q}_f) \tag{1.20}$$

cannot be computed. Instead, the pose of the flexible manipulator is measured, such that

$$\mathbf{x}_f = \mathbf{x} \tag{1.21}$$

where $\mathbf{x}$ is given by the measuring arm according to (1.7).

The proposed trajectory tracking control is a simple modification of a typical collocated proportional-derivative (PD) controller where the desired task space poses and their time derivatives are mapped to joint coordinates. Thus, the controller equation is given by

$$\boldsymbol{\tau}_m = \mathbf{G}_P \mathbf{J}_r^{-1}(\mathbf{q}_r)[\mathbf{x}_d - \mathbf{x}_f] + \mathbf{G}_D[\mathbf{J}_r^{-1}(\mathbf{q}_r)\dot{\mathbf{x}}_d - \dot{\mathbf{q}}_r] + \mathbf{g}_r(\mathbf{q}_r) \tag{1.22}$$

where $\mathbf{G}_P$ and $\mathbf{G}_D$ are, respectively, the proportional and derivative gain matrices and $\mathbf{J}_r(\mathbf{q}_r)$ and $\mathbf{g}_r(\mathbf{q}_r)$ are, respectively, the Jacobian matrix and the vector of gravity compensation torques, both associated with the rigid body model of the flexible manipulator. As such, the controller does not rely on prior knowledge of the dynamic model of the manipulator, nor its stiffness matrix.

Alternatively, if velocity control is used instead of torque or current control, a close equivalent to (1.22) can be achieved with

$$\dot{\mathbf{q}}_{r,c} = \mathbf{J}_r^{-1}(\mathbf{q}_r)[\dot{\mathbf{x}}_d + \boldsymbol{\lambda}(\mathbf{x}_d - \mathbf{x}_f)] \tag{1.23}$$

where $\dot{\mathbf{q}}_{r,c}$ is the actuator velocity command sent to the controller and $\boldsymbol{\lambda}$ is a tuning parameter matrix.

As expected with this type of Cartesian controller, extra caution is required in the vicinity of the singular configurations of the manipulator, due to the bad conditioning of the Jacobian matrix. Nevertheless, there exist many methods that circumvent this issue, with a notable example being the damped least squares method (Buss and Kim, 2005).

1.11 Simulation

As a first step towards demonstrating the effectiveness of the proposed solution, a dynamic simulation was carried out in MATLAB. The simulated robot is a 2-DoF planar serial manipulator with flexible rotary joints subject to gravity. The parameters of the simulated manipulator are shown in Table 1.2.

Table 1.2 – Simulated Manipulator Parameters

Parameter	**Value**
Link 1 Length [m]	0.45
Link 2 Length [m]	0.45
Link 1 Mass [kg]	1.44
Link 2 Mass [kg]	0.50
Payload Mass [kg]	2
Joint 1 Reduction ratio	121:1
Joint 2 Reduction ratio	90:1
Joint 1 Moment of inertia* [kgm^2]	2.5×10^{-3}
Joint 2 Moment of inertia* [kgm^2]	1.0×10^{-3}
Joint 1 Stiffness [Nm/rad]	2000
Joint 2 Stiffness [Nm/rad]	1000

* At reducer input.

This simulation is a three step process. First, a trajectory planner generates the next desired pose according to the specified trajectory. Second, the time-varying torque inputs are computed according to the controller equation and using the manipulator's current kinematic states. Third, the dynamic model in (1.19) is numerically solved, yielding the next kinematic states.

The task consists in moving up 0.5 meters in the Y direction (against gravity) following a fifth order interpolation, while keeping the X coordinate fixed. The trajectory is executed in 2 seconds. The graphs in Figure 1.6 show the desired reference trajectory and the resulting tracking error of three different controllers applied to this task. The relevant error values for quantitative analysis are presented in Table 1.3.

The first case illustrates the results of a traditional PD controller which ignores the robot's

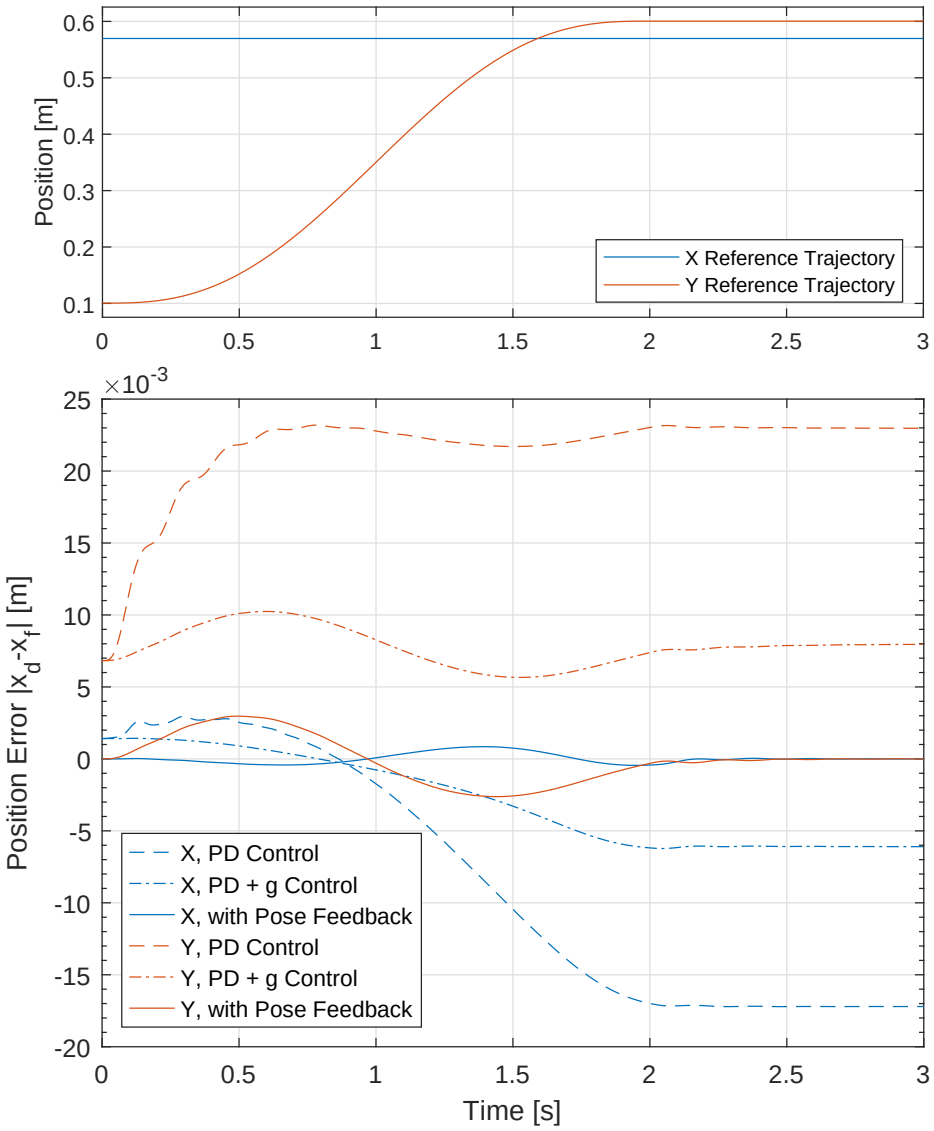

Figure 1.6 – Desired reference trajectories in task space and tracking error of three different controllers applied to the simulated flexible manipulator. Payload is 2 kg and gravity is in the negative Y direction.

Table 1.3 – Simulation Tracking Error Results

	Error Norm [mm]				
Controller	Initial	Final	Min	Max	RMS
PD	7.0	28.7	7.0	28.8	24.8
PD + g	7.0	10.0	6.4	10.3	8.9
Pose Feedback	0	0	0	3.0	1.6

flexibility. In other words, this controller relies on the rigid model, forward kinematics and actuator positions of the manipulator to track its end effector pose. As expected, there is a non-negligible initial error in the direction of gravity, due to flexibility, which worsens as the manipulator reaches a more extended configuration. Because of the coupled nature of the serial manipulator, a notable error in the X direction is also observed. Practically, the actual manipulator stands lower than predicted by the rigid model, deformed under the weight of its own links and its payload. This static error, expected with PD control, is worsened by the flexibility of the manipulator. Thus, the trajectory is not accurately tracked and its end point is never reached.

The second case shows the effect of including a feedforward gravity compensation term, based on the rigid static model, in the PD control scheme ('PD + g' control). As expected, although every error metric is improved compared to the PD controller, a large static error of 10 mm remains in the final configuration. Gravity compensation cannot adequately eliminate the static error of the PD controller without the stiffness model of the manipulator. Indeed, in this case, once the forward kinematics –based on the actuator positions– have converged to the desired pose, the controller lacks the necessary information to further adjust the actual pose of the manipulator. In this sense, including an integrator term in this controller would also be useless.

The third case illustrates the behaviour of the proposed controller with actual pose feedback, as defined in (1.22). This additional feedback is considered available at each time step of the simulation, since the real sensor system allows sampling rates higher than 1 kHz. The results clearly show that the actual pose of the flexible manipulator converges to the desired value, both statically and dynamically. The static error tends to zero in the final configuration. In this example, the maximal error magnitude, which occurs during the most dynamic phases of the trajectory, is 3 mm. This is lower than the overall minimum error achieved with the other controllers. Thus, the end effector effectively tracks the prescribed Cartesian trajectory.

The simulation results indicate that, in theory, the deformation of a flexible manipulator can be compensated by feeding back the measurement of the end effector pose. Moreover, with this type of feedback, the controller does not require a detailed dynamic model of the robot. Of course, this simulation represents an idealized model of a flexible joint manipulator

and ignores practical considerations such as noise, delays, friction, or bending of the links. Therefore, the next sections are aimed at introducing and detailing an experimental setup to fully validate the proposed solution in real-world conditions.

1.12 Proof of Concept

As discussed in the Introduction, the proposed sensor system can shift the design paradigm of robotic manipulators for certain applications such as pHRI. Indeed, with proprioception decoupled from actuation, the design can be based on strength, rather than stiffness. To substantiate this claim, a serial manipulator prototype (shown in Figure 1.7) was built. With three rotary joints, this manipulator was designed for 3D positioning tasks, with a maximum payload of 5 kg and a reach of 0.9 m. The prototype was deliberately made flexible, for practical and demonstration purposes.

Practically, positioning the distal actuator at the base of the robot rather than at the joint requires a means of power transmission. Again, moving the actuators to the base has the advantage of drastically reducing the moving mass and inertia of the robot. However, due to the manipulator links being flexible, 'rigid' power transmission methods such as drive shafts or gear trains are inadequate. Indeed, the method must accommodate some degree of deflection in the links. With such constraints, synchronous pulleys and belts are a natural lightweight and low-backlash solution. These belts are inherently flexible and this property is generally only negligible for short belt lengths or very stiff materials. In consequence, the rotational stiffness of the affected joint is effectively reduced.

For demonstration purposes, the second and third manipulator links were designed as slender as possible. With this methodology, the links can still withstand the static and dynamic efforts induced by the payload, but are more flexible than links whose mass would be distributed away from the centroid of their cross-section. Moreover, a flexible coupling was chosen to transmit power to the second joint, rather than rigidly attaching the second link to the actuator. Finally, per the reasoning detailed in Section 1.4, the first mobile link and the first joint were designed to be rigid.

The rotational stiffness of the second joint is mainly determined by the flexible coupling between the actuator and the link. The selected coupling is specified at a static torsional stiffness of 2600 Nm/rad. The stiffness of the third joint is governed by the type of belt, its section properties, and its total length. Computing and transforming the linear stiffness of the belt to a static torsional stiffness yields a value in the order of 1300 Nm/rad at the distal joint (joint 3). For comparison, values around 10^5 Nm/rad represent a minimum level of elasticity that can be neglected in practice (Zollo et al., 2005). Finally, the second and third links were designed to each allow a deflection of up to two centimetres in the direction of gravity when in the least favourable (horizontal, fully extended) configuration.

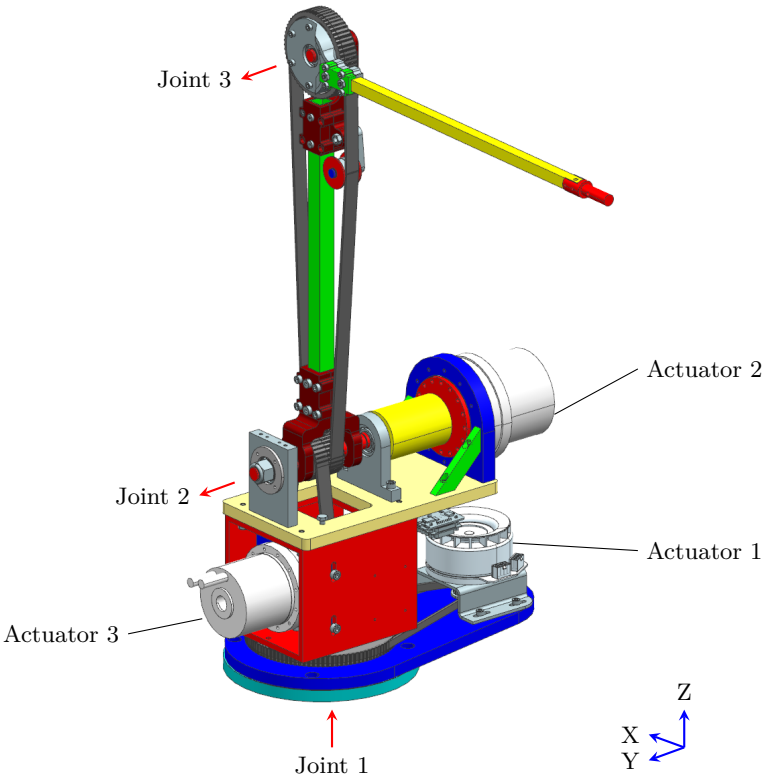

Figure 1.7 – CAD model of the 3-DoF lightweight serial manipulator prototype. Joint axes are indicated with red arrows.

Table 1.4 – Mass Properties of the Prototype Versus a UR5 Robot

Property	**Link**	**Prototype**	**UR5 Robot**
Mass [kg]	l_1	9.90	3.70
	l_2	1.44	8.39
	l_3	0.50	2.33
Moment of inertia* [kgm^2]	l_1	0.182	0.008
	l_2	0.077	0.597
	l_3	0.014	0.101

* Moment of inertia of link l_i is given about joint j_i.

This manipulator is *not* equipped with link side encoders. Thus, with flexible links and flexible joints, the manipulator alone cannot accurately estimate its actual pose. The encoders are integrated into the actuators for joint control purposes. The first actuator is a Maxon EC-90 direct drive motor coupled to a 4.54:1 synchronous belt reducer. The second actuator is a Harmonic Drive SHA-25 with a 121:1 integrated gearbox. The third actuator is a Harmonic Drive SHA-20 with a 81:1 built-in reducer coupled to a synchronous belt transmission, yielding an effective ratio of 90:1 at the third joint.

The resulting mass properties of the prototype, given by the CAD model, are shown in Table 1.4, along with values from the Universal Robots UR5 manipulator for comparison. The UR5 cobot is ubiquitous in industry and in the literature and was thus chosen for comparison. Its parameters are also typical of manipulators in the 5 kg payload range. As expected, for a similar payload and reach, the proposed design allows the moving mass (links 2 and 3) to be drastically reduced. When combined with the lower moment of inertia of the links, a much lower reflected inertia at the end-effector can be expected. For instance, the total moment of inertia of the robot about joint 1 in a completely extended horizontal configuration is 0.446 kgm^2 for the proposed prototype and 1.846 kgm^2 for the UR5. Moreover, while the mass of the first link is naturally greater, the total mass is notably reduced. Of course, when comparing values, it should be considered that a UR5 is designed to carry the weight of 3 other links and actuators further down the kinematic chain. This however only further supports the idea that these actuators should ideally be moved as close to the base as possible.

Along with the manipulator prototype, an associated measuring arm was also designed and built, according to the methods in Section 1.7 and Section 1.8. The actual device and a schematic representation of its kinematic model are shown in Figure 1.8. The complete robotic unit is also shown in a working configuration in Figure 1.9. As it can be observed, this measuring arm is different from the planar model that was introduced in Section 1.9 for testing purposes. For simplicity, the number of joints was limited to five. Along the kinematic chain, each joint axis is perpendicular to the previous joint, yielding a potential of five Cartesian DoFs. However, the end point of the measuring chain is connected to the end effector of the manipulator by a spherical joint, restricting the number of Cartesian DoFs to three. Thus, this specific model of the proposed sensor system is designed to only measure the 3D position (not the orientation) of the end effector. As a result, as explained in Section 1.4, this measuring arm has two redundant joints which allow link movements without affecting the measured value. Due to this relatively low degree of redundancy, elastic elements are used to maintain the measuring arm in a favourable configuration close to the manipulator.

In order to provide a better picture of the overall flexibility of the robot, Table 1.5 shows the measured deflection at the end-effector in three typical configurations with a 2 kg payload. To collect the data, the manipulator is first put into the desired configuration with the actuator brakes applied and without a payload. This initial unloaded position is recorded by the measuring arm. The payload is then added and the new static equilibrium position is recorded by the measuring arm. With the brakes applied, the motor side of the joints cannot move and the deflection can only be a result of the flexibility of the joints and links. It is worth noting that this method only measures the deflection caused by the payload. Indeed, before adding the payload, the manipulator is already slightly deformed under its own weight. The first configuration has the second and third link respectively vertical and horizontal. The second configuration has both links at an angle in a typical working configuration, where the

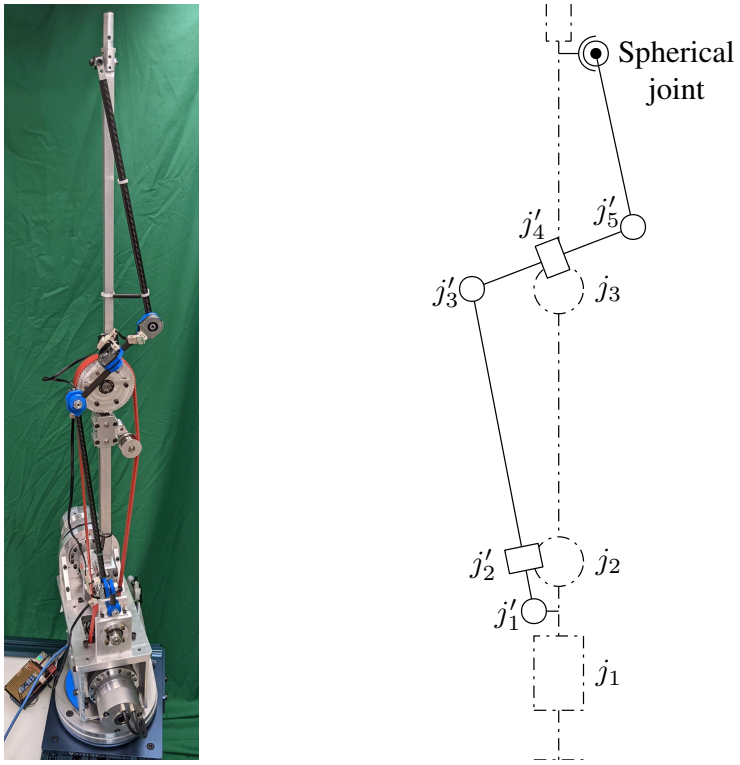

Figure 1.8 – (Left) Parallel measuring arm mounted on serial manipulator prototype. (Right) Schematic representation of the manipulator (dashed lines) and measuring arm (solid lines).

Table 1.5 – Static Deflection of the Manipulator at the End Effector When Adding a 2 kg Payload with Brakes Applied

Joint Configuration [deg]	**Deviation [mm]**
$\mathbf{q} = [0 \quad 0 \quad 90]^T$	10.0
$\mathbf{q} = [0 \quad 40 \quad 80]^T$	14.5
$\mathbf{q} = [0 \quad 80 \quad 5]^T$	15.0

work surface would be at base height. The third configuration has the manipulator almost completely extended horizontally.

1.13 Experimental Validation

The final step in validating the proposed sensor system consists in testing it on an actual robotic task. To this end, two trajectory tracking tasks are carried out in real-world conditions with the physical integrated robotic unit described in Section 1.12. Both trajectories require active error compensation in every coordinate. The actual Cartesian position of the manipulator is tracked by the measuring arm.

The relevant experimental results for both trajectories are summarised in Table 1.6. The

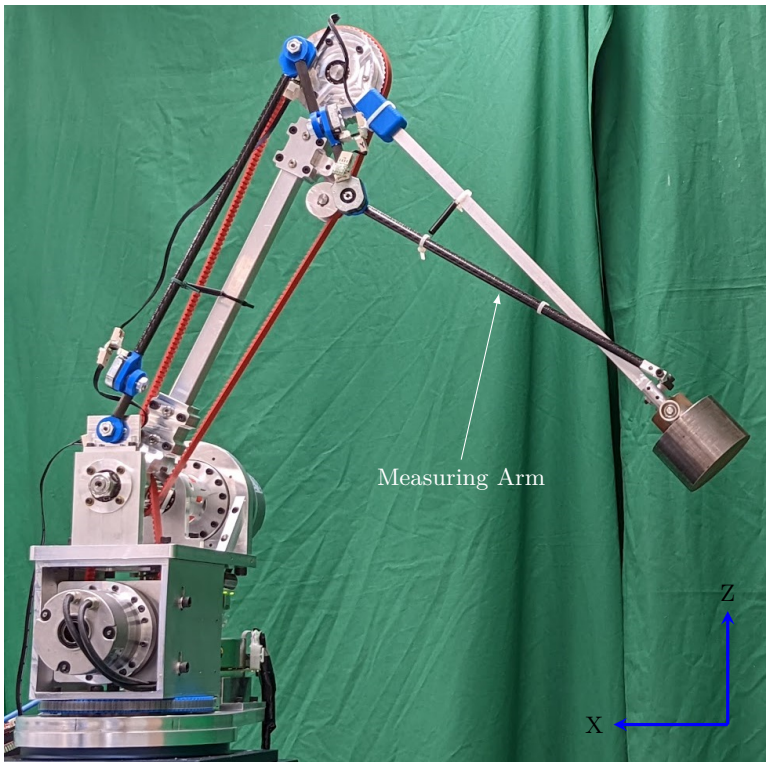

Figure 1.9 – Robotic unit prototype in working configuration with 2 kg payload.

Table 1.6 – Experimental Tracking Error Results

		Error Norm [mm]					**$\pm 1\sigma$ Uncertainty [mm]**		
Trajectory	**Controller**	Initial	Final	Min	Max	RMS	Initial	Final	Average
Vertical	Pose Feedback	0.3	0.5	0.2	8.4	4.3	±0.13	±0.16	±0.15
	PD + g	9.2	17.4	9.0	20.0	16.8			
Horizontal	Pose Feedback	0.3	0.5	0	2.9	1.2	±0.14	±0.14	±0.14
	PD + g	11.5	11.2	9.1	11.6	10.8			

reported uncertainty in the table is computed by converting the resolution of the encoders to standard uncertainty and using the method shown in Section 1.6.

Figure 1.10 shows the test results for the same trajectory as in Section 1.11. Practically, the manipulator must move a 2 kg payload 500 mm up in the Z direction (against gravity) in 2 seconds. It is interesting to note that with traditional PD control, unintuitive out-of-plane deflections (in the Y direction) can not only be observed in the initial configuration, but become larger in the less favourable (more extended) final configuration. This phenomenon was not observable in the 2D simulation. Still, as expected, the main components of the position error are caused by the very large in-plane (XZ) deflections, which reach their maximum value around the point of maximum velocity. The results with the proposed sensor

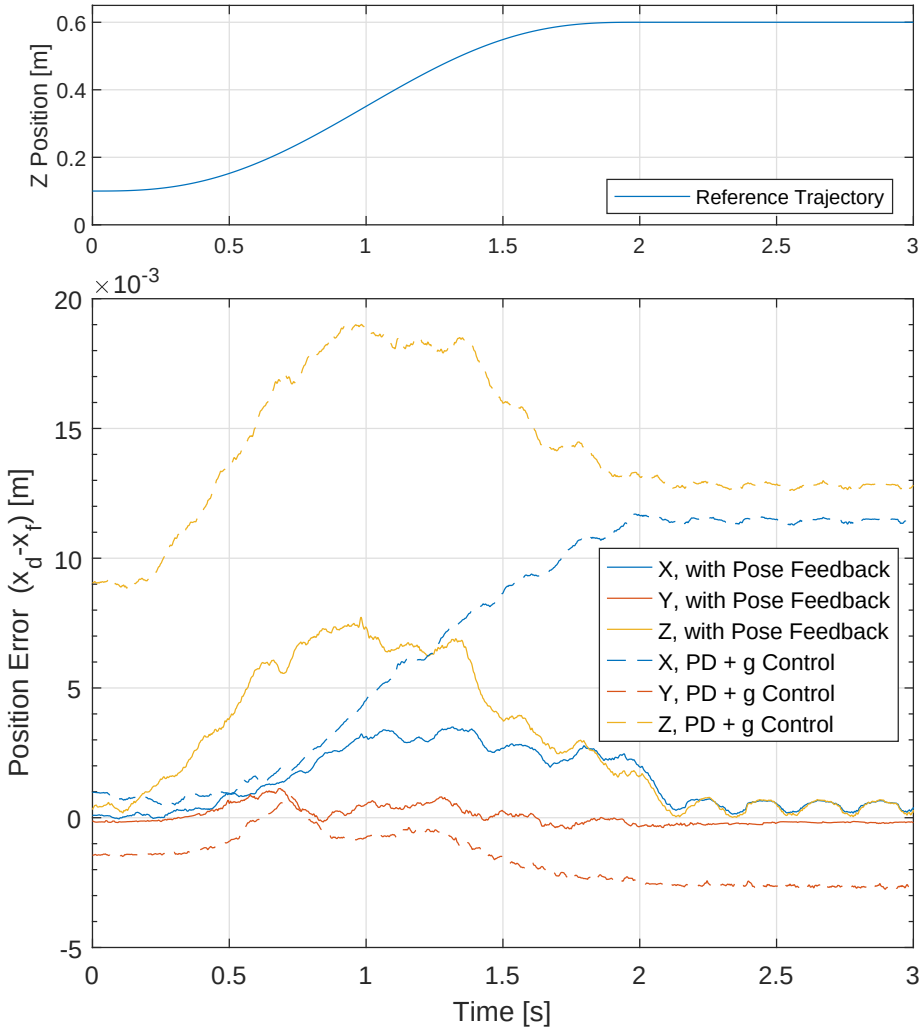

Figure 1.10 – (Top) Prescribed vertical trajectory in task space, where $x_d = -0.5$ m and $y_d = 0.03$ m are constant. (Bottom) Position error during the trajectory tracking task, with the proposed control and with a PD control with gravity compensation (PD + g). Payload is 2 kg and gravity is in the negative Z direction.

system show a drastic reduction in both static and dynamic errors. Indeed, even in the unfavourable final configuration, the out-of-plane static error is virtually eliminated with respect to the precision of the prototype sensor, and the in-plane static errors are reduced to under 0.4 mm, for a total error norm of 0.5 mm. The maximum dynamic error in this example trajectory is reduced by 58% compared to the traditional PD approach. The remaining dynamic error could be further reduced by including inertia feedforward terms (computed torque method) in the controller or, naturally, by considering trajectories with lower dynamics.

Figure 1.11 shows the time graphs of the second trajectory. This trajectory requires coordinated motion of the three actuators and illustrates the behaviour of the robot when moving perpendicularly to gravity. Practically, the manipulator must move a 2 kg payload 400 mm

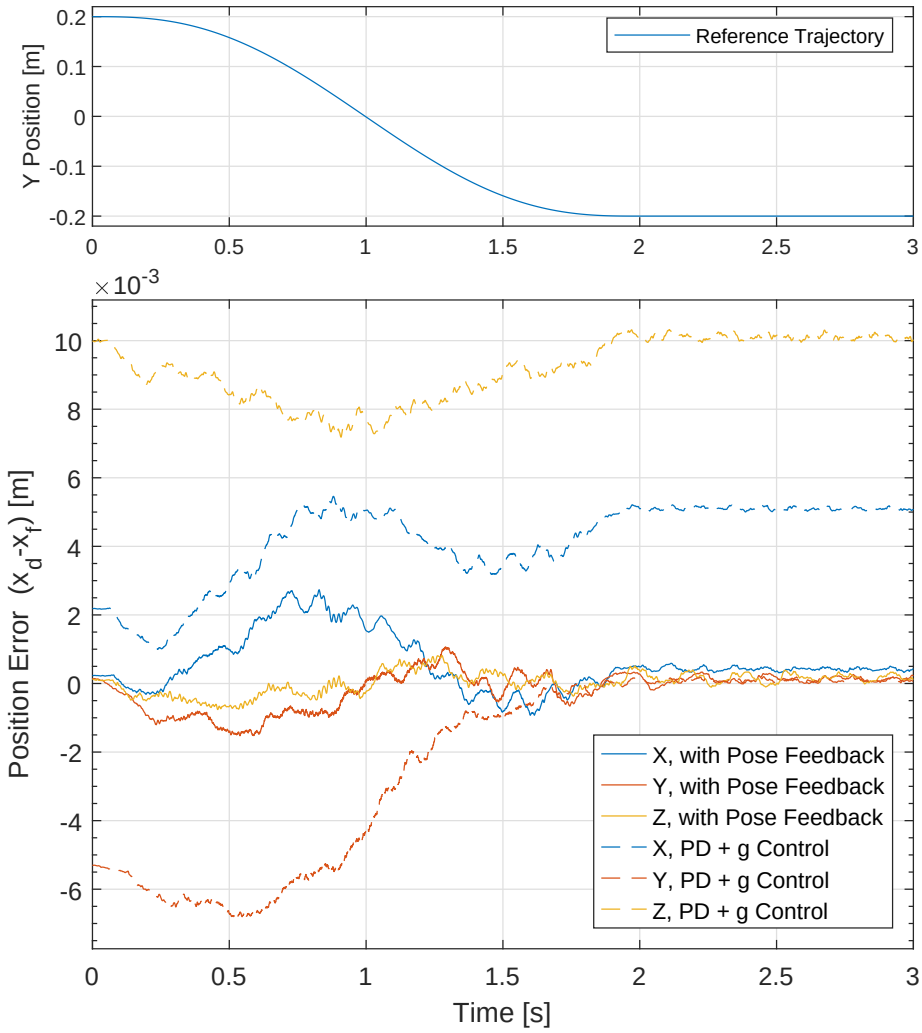

Figure 1.11 – (Top) Prescribed horizontal trajectory in task space, where $x_d = -0.3$ m and $z_d = 0.4$ m are constant. (Bottom) Position error during the trajectory tracking task, with the proposed control and with a PD control with gravity compensation (PD + g). Payload is 2 kg and gravity is in the negative Z direction.

sideways in the Y direction (side to side and not front to back) in 2 seconds. All three coordinates show very low error when using pose feedback compared to the traditional PD controller. While the final configuration differs from the first experiment, the static error is again reduced to 0.5 mm, a notable improvement over the 11.2 mm error with PD control.

To conclude, these results indicate that:

1. The proposed sensor system and controller effectively compensate the static deflection of a flexible manipulator. These results align with what is reported in Merckaert et al. (2018), where a similar vertical static error component of 0.3 mm was achieved (with a simpler 2-DoF flexible manipulator with a 45% smaller reach) and shown to be better than a commercial KUKA robot arm.
2. While doing so, we have also effectively expanded the concept to non-trivial multi-DoF error measurement and compensation, along with dynamic trajectory tracking.

1.14 Conclusion

In this paper, a non-collocated sensor system consisting of a serial chain of lightweight links and instrumented passive joints was developed. This device is mounted in parallel to a flexible robotic manipulator to form an integrated robotic unit that can measure its own deflection at the end effector. The kinematic constraints associated with the device were detailed and shown to be considerable design obstacles. To avoid these obstacles, a basic kinematic structure was proposed where the measuring arm spans all but the first link and joint of the manipulator. It was also proposed to take advantage of kinematic redundancy in the measuring arm to prevent any interference with the manipulator, while also ensuring the safety of human operators. To assess the precision of this sensor system, an error model was developed based on a kinematic sensitivity index. This method gives an upper bound on the Cartesian resolution of the device in a given configuration. A simple mechanical and electronic design, which allows the device to be easily assembled and calibrated, was presented. The practicality of the measuring arm was first demonstrated by comparing actual measurements from a simplified planar prototype against ground truth values. Then, with feedback on the actual end effector pose readily available, a position control scheme was devised. The controller allows a flexible manipulator to track trajectories in task space without a dynamic model or a stiffness model, as shown by simulation results. Finally, a complete integrated robotic unit was built as an experimental setup. The unit comprises a lightweight 3-DoF manipulator and a 5-DoF redundant measuring arm. The experimental results indicate that the robot can effectively compensate position errors and accurately track trajectories even with flexible links and joints.

Such a sensor system introduces new possibilities for applications related to pHRI. Concretely, the detection of user-induced deviations at the end effector will be investigated in future works.

This could lead to new control possibilities based on intuitive physical interactions between the human operator and the robot.

1.15 Bibliographie

T. Berger and L. Lanza. Output tracking for a non-minimum phase robotic manipulator. *IFAC-PapersOnLine*, 54(9) :178–185, 2021. ISSN 24058963. doi : 10.1016/j.ifacol.2021.06.074.

S. R. Buss and J.-S. Kim. Selectively Damped Least Squares for Inverse Kinematics. *Journal of Graphics Tools*, 10(3) :37–49, jan 2005. ISSN 1086-7651. doi : 10.1080/2151237X.2005.10129202.

R. H. Cannon and E. Schmitz. Initial Experiments on the End-Point Control of a Flexible One-Link Robot. *The International Journal of Robotics Research*, 3(3) :62–75, sep 1984. ISSN 0278-3649. doi : 10.1177/027836498400300303.

P. Cardou, S. Bouchard, and C. Gosselin. Kinematic-sensitivity indices for dimensionally nonhomogeneous jacobian matrices. *IEEE Transactions on Robotics*, 26(1) :166–173, feb 2010. doi : 10.1109/TRO.2009.2037252.

A. Chen, R. Yin, L. Cao, C. Yuan, H. Ding, and W. Zhang. Soft robotics : Definition and research issues. In *2017 24th International Conference on Mechatronics and Machine Vision in Practice (M2VIP)*, pages 366–370. IEEE, nov 2017. ISBN 978-1-5090-6546-2. doi : 10.1109/M2VIP.2017.8267170.

A. De Santis, B. Siciliano, A. De Luca, and A. Bicchi. An atlas of physical human–robot interaction. *Mechanism and Machine Theory*, 43(3) :253–270, mar 2008. ISSN 0094114X. doi : 10.1016/j.mechmachtheory.2007.03.003.

D. Feliu-Talegon and V. Feliu-Batlle. Control of Very Lightweight 2-DOF Single-Link Flexible Robots Robust to Strain Gauge Sensor Disturbances : A Fractional-Order Approach. *IEEE Transactions on Control Systems Technology*, 2021. doi : 10.1109/TCST.2021.3053857.

J. P. W. Flemming. Monitoring the location of a robot hand. U.S. Patent 4119212A, jul 1977.

P. L. García, S. Crispel, E. Saerens, T. Verstraten, and D. Lefeber. Compact Gearboxes for Modern Robotics : A Review. *Frontiers in Robotics and AI*, 7 :103, aug 2020. ISSN 2296-9144. doi : 10.3389/frobt.2020.00103.

D. V. Gealy, S. McKinley, B. Yi, P. Wu, P. R. Downey, G. Balke, A. Zhao, M. Guo, R. Thomasson, A. Sinclair, P. Cuellar, Z. McCarthy, and P. Abbeel. Quasi-direct drive for low-cost compliant robotic manipulation. *Proceedings - IEEE International Conference on Robotics and Automation*, 2019-May :437–443, may 2019. doi : 10.1109/ICRA.2019.8794236.

S. Gong. A novel ultra-precision integrated robotic system. *Robotica*, 23(4) :501–513, jul 2005. ISSN 0263-5747. doi : 10.1017/S0263574704001171.

A. Grädener and L. Rokeach. Arrangement for an articulated arm robot and method for determining the positioning of a mount for an end effector of an articulated arm robot. International Patent WO2019011381A1, jan 2019.

S. Haddadin and E. Croft. Physical Human–Robot Interaction. In O. Siciliano Bruno and Khatib, editor, *Springer Handbook of Robotics*, pages 1835–1874. Springer International Publishing, Cham, 2016. ISBN 978-3-319-32552-1. doi : 10.1007/978-3-319-32552-1_69.

S. Haddadin, A. Albu-Schaffer, and G. Hirzinger. The role of the robot mass and velocity in physical human-robot interaction - Part I : Non-constrained blunt impacts. In *2008 IEEE International Conference on Robotics and Automation*, pages 1331–1338. IEEE, may 2008. ISBN 978-1-4244-1646-2. doi : 10.1109/ROBOT.2008.4543388.

M. Hussein. A review on vision-based control of flexible manipulators. *Advanced Robotics*, 29 (24) :1575–1585, dec 2015. doi : 10.1080/01691864.2015.1078743.

C. T. Kiang, A. Spowage, and C. K. Yoong. Review of Control and Sensor System of Flexible Manipulator. *Journal of Intelligent & Robotic Systems*, 77(1) :187–213, jan 2015. ISSN 0921-0296. doi : 10.1007/s10846-014-0071-4.

K. Merckaert, A. De Beir, N. Adriaens, I. El Makrini, R. Van Ham, and B. Vanderborght. Independent load carrying and measurement manipulator robot arm for improved payload to mass ratio. *Robotics and Computer-Integrated Manufacturing*, 53 :135–140, oct 2018. ISSN 0736-5845. doi : 10.1016/J.RCIM.2018.04.001.

J. Oliveira, A. Ferreira, and J. C. Reis. Design and experiments on an inflatable link robot with a built-in vision sensor. *Mechatronics*, 65 :102305, feb 2020. ISSN 09574158. doi : 10.1016/j.mechatronics.2019.102305.

U. K. Sahu, D. Patra, and B. Subudhi. Vision-based tip position tracking control of two-link flexible manipulator. *IET Cyber-Systems and Robotics*, 2(2) :53–66, jun 2020. ISSN 2631-6315. doi : 10.1049/iet-csr.2019.0035.

M. Sayahkarajy, Z. Mohamed, and A. A. Mohd Faudzi. Review of modelling and control of flexible-link manipulators. *Proceedings of the Institution of Mechanical Engineers, Part I : Journal of Systems and Control Engineering*, 230(8) :861–873, sep 2016. ISSN 0959-6518. doi : 10.1177/0959651816642099.

A. H. Slocum. Mechanism to determine position and orientation in space. U.S. Patent 4606696A, jun 1984.

P. Staufer and H. Gattringer. State estimation on flexible robots using accelerometers and angular rate sensors. *Mechatronics*, 22(8) :1043–1049, dec 2012. ISSN 0957-4158. doi : 10.1016/J.MECHATRONICS.2012.08.009.

T. Steinecker, A. Kurdas, N. Mansfeld, M. Hamad, R. J. Kirschner, S. Abdolshah, and S. Haddadin. Mean Reflected Mass : A Physically Interpretable Metric for Safety Assessment and Posture Optimization in Human-Robot Interaction. In *2022 International Conference on Robotics and Automation (ICRA)*, pages 11209–11215. IEEE, may 2022. ISBN 978-1-7281-9681-7. doi : 10.1109/ICRA46639.2022.9811582.

D. Subedi, T. N. Aune, I. Tyapin, and G. Hovland. Static Deflection Compensation of Multi-Link Flexible Manipulators Under Gravity. *IEEE Access*, 10 :9658–9667, 2022. ISSN 21693536. doi : 10.1109/ACCESS.2022.3144404.

S. Toxiri, A. Calanca, J. Ortiz, P. Fiorini, and D. G. Caldwell. A Parallel-Elastic Actuator for a Torque-Controlled Back-Support Exoskeleton. *IEEE Robotics and Automation Letters*, 3 (1) :492–499, jan 2018. ISSN 2377-3766. doi : 10.1109/LRA.2017.2768120.

K. Wen, T. S. Nguyen, D. Harton, T. Laliberté, and C. Gosselin. A Backdrivable Kinematically Redundant (6+3)-Degree-of-Freedom Hybrid Parallel Robot for Intuitive Sensorless Physical Human–Robot Interaction. *IEEE Transactions on Robotics*, 37(4) :1222–1238, aug 2021. ISSN 1552-3098. doi : 10.1109/TRO.2020.3043723.

L. Zollo, B. Siciliano, A. De Luca, E. Guglielmelli, and P. Dario. Compliance Control for an Anthropomorphic Robot with Elastic Joints : Theory and Experiments. *Journal of Dynamic Systems, Measurement, and Control*, 127(3) :321–328, sep 2005. ISSN 0022-0434. doi : 10.1115/1.1978911.

Chapitre 2

Whole-body Intuitive Physical Human-Robot Interaction with Flexible Robots Using Non-Collocated Proprioceptive Sensing

2.1 Résumé

Cet article présente une méthode permettant l'interaction physique humain-robot de façon intuitive avec les manipulateurs flexibles grâce à un système de mesure de l'organe terminal. Le dispositif est une chaîne passive d'encodeurs et de membrures légères, montée en parallèle avec le manipulateur. En mesurant la déviation de l'organe terminal par rapport à la base, toute la structure du manipulateur devient une interface potentielle d'interaction, peu importe si la flexion provient des membrures ou des articulations. Le schéma de commande proposé est basé sur un simple asservissement des vitesses articulaires et ne requiert que la connaissance de la matrice jacobienne rigide du manipulateur. L'approche est validée en simulation sur un modèle simplifié, ainsi qu'expérimentalement sur un prototype physique de robot sériel à trois degrés de liberté avec articulations et membrures flexibles. Les résultats indiquent une interaction humain-robot intuitive, avec des forces d'interaction inférieures à 25 N pour des tâches dynamiques.

2.2 Abstract

This paper presents a method enabling intuitive physical human-robot interaction (pHRI)

with flexible robots using an end-point sensing device. The device is a passive serial chain of encoders and lightweight links, mounted in parallel with the manipulator. By measuring the deflection of the end-effector relative to the base, the whole body of the manipulator becomes a potential interaction interface, whether the compliance stems from the links or the joints. The proposed control scheme is a simple joint velocity control that only requires knowledge of the rigid body Jacobian matrix of the manipulator. The approach is validated both in simulation on a simplified model and experimentally on a physical 3-DoF flexible-link flexible-joint serial robot. The results indicate that intuitive pHRI is achieved, with interaction forces under 25 N even for tasks with high dynamics.

2.3 Introduction

In the context of physical human-robot interaction (pHRI), direct drive is generally regarded as the ideal actuation method. Indeed, direct drive actuators are intrinsically transparent and drastically reduce the reflected inertia at the end-effector, while not exhibiting the typical nonlinearities of transmission systems such as backlash and friction, which are still a topic of research (García et al., 2020). The backdrivability resulting from these characteristics makes direct drive actuators suitable for intent detection (Losey et al., 2018) in pHRI, and allows sensorless impedance control (Wen et al., 2021).

Still, implementing direct drive actuation in serial robots or in high payload applications remains a challenge. Quasi-direct drive was achieved for a serial robot in Gealy et al. (2019), at the cost of relatively low payload and dynamics.

Therefore, various solutions have been proposed to enable intent detection in pHRI with non-backdrivable actuators. Notable examples include force-torque (FT) sensors (Haddadin and Croft, 2016) at the end-effector for admittance control (Keemink et al., 2018), joint FT sensors for impedance control (Dehio et al., 2022), tactile sensors such as human-like skins (Teyssier et al., 2021), and low impedance shells (Laliberté and Gosselin, 2022). One obvious drawback of FT sensors is that unless they are implemented in every joint, the interaction interface is limited to a single location on the robot, generally at the end-effector.

The macro-mini paradigm has also proven to be effective in the context of pHRI, allowing low-impedance interaction even with large payloads (Abdallah et al., 2022), by measuring the relative displacement at the end-effector. This approach nevertheless faces the same previously discussed limitations, namely that intent detection is only possible through the mini robot located at the tip of the macro robot.

Finally, all of the methods discussed above are *control* solutions and none of them contributes to the intrinsic safety of the manipulator. Conversely, in this regard, flexible robots excel. When stiffness is no longer the prime design criteria, manipulators can be made lightweight,

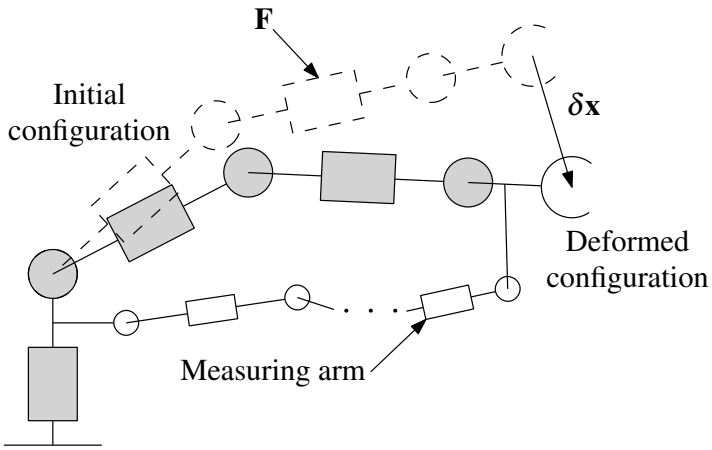

Figure 2.1 – Schematic illustration of the flexible manipulator and measuring arm. A load at any point along the manipulator results in a measurable deformation at the end-effector.

reducing the total energy in the robot for the same velocity (Steinecker et al., 2022). Moreover, compliance partially decouples the very large reflected inertia of the gearmotors from the end-effector dynamics in the event of an impact (Haddadin et al., 2012).

Model-based control of flexible manipulators is notoriously challenging. Therefore, various methods relying on additional feedback have been investigated in the literature (see Kiang et al. (2015) for a review of this topic). The proposed approach in this paper relies on a passive measuring arm mounted in parallel with the manipulator, as illustrated in Figure 2.1. This serial chain of lightweight links and encoders provides fast and reliable end-effector deflection information, accounting for both link and joint compliance.

This type of non-collocated sensing device is only scarcely studied in the literature. In a very conceptual manner, some early patents (Flemming, 1977) have explored the idea of adding passive instrumented links between the ends of one or more robotic manipulator links. This has led to a small series of equally conceptual patents, some more recent (Grädener and Rokeach, 2019).

To the best of the authors' knowledge, in the scientific literature, this concept was first investigated as a way of theoretically increasing the precision of robotic manipulators (Gong, 2005). Then, the first practical implementation of the concept (Merckaert et al., 2018) as a 2-DoF measuring arm demonstrated that separating sensing from actuation had the potential to greatly improve the safety and decrease the mass of robotic arms. In the authors' previous work, the practical roadblocks to the application of the measuring arm concept to higher DoF systems were identified and solved, allowing trajectory tracking with flexible manipulators (Garant and Gosselin, 2023).

The main contribution of this paper is the development and validation of a control method that

enables pHRI with compliant robots by using the measuring system described in Garant and Gosselin (2023). Lightweight and compliant robots are known to be prime candidates for pHRI due to their intrinsic safety at the hardware level, as opposed to conventional extrinsic software or control methods. Therefore, it is proposed to take advantage of the inherent compliance and decoupled reflected inertia of flexible manipulators for intent detection purposes and interaction control in pHRI. This is made possible by the proprioceptive pose information returned by the measuring arm. An analogy can be made with rigid robots prone to backlash, where the use of link-side encoders has been shown to hold the potential for improved overall backdrivability (Yamada and Fujimoto, 2021).

The proposed approach has the following notable advantages over conventional solutions:

— Whole-body interaction is possible, in contrast with the other methods discussed in the introduction.

— Force-torque sensors are not required.

— Compared to typical cobots like the KUKA LBR iiwa manipulator with joint torque sensing, the interaction forces are much lower.

This paper is structured as follows. Section 2.4 introduces the dynamic model of a general flexible robot and explains the working principle of the proposed approach. In Section 2.5, a control scheme enabling pHRI by taking advantage of the pose feedback is detailed. Section 2.6 then shows simulation results using this controller on a virtual flexible manipulator. The results of the experimental validation on a physical flexible-joint flexible-link manipulator are presented in Section 2.7 and discussed in Section 2.8. Finally, conclusions are drawn in Section 2.9.

2.4 Proposed Approach

Consider the general dynamic model of a flexible-link flexible-joint manipulator

$$\mathbf{M}(\mathbf{q}_r, \mathbf{q}_f) \begin{bmatrix} \ddot{\mathbf{q}}_r \\ \ddot{\mathbf{q}}_f \end{bmatrix} + \mathbf{h}(\mathbf{q}_r, \mathbf{q}_f, \dot{\mathbf{q}}_r, \dot{\mathbf{q}}_f) + \mathbf{g}(\mathbf{q}_r, \mathbf{q}_f) + \mathbf{K}(\mathbf{q}_r, \mathbf{q}_f) \begin{bmatrix} \mathbf{q}_r \\ \mathbf{q}_f \end{bmatrix} = \begin{bmatrix} \boldsymbol{\tau}_m \\ \boldsymbol{\tau}_{ext} \end{bmatrix} \tag{2.1}$$

where $\mathbf{q}_r$ is the vector of joint variables ('rigid' coordinates), $\mathbf{q}_f$ is the vector of deformation variables, $\mathbf{M}$ is the generalised inertia matrix, $\mathbf{h}$ is the vector of Coriolis and centrifugal terms, $\mathbf{g}$ is the vector of gravitational terms, $\mathbf{K}$ is the stiffness matrix of the system, $\boldsymbol{\tau}_m$ is the vector of actuator torques applied at the joints, and $\boldsymbol{\tau}_{ext}$ is the mapping of external forces and torques to $\mathbf{q}_f$ coordinates. Under the assumption that the rotational kinetic energy of the actuators is not significantly affected by the movement of the links, a "reduced" model can be derived (Della Santina, 2021). This assumption is valid in the present case where high reduction ratios at the joints are considered. Moreover, this assumption is mathematically true if the actuators are located at the base of the robot (Ott, 2008), irrespective of the reduction ratios. In other words, regardless of how $\mathbf{q}_f$ is defined, $\dot{\mathbf{q}}_f$ has a negligible impact

on the kinetic energy associated with $\dot{\mathbf{q}}_r$, the actuator velocities. The reduced model can then be written (Subudhi and Morris, 2002) as

$$\mathbf{M}_r\ddot{\mathbf{q}}_r + \mathbf{K}_\theta(\mathbf{q}_r - \mathbf{q}_\theta) = \boldsymbol{\tau}_m \tag{2.2}$$

$$\mathbf{M}_f(\mathbf{q}_\theta, \mathbf{q}_f)\begin{bmatrix}\ddot{\mathbf{q}}_\theta \\ \ddot{\mathbf{q}}_f\end{bmatrix} + \mathbf{h}(\mathbf{q}_\theta, \dot{\mathbf{q}}_\theta) + \mathbf{g}(\mathbf{q}_\theta, \mathbf{q}_f) = \begin{bmatrix}-\mathbf{K}_\theta(\mathbf{q}_r - \mathbf{q}_\theta) \\ \mathbf{K}_f(\mathbf{q}_\theta)\mathbf{q}_f\end{bmatrix} + \begin{bmatrix}\boldsymbol{\tau}_{ext} \\ \mathbf{0}\end{bmatrix} \tag{2.3}$$

where $\mathbf{M}_r$ is the constant diagonal matrix of rotor inertias in $\mathbf{q}_r$ (actuator side) coordinates, $\mathbf{K}_\theta$ is the constant diagonal matrix of joint stiffness values, $\mathbf{q}_\theta$ is an intermediate variable representing the link-side joint positions, $\mathbf{M}_f$ is the mass matrix associated with the flexible links, $\mathbf{q}_f$ is the array of link bending mode variables, and $\mathbf{K}_f$ is the stiffness matrix of the flexible links. The only coupling that remains between (2.2) and (2.3) is through the $\mathbf{K}_\theta$ stiffness term.

While the same conclusion can be drawn without it, this reduced model clearly highlights the fact that in the case of a flexible manipulator, the user does not interact with the reflected actuator inertias $\mathbf{M}_r$ directly, but rather via the stiffness of the deformable components represented by $\mathbf{K}$. This decoupling property allows a certain degree of "backdrivability", which can then be amplified with proper control methods.

Indeed, due to the compliant property of the manipulator, the application of a force *at any point* on the robot results in a displacement at the end-effector. If this deflection is measured with respect to the base, then the whole body of the manipulator effectively becomes a potential interface for pHRI, whether the compliance stems from the joints, links or a combination of both.

In a previous paper (Garant and Gosselin, 2023), the practicality of the proposed proprioceptive end-effector position sensor was demonstrated. As shown in Figure 2.1, the device is a passive serial chain of encoders and lightweight links, mounted in parallel with the manipulator. This allows the measurement of the actual tip position *relative to the base*, with classical forward kinematics methods. Kinematic redundancy in the measuring arm ensures that it can always move freely, avoiding singular configurations and negating potential squeezing hazards for human operators. This property also prevents external forces at the end-effector from generating internal efforts in the measuring arm.

2.5 Control Algorithm

As discussed in the introduction, model-based control of flexible manipulators is challenging. Therefore, we propose the following simple, quasi model-free velocity control enabling pHRI with a flexible manipulator:

$$\boldsymbol{\tau}_m = \mathbf{K}_v(\mathbf{J}_r^{-1}\dot{\mathbf{x}}_f - \dot{\mathbf{q}}_r) \tag{2.4}$$

where $\mathbf{K}_v$ is the positive definite diagonal matrix of controller gains, $\mathbf{J}_r := \mathbf{J}(\mathbf{q}_r)$ is the Jacobian matrix of the rigid model of the manipulator and $\dot{\mathbf{x}}_f$ is the actual end-effector velocity derived from the measurement of $\mathbf{x}_f$. Equation (2.4) represents a simple joint velocity controller where the set point is the mapping of the measured velocity at the end-effector to $\mathbf{q}_r$ coordinates. The joint velocities are obtained by differentiating the joint positions. The joint accelerations are therefore ignored due to noise.

The only model required is the rigid Jacobian of the manipulator, which can typically be easily derived. In the vicinity of singular configurations, due to the bad conditioning of the Jacobian matrix, special methods of inversion should be used such as the damped least squares method (Buss and Kim, 2005).

Alternatively, one can think of (2.4) as a task-space controller making a virtual rigid manipulator with identical geometric parameters match the measured tip velocity of the physical flexible manipulator, such that

$$\mathbf{F}_m = \mathbf{J}_r^{-T}\mathbf{K}_v\mathbf{J}_r^{-1}(\dot{\mathbf{x}}_f - \dot{\mathbf{x}}_r) \tag{2.5}$$

where $\mathbf{F}_m$ is the equivalent force applied at the virtual end-effector and $\dot{\mathbf{x}}_r = \mathbf{J}_r\dot{\mathbf{q}}_r$.

It is interesting to note that in this application, the forces applied by the user are always in the same direction as the controller effort, relaxing the need for high controller gains.

2.5.1 Stability

Consider the typical equation of a PD controller:

$$\boldsymbol{\tau}_{PD} = \mathbf{K}_p(\mathbf{q}_{r,d} - \mathbf{q}_r) + \mathbf{K}_v(\dot{\mathbf{q}}_{r,d} - \dot{\mathbf{q}}_r) \tag{2.6}$$

where $\mathbf{K}_p$ and $\mathbf{K}_v$ are the constant diagonal positive definite matrices of proportional and derivative gains, respectively, and $\mathbf{q}_{r,d}$ and $\dot{\mathbf{q}}_{r,d}$ are the desired joint position and velocity arrays. Suppose then that the desired joint position is simply expressed by the first order integration of the desired velocity, such that

$$\dot{\mathbf{q}}_{r,d} = \mathbf{J}_r^{-1}\dot{\mathbf{x}}_f \tag{2.7}$$

$$\mathbf{q}_{r,d} = \mathbf{q}_r + \mathbf{J}_r^{-1}\dot{\mathbf{x}}_f\delta t \tag{2.8}$$

where δt is the controller time step. Substituting (2.7) and (2.8) into (2.6) yields

$$\begin{aligned}\boldsymbol{\tau}_{PD} &= \mathbf{K}_p(\mathbf{J}_r^{-1}\dot{\mathbf{x}}_f\delta t) + \mathbf{K}_v(\mathbf{J}_r^{-1}\dot{\mathbf{x}}_f - \dot{\mathbf{q}}_r) \\ &= \mathbf{K}_v[(\mathbf{K}_v^{-1}\mathbf{K}_p\delta t + \mathbf{I})\mathbf{J}_r^{-1}\dot{\mathbf{x}}_f - \dot{\mathbf{q}}_r]\end{aligned} \tag{2.9}$$

Assuming a very small time step δt and high $\mathbf{K}_v$ values, we find

$$\boldsymbol{\tau}_{PD} \approx \mathbf{K}_v(\mathbf{J}_r^{-1}\dot{\mathbf{x}}_f - \dot{\mathbf{q}}_r) \tag{2.10}$$

which is equal to the proposed control in (2.4). In general, the small step assumption is automatically fulfilled by the fast controller sampling rates required for real-time control of robotic systems. In the present case, the controller runs on a real-time computer at 1 kHz ($\delta t = 0.001$ s) and $\mathbf{K}_v$ values are in the order of 10^2, thus validating the assumptions. The proposed control scheme can then be considered equivalent to a typical PD control. We can therefore conclude that the proposed control is asymptotically stable, as demonstrated in De Luca and Siciliano (1992), as long as the robot is not in a singular configuration.

2.5.2 Actuator Dynamics

Recall the reduced model introduced in (2.2) and (2.3). Let us substitute the control equation (2.4) in the actuator dynamics (2.2). Rearranging, we obtain

$$\mathbf{M}_r\ddot{\mathbf{q}}_r + \mathbf{K}_\theta(\mathbf{q}_r - \mathbf{q}_\theta) + \mathbf{K}_v(\dot{\mathbf{q}}_r - \mathbf{J}_r^{-1}\dot{\mathbf{x}}_f) = \mathbf{0}. \tag{2.11}$$

In practice, the reflected stiffness of the manipulator (or lack thereof) is generally dominated by the effect of joint stiffness. Indeed, since stress is related to strain, there are physical limits to the amount of deflection that the links can undergo with the typical materials used in robotics. Moreover, in the context of pHRI, the links are not expected to vibrate at high frequency, whereas $\dot{\mathbf{q}}_\theta$ is always in the same order of magnitude as $\dot{\mathbf{q}}_r$. Therefore, under these assumptions, let us assume that $\mathbf{J}_r^{-1}\dot{\mathbf{x}}_f$ can be considered a good approximation of $\dot{\mathbf{q}}_\theta$. This assumption is further discussed in the Appendix. This yields the following system of decoupled equations:

$$\mathbf{M}_r\ddot{\mathbf{q}}_r + \mathbf{K}_\theta(\mathbf{q}_r - \mathbf{q}_\theta) + \mathbf{K}_v(\dot{\mathbf{q}}_r - \dot{\mathbf{q}}_\theta) = \mathbf{0} \tag{2.12}$$

where each equation is identical to a typical single mass-spring system subjected to base excitation. The frequency response of such systems in dimensionless form is well known and is reproduced in Figure 2.2 for convenience.

From Figure 2.2, we can conclude that as the damping ratio ζ increases, the amplitude response of the rotors tends to 1 for all frequencies, including the natural frequency. Since ζ is directly proportional to $\mathbf{K}_v$ in this case, the highest possible gain values should be used in order to ensure adequate response in the widest possible range of frequencies. Although the exact stiffness model of the manipulator is not always known, determining bounds on the stiffness values, in order to design $\mathbf{K}_v$, is typically feasible.

Fortunately, the gains can also simply be empirically tuned until the response matches the input. Indeed, if we observe that the actual joint velocities match the desired values derived from $\dot{\mathbf{x}}_f$ in various configurations, we can conclude by definition that the resulting damping ratio is high enough in these configurations to ensure a proper response.

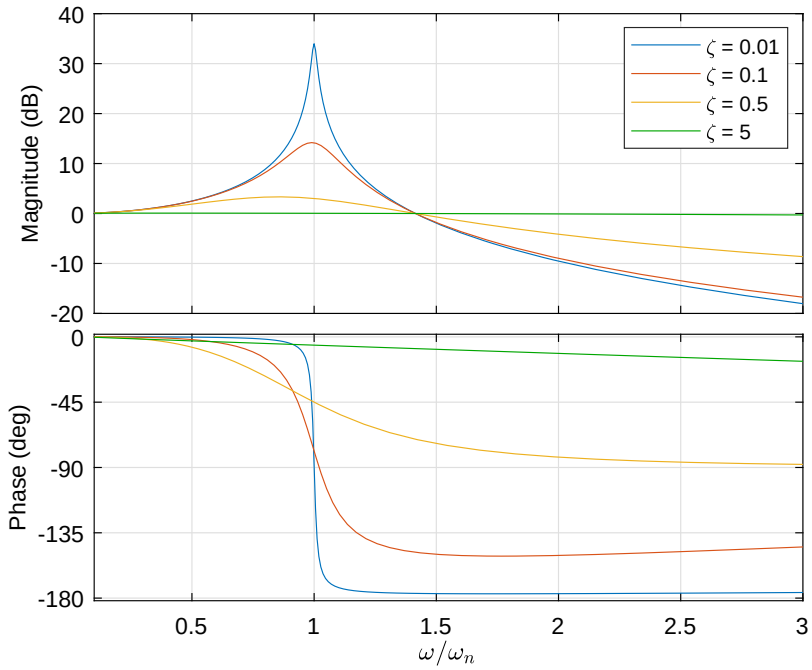

Figure 2.2 – Steady state response amplitude of $\mathbf{q}_r$ modelled by a base ($\mathbf{q}_\theta$) excited mass-spring-damper system. ζ is the damping ratio and ω_n is the natural frequency.

On a physical system, since $\dot{\mathbf{x}}_f$ and $\dot{\mathbf{q}}_r$ are obtained by differentiation, the values of $\mathbf{K}_v$ are limited by various factors such as noise and delays. The next sections show that with realistic manipulator mass, stiffness and size, adequate gain values can still be found.

2.5.3 Gravity Compensation

In the previous subsection, it was shown that under the joint control in (2.4), given sufficiently high $\mathbf{K}_v$ gains, the joint values will follow any arbitrary input $\dot{\mathbf{x}}_f$. As previously discussed, in the standard use case, this velocity will be directly imparted by the user, as intended. However, if the interaction controller is switched on without any external force exerted by the human user, nothing prevents the end-effector from moving under the effect of gravity, even if the manipulator is initially at rest. Therefore, a gravity compensation term $\boldsymbol{\tau}_g$ must be added to the control law given in (2.4) to keep the manipulator immobile in the absence of external forces.

Since the manipulator is subject to link and/or joint deformation, the classical rigid gravity compensation $\boldsymbol{\tau}_g = \mathbf{g}_r(\mathbf{q}_r)$ (where $\mathbf{g}_r$ is given by the static model of the rigid robot) is ineffective unless paired with a stiff position control.

In the present case, satisfactory results can be obtained in practice by using the actual measured effector position, assuming small deformations and neglecting the foreshortening of the bent links. This allows us to define the gravity compensation torques, without knowledge of

the stiffness model of the manipulator, as

$$\boldsymbol{\tau}_g = \mathbf{g}_r(\mathbf{f}_k^{-1}(\mathbf{x}_f)) \tag{2.13}$$

where $\mathbf{f}_k^{-1}(\mathbf{x})$ represents the inverse kinematics of the rigid model of the manipulator. If the manipulator is not redundant and only has flexible joints, (2.13) yields mathematically exact results, since in this case $\mathbf{f}_k^{-1}(\mathbf{x}_f) = \mathbf{q}_\theta$. If the manipulator has flexible links, this is equivalent to approximating the first mode bending of the links as a straight line, or lumping link flexibility at the joints.

A few final remarks should be made regarding gravity compensation: While the method proposed here generally only results in an approximation of the gravity compensation torques, this is also the case for any classical method involving a geometric model of the static forces, which is often an imperfect representation of the physical manipulator. Practically, the non-backdrivable nature of a manipulator, mainly due to static friction, is very forgiving of uncertainties in its static model. It is also worth restating that the proposed gravity compensation is only *necessary* when the user is not interacting with the manipulator. It does however improve the overall feeling of the interaction, and it reduces the control effort. Finally, in applications where the robot is already statically balanced, or when it operates in a plane perpendicular to the direction of gravity (such as SCARA-type manipulators) this compensation is naturally not needed.

2.6 Simulation

In this section, a simulation experiment is devised to validate the proposed control scheme on a simulated two-DoF flexible joint manipulator with rigid links, shown in Figure 2.3. The parameters of the simulated manipulator, which are typical of robots in the 5-7 kg payload range, are given in Table 2.1. Although these parameters justify the use of the reduced model, this simulation uses the complete model, as expressed in (2.1), for generality.

Concretely, the experiment consists in simulating an interaction force acting at the tip of the manipulator. This force is modelled as a stiff spring-damper system following a predefined sinusoidal velocity profile in the vertical direction. This simulates a user trying to impart this velocity profile to the end-effector (Muller et al., 2019). The force required to produce this motion is reported for two different cases.

The first case illustrates the behaviour of the flexible manipulator without payload when the user tries to impart a sinusoidal velocity profile of 0.8 m/s amplitude at 1 Hz. The results in Figure 2.4 show that the maximum applied force is 12 N. In Boucher et al. (2021); Laliberté and Gosselin (2022), a similar experiment was reported for both a serial manipulator equipped with very low-impedance interface mechanisms for pHRI and a KUKA LBR IIWA robot set in impedance control mode. For the same velocity profile, the interaction force amplitude with

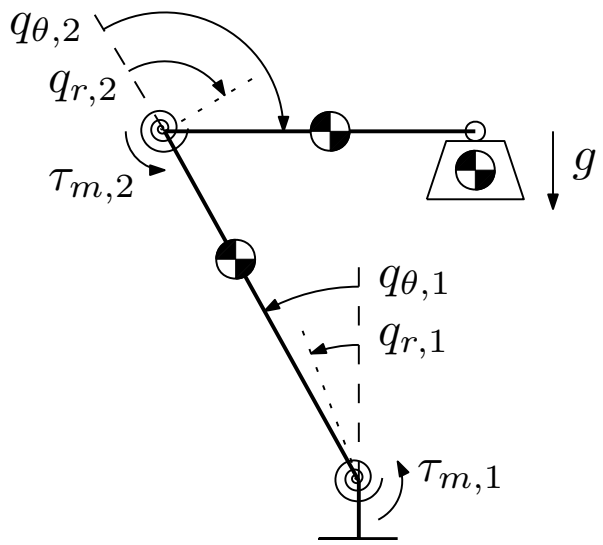

Figure 2.3 – Schematic representation of the simulated 2-DoF flexible-joint manipulator. Gravity is in the vertical direction.

Table 2.1 – Simulated Manipulator Parameters

Parameter	**Value**	**Unit**
Link 1 Length	0.45	m
Link 2 Length	0.45	m
Link 1 Mass	1.44	kg
Link 2 Mass	0.50	kg
Payload Mass	$\{0, 2\}$	kg
Joint 1 Reduction ratio	121:1	-
Joint 2 Reduction ratio	90:1	-
Joint 1 Moment of inertia*	2.5×10^{-3}	kgm^2
Joint 2 Moment of inertia*	1.0×10^{-3}	kgm^2
Joint 1 Stiffness	2000	Nm/rad
Joint 2 Stiffness	1000	Nm/rad

* At reducer input.

the KUKA robot reached a much higher value of over 50 N. The interaction force with the low-impedance interface equipped manipulator in Laliberté and Gosselin (2022), considered very transparent, was reported at 10 N. Our similar results indicate that the proposed solution appears to be appropriate for intuitive pHRI.

The second and more demanding case illustrates the behaviour of the flexible manipulator with a 2 kg payload (closer to real-world use case) when the user tries to impart a sinusoidal velocity profile of the same 0.8 m/s amplitude, but at 2.3 Hz this time. This benchmark frequency is reported in the literature as the average performance limit of the human arm (Aaron and Stein, 1976; Gealy et al., 2019). It is therefore considered here as an upper bound on

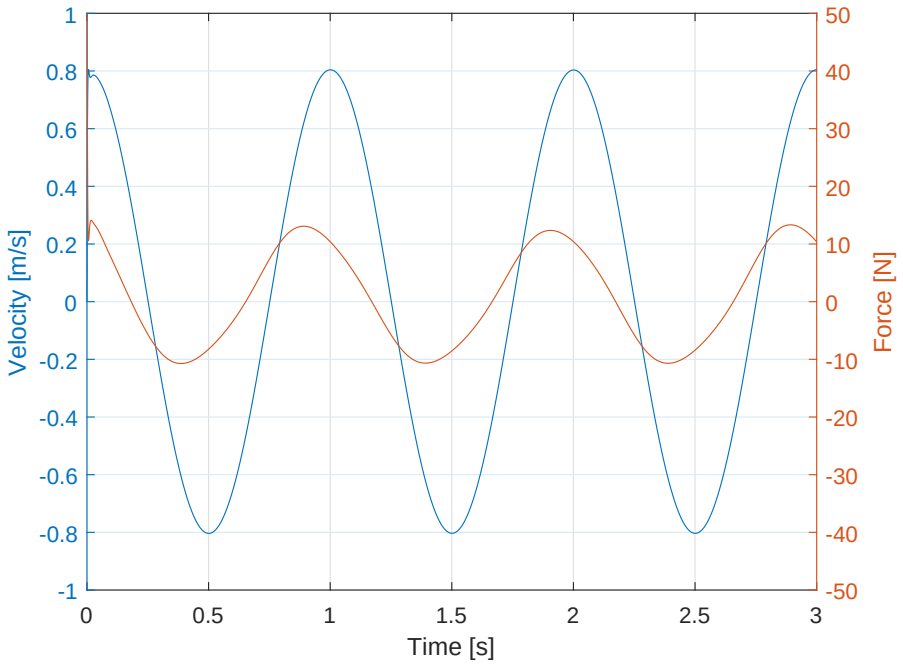

Figure 2.4 – Vertical velocity and user applied force for a sinusoidal velocity profile of 0.8 m/s amplitude at 1 Hz, without payload, for the simulated two-DoF manipulator with flexible joints. Initial configuration is $\mathbf{q}_r = [20, 120]^\circ$.

the physical human-robot interaction bandwidth. The results in Figure 2.5 show a required interaction force amplitude of 34 N for this very dynamic velocity profile. Again, by contrast, the reported results for the KUKA robot, *without payload*, in impedance control mode were above 50 N for a more than 50% slower trajectory.

2.7 Experimental Validation

In this section, an experimental validation of the proposed solution is carried out on a physical prototype. The integrated robotic unit, shown in Figure 2.6, comprises a 3-DoF positioning manipulator with flexible links and joints, and a 5-DoF measuring arm. The measuring arm is connected to the manipulator's end-effector through a spherical joint. This restricts the measurements to position only but ensures that the robotic unit can move (and deflect) freely in all spatial directions, while also ensuring that the measuring arm has two redundant DoFs.

The parameters of the physical robot are identical to the simulated manipulator parameters reported in Table 2.1, except for the joint stiffness values which are approximately 2600 Nm/rad and 1300 Nm/rad for the first and second horizontal joints, respectively. The vertical (proximal) joint is virtually rigid for all practical purposes. The slender links of the manipulator were purposely designed to allow up to approximately 2 cm of deflection at the tip in the worst conditions. More details on the design of the prototype and measuring arm

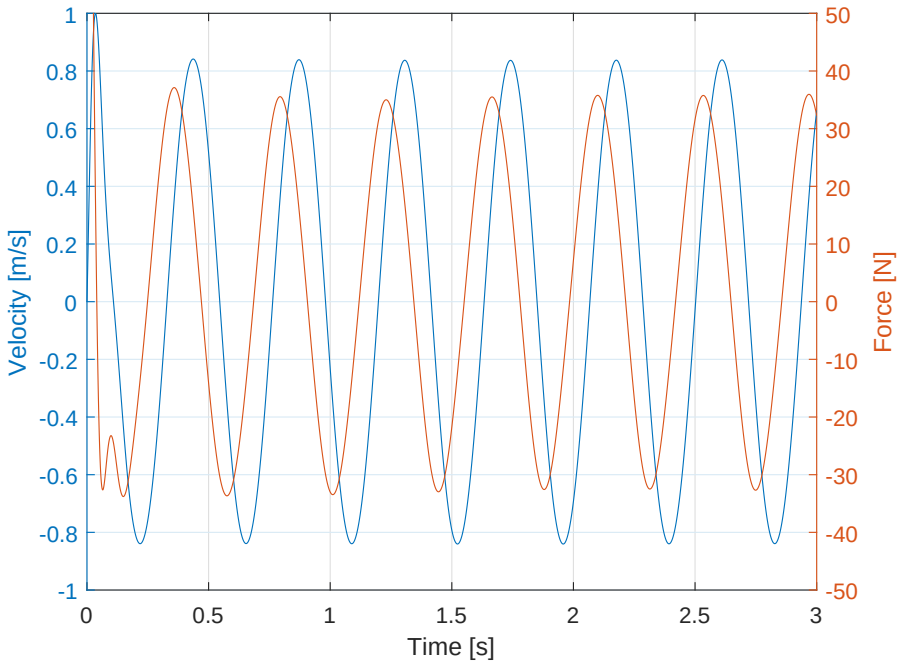

Figure 2.5 – Vertical velocity and user applied force for a sinusoidal velocity profile of 0.8 m/s amplitude at 2.3 Hz, with a 2 kg payload, for the simulated two-DoF manipulator with flexible joints. Initial configuration is $\mathbf{q}_r = [20, 120]^\circ$.

are provided in our previous work (Garant and Gosselin, 2023).

The controller is implemented on a computer running a real-time operating system, ensuring hard real-time at 1 kHz. Communication with the actuators and sensors is done via an EtherCat network in real-time at 1 kHz. The controller gains are iteratively tuned using a Ziegler-Nichols method, first in simulation and then on the physical hardware.

2.7.1 Friction Compensation

In practice, the friction forces present in the gearboxes dampen the response of the actuators. This is particularly notable at low frequencies, where the measured velocity input to the controller fails to generate a sufficient torque output to overcome static friction. In order to mitigate this, rather than increasing the gains to potentially impractical values, we can take advantage of this velocity input by designing a friction compensation term $\boldsymbol{\tau}_\mu$ to be added to the control law given in (2.4). The values of this feedforward term are expressed as

$$\tau_{\mu,i} = A_i \tanh(B_i u_i) \tag{2.14}$$

where the input values u_i are the components of vector $\mathbf{u}$, given by

$$\mathbf{u} = \mathbf{J}_r^{-1} \dot{\mathbf{x}}_f \tag{2.15}$$

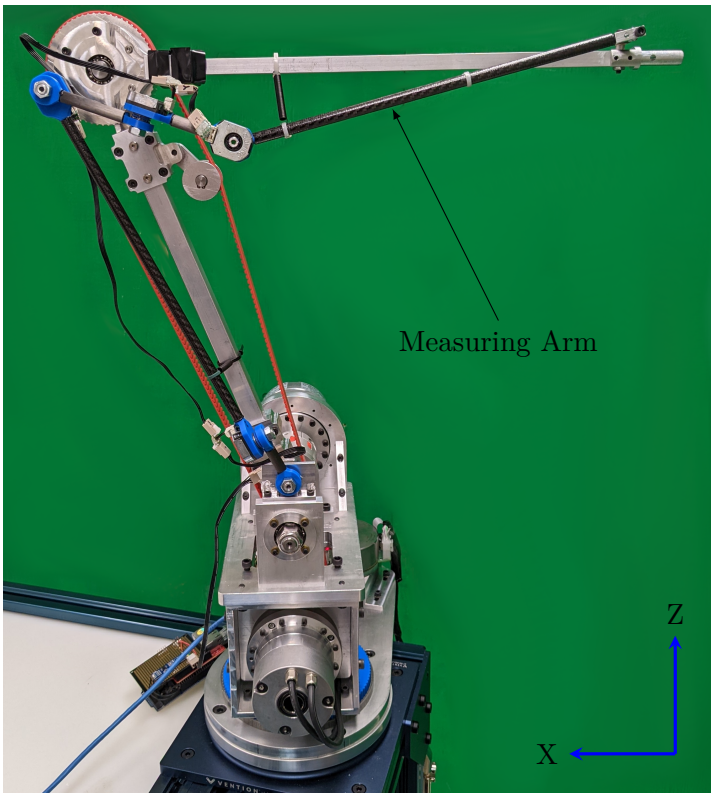

Figure 2.6 – Robotic unit prototype in working configuration.

and where A_i is the scaling factor to match the ith actuator static friction torque and B_i is a tuning parameter governing the zero-crossing slope of the function. It should be noted that the sole purpose of this friction compensation term is to improve the feeling of the user. Therefore, it does not need to exactly match the actual actuator torque. The final control scheme applied at the joints is then

$$\boldsymbol{\tau}_m = \mathbf{K}_v(\mathbf{J}_r^{-1}\dot{\mathbf{x}}_f - \dot{\mathbf{q}}_r) + \boldsymbol{\tau}_g + \boldsymbol{\tau}_\mu. \tag{2.16}$$

2.7.2 Experiment

In order to allow comparisons with results published in the literature, the experiments shown here are performed by interacting with the robotic unit's end-effector. Whole-body interaction is shown in the video accompanying this paper, and briefly discussed in Subsection 2.7.3.

The experimental validation consists in measuring the applied force and resulting end-effector velocity while a user interacts with the manipulator via a force gauge. The payload mass for the experiments is 0.4 kg, corresponding to the mass of the force gauge. The measurement provided by the force gauge is not used in the controller. It is solely used to collect experimental data on the interaction force.

For the first experiment, the user imparted a vertical oscillatory motion at approximately 1

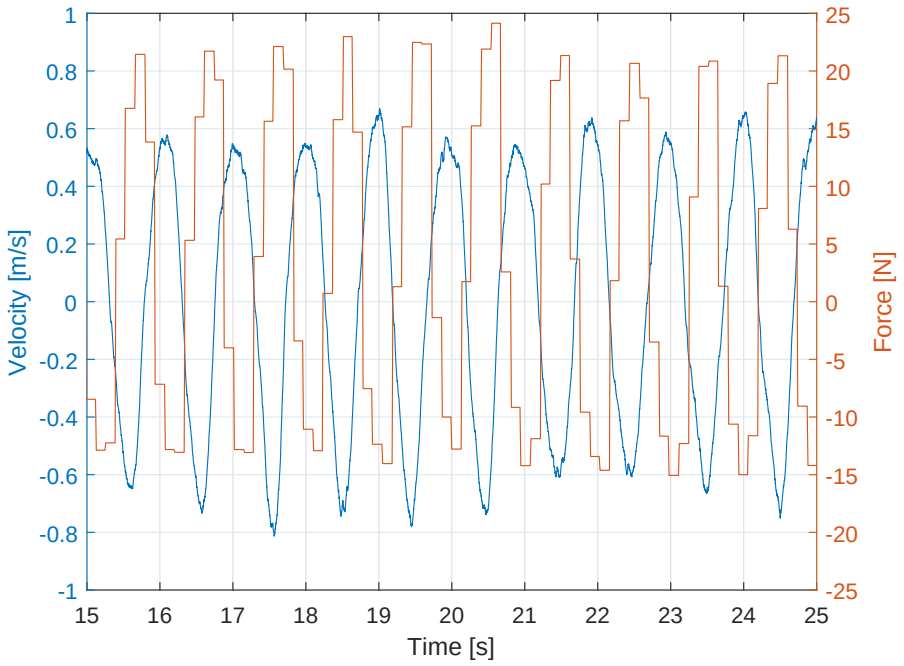

Figure 2.7 – Vertical velocity and user applied force for a sinusoidal velocity profile of 0.6-0.8 m/s amplitude at 1 Hz, with a 0.4 kg payload mounted on the prototype robot shown in Figure 2.6. Nine out of the 27 cycles that were completed are shown.

Hz with a velocity amplitude between 0.6-0.8 m/s, similar to the first simulation experiment. The end-effector velocity was obtained by differentiating the measuring arm position data at 1000 Hz. The force was measured with a digital force gauge in continuous mode at 8 Hz. To compensate for the relatively low sampling rate of the force measurements, 27 cycles were completed. The results for 9 of those cycles, which include the maximum recorded force and velocity during the experiment, are shown in Figure 2.7. The maximum recorded force was 24.14 N.

The objective of the second experiment was to measure the interaction force required to initiate movement from the robot and guide it at low speed. To do so, the user applied a slowly increasing force until the manipulator started moving, then stopped and changed direction. This was first repeated five times in the vertical direction, followed by four times in the horizontal direction. The data collection methodology was unchanged from the first experiment. The results are shown in Figure 2.8. The maximum recorded force was 11.94 N for peak velocities ranging between 0.03-0.04 m/s.

For the third experiment, the force gauge was set to peak mode, thereby increasing its sampling rate to 1000 Hz but restricting the measurements to maximum values only. The user then imparted the fastest possible vertical motion at the end-effector. This particular user achieved a consistent 3 Hz motion. After 18 cycles, the maximum recorded force was 22.72 N

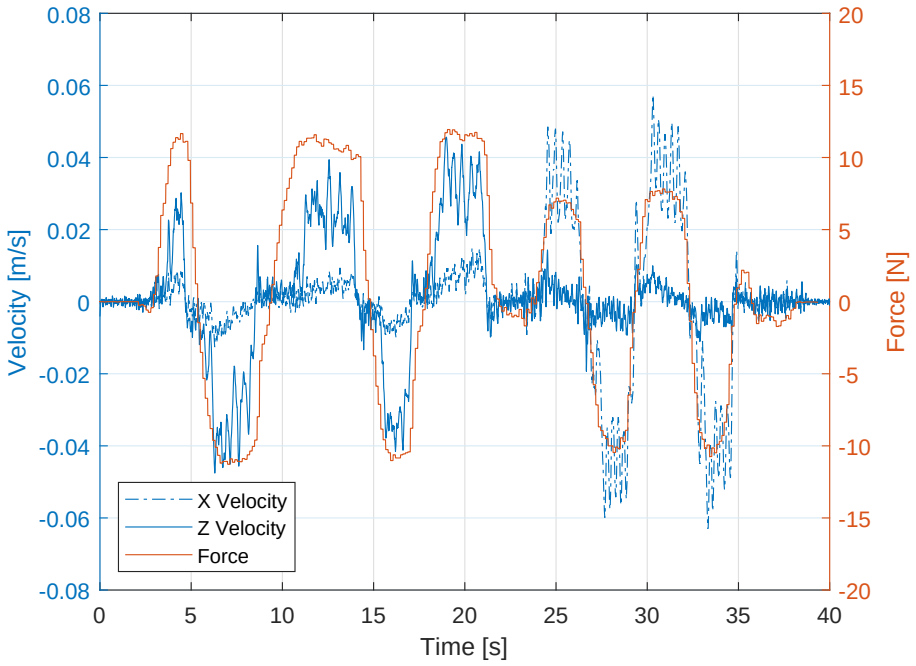

Figure 2.8 – Vertical (Z) and horizontal (X) velocity and user applied force at low speed with a 0.4 kg payload mounted on the prototype robot shown in Figure 2.6. Respectively four and five cycles were tested in the X and Z directions.

and the maximum velocity was 0.88 m/s. These results are included in Table 2.2, which presents a summary of the relevant experimental results.

Table 2.2 – Experimental Results Summary

Max Velocity	**Frequency**	**Number of cycles**	**Max Force**
0.06 m/s	< 0.2 Hz	9	11.94 N
0.81 m/s	1 Hz	27	24.14 N
0.88 m/s	3 Hz	18	22.72 N

2.7.3 Video

The video attachment [1] to this paper shows, in this order:

— General user-guided motion via the end-effector.

— The low interaction forces required to move the manipulator in all 3 directions (including out-of-plane) by using just one finger.

— An example application where the end-effector is guided to waypoints that could be recorded for teach and repeat tasks.

1. Video available on the Laval University Robotics Laboratory Youtube channel.

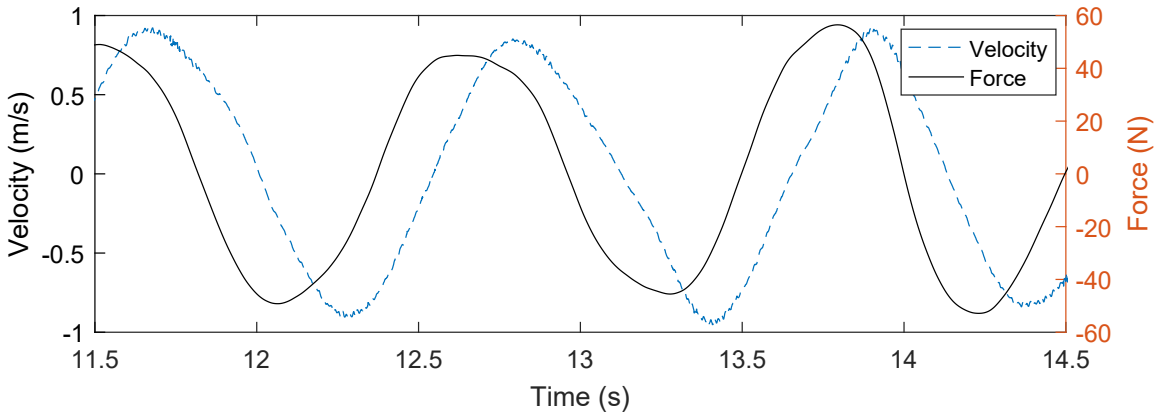

Figure 2.9 – Velocity and user applied force for a sinusoidal velocity profile of 0.8 m/s amplitude at 1 Hz for a KUKA LWR manipulator in a similar configuration, for reference, as reported in Laliberté and Gosselin (2022).

— Whole-body pHRI with low interaction forces exemplified by using just one finger on the links of the manipulator.

— Robustness against impacts (high force, short contact time), demonstrating the stability of the controller.

— High-bandwidth interaction (continuous contact) at over 2 Hz in the vertical and horizontal directions.

2.8 Discussion

By comparing experimental and simulation results, we can conclude that, in practice, friction plays a major role in the pHRI dynamics at low speed. The 24 N maximum measured force at 1 Hz is indeed higher than predicted by the frictionless simulation, but remains acceptable for intuitive pHRI. For instance, in a previous paper (Laliberté and Gosselin, 2022), a similar task where a user imparts a sinusoidal velocity profile was executed on a KUKA LWR robot in a similar configuration. In this case, the user applied force, measured with an end-effector mounted force-torque sensor, reached peak values above 50 N for a similar (0.8 m/s, 1 Hz) profile, as shown in Figure 2.9. Finally, the simulation results also show that the proposed control is equally functional in the absence of friction, i.e., that the control does not rely on the stabilising or damping effect of friction.

The third practical experiment demonstrated a similar but slightly lower force (approx. 23 N) for a motion profile with much higher dynamics (0.88 m/s, 3 Hz). While this result may seem counterintuitive at first, it is a natural consequence of friction, and of the type of control used. Indeed, when the measured velocity inputs are low, the proportional command sent to the actuators is barely sufficient to overcome stiction. Conversely, at high velocity, friction

becomes negligible against the high value of the actuator commands. Therefore, the robotic unit behaves more intuitively for a human user when executing tasks with higher dynamics.

The force needed to initiate the motion of the robotic unit and move it at very low speeds was measured at a very low 12 N. For reference, althought the context is different, in Safeea et al. (2019), a slightly higher 15 N force was needed to move a KUKA iiwa collaborative robot at a similar velocity of 40 mm/s, even with the help of a force/torque sensor at the end-effector. Again, the robotic unit and associated control method proposed here only uses displacement and velocity inputs, and as such does not require force/torque data.

Finally, it is worth restating that the interaction forces were measured at the end-effector for comparison purposes. In practice, the proposed concept allows the user to interact simultaneously at *any* point on the robot, thus splitting the actual required effort between each of the user's arms.

2.9 Conclusion

This paper investigated the use of non-collocated proprioceptive sensing for intuitive pHRI with flexible manipulators. The proposed approach relies on the use of a passive measuring arm, consisting of a serial chain of lightweight links and encoders, mounted in parallel with the manipulator. By providing end-effector deflection measurements relative to the base, the device allows the user to interact with the manipulator at any point along its structure, even though the actuators are not backdrivable. The proposed control scheme is a simple joint velocity controller where the set-point is the mapping of the measured end-point velocity into the joint-space through the rigid Jacobian. Simulation results indicate good performance even in the absence of joint damping. The proposed approach was also validated on a physical flexible-joint flexible-link 3-DoF serial robot prototype. The test results indicated peak forces under 25 N for tasks with high dynamics, which is at least 50% lower than the same task performed on a commercial KUKA cobot. At low speed, the forces were comparable to (but still lower than) other reported experiments in the literature, without requiring force-torque feedback.

Currently, the proposed control scheme however does not allow explicit control of the interaction dynamics. Therefore, future works will investigate the possibility of prescribing a specific dynamic behaviour at the end-effector, similar to classical impedance or admittance control.

Appendix

Theoretically, the velocity relationship from Section 2.5.2,

$$\mathbf{J}_r^{-1}\dot{\mathbf{x}}_f = \dot{\mathbf{q}}_\theta \tag{2.17}$$

is not exact if the manipulator has flexible links. Assume then that

$$\mathbf{J}_r^{-1}\dot{\mathbf{x}}_f = \dot{\mathbf{q}}_\theta + \delta\dot{\mathbf{q}}_\theta \tag{2.18}$$

where $\delta\dot{\mathbf{q}}_\theta$ is the result of link compliance, which can be interpreted as a disturbance acting on $\dot{\mathbf{q}}_\theta$.

Substituting (2.18) into the actuators dynamics given in (2.11) and rearranging yields

$$\mathbf{M}_r\ddot{\mathbf{q}}_r + \mathbf{K}_\theta(\mathbf{q}_r - \mathbf{q}_\theta) + \mathbf{K}_v(\dot{\mathbf{q}}_r - \dot{\mathbf{q}}_\theta) - \mathbf{K}_v(\delta\dot{\mathbf{q}}_\theta) = \mathbf{0} \tag{2.19}$$

which is a decoupled system of equations with one output and two inputs, $\mathbf{q}_\theta$ and $\delta\dot{\mathbf{q}}_\theta$. The total output $\mathbf{q}_r$ can then be considered a superposition of the response to each input. The response to $\mathbf{q}_\theta$ is given in Section 2.5.2. From (2.19), we find the response to $\delta\dot{\mathbf{q}}_\theta$, in the Laplace domain, given by the transfer function

$$q_{r,i}(s) = \frac{k_{v,i}}{m_{r,i}s^2 + k_{v,i}s + k_{\theta,i}} s\delta q_{\theta,i}(s) \tag{2.20}$$

where $m_{r,i}$, $k_{v,i}$ and $k_{\theta,i}$ are the positive values of the inertia, the control gain and the stiffness of the ith joint, respectively. By inspection, we can observe that the system in (2.20) is stable. Figure 2.10 shows the frequency response of $\mathbf{q}_r$ with respect to the $\delta\mathbf{q}_\theta$ input for different gain values and for realistic values of joint parameters. In practice, gain values are in the order of 10^2 and in the context of pHRI, frequencies are under 3 Hz. Considering the very low amplification in this frequency range, we can conclude that the deviation from the assumption introduced in Section 2.5.2 due to link compliance has a negligible impact on the actuator dynamics.

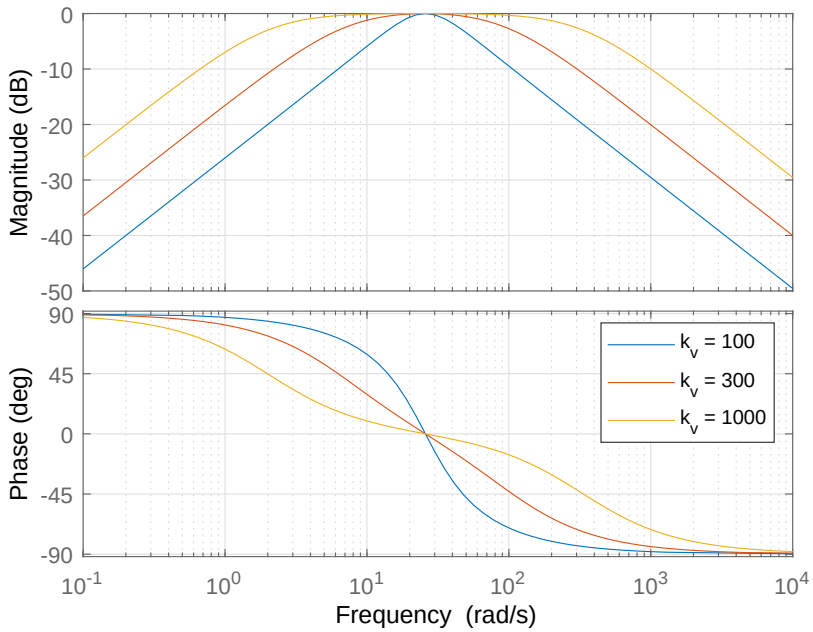

Figure 2.10 – Frequency response of $q_{r,i}$ with respect to $\delta q_{\theta,i}$, with $m_{r,i} = 3$ kgm^2 and $k_{\theta,i} = 2000$ Nm/rad.

2.10 Bibliographie

S. L. Aaron and R. B. Stein. Comparison of an EMG-controlled prosthesis and the normal human biceps brachii muscle. *American journal of physical medicine*, 55(1) :1–14, feb 1976. ISSN 0002-9491.

M. Abdallah, A. Chen, A. Campeau-Lecours, and C. Gosselin. How to reduce the impedance for pHRI : Admittance control or underactuation ? *Mechatronics*, 84 :102768, jun 2022. ISSN 09574158. doi : 10.1016/j.mechatronics.2022.102768.

G. Boucher, T. Laliberté, and C. Gosselin. Mechanical Design of a Low-Impedance 6-Degree-of-Freedom Displacement Sensor for Intuitive Physical Human–Robot Interaction. *Journal of Mechanisms and Robotics*, 13(2), apr 2021. ISSN 1942-4302. doi : 10.1115/1.4049191.

S. R. Buss and J.-S. Kim. Selectively Damped Least Squares for Inverse Kinematics. *Journal of Graphics Tools*, 10(3) :37–49, jan 2005. ISSN 1086-7651. doi : 10.1080/2151237X.2005.10129202.

A. De Luca and B. Siciliano. An asymptotically stable joint PD controller for robot arms with flexible links under gravity. In *[1992] Proceedings of the 31st IEEE Conference on Decision and Control*, pages 325–326. IEEE, 1992. ISBN 0-7803-0872-7. doi : 10.1109/CDC.1992.371728.

N. Dehio, J. Smith, D. L. Wigand, P. Mohammadi, M. Mistry, and J. J. Steil. Enabling impedance-based physical human–multi–robot collaboration : Experiments with four torque-controlled manipulators. *The International Journal of Robotics Research*, 41(1) :68–84, jan 2022. ISSN 0278-3649. doi : 10.1177/02783649211053650.

C. Della Santina. Flexible Manipulators. In *Encyclopedia of Robotics*, pages 1–15. Springer Berlin Heidelberg, Berlin, Heidelberg, 2021. doi : 10.1007/978-3-642-41610-1_182-1.

J. P. W. Flemming. Monitoring the location of a robot hand. U.S. Patent 4119212A, jul 1977.

X. Garant and C. Gosselin. Noncollocated Proprioceptive Sensing for Lightweight Flexible Robotic Manipulators. *IEEE/ASME Transactions on Mechatronics*, pages 1–12, 2023. ISSN 1083-4435. doi : 10.1109/TMECH.2023.3263108.

P. L. García, S. Crispel, E. Saerens, T. Verstraten, and D. Lefeber. Compact Gearboxes for Modern Robotics : A Review. *Frontiers in Robotics and AI*, 7 :103, aug 2020. ISSN 2296-9144. doi : 10.3389/frobt.2020.00103.

D. V. Gealy, S. McKinley, B. Yi, P. Wu, P. R. Downey, G. Balke, A. Zhao, M. Guo, R. Thomasson, A. Sinclair, P. Cuellar, Z. McCarthy, and P. Abbeel. Quasi-direct drive for low-cost compliant robotic manipulation. *Proceedings - IEEE International Conference on Robotics and Automation*, 2019-May :437–443, may 2019. doi : 10.1109/ICRA.2019.8794236.

S. Gong. A novel ultra-precision integrated robotic system. *Robotica*, 23(4) :501–513, jul 2005. ISSN 0263-5747. doi : 10.1017/S0263574704001171.

A. Grädener and L. Rokeach. Arrangement for an articulated arm robot and method for determining the positioning of a mount for an end effector of an articulated arm robot. International Patent WO2019011381A1, jan 2019.

S. Haddadin and E. Croft. Physical Human–Robot Interaction. In O. Siciliano Bruno and Khatib, editor, *Springer Handbook of Robotics*, pages 1835–1874. Springer International Publishing, Cham, 2016. ISBN 978-3-319-32552-1. doi : 10.1007/978-3-319-32552-1_69.

S. Haddadin, K. Krieger, N. Mansfeld, and A. Albu-Schaffer. On impact decoupling properties of elastic robots and time optimal velocity maximization on joint level. In *2012 IEEE/RSJ International Conference on Intelligent Robots and Systems*, pages 5089–5096. IEEE, oct 2012. ISBN 978-1-4673-1736-8. doi : 10.1109/IROS.2012.6385913.

A. Q. Keemink, H. van der Kooij, and A. H. Stienen. Admittance control for physical human–robot interaction. *The International Journal of Robotics Research*, 37(11) :1421–1444, sep 2018. ISSN 0278-3649. doi : 10.1177/0278364918768950.

C. T. Kiang, A. Spowage, and C. K. Yoong. Review of Control and Sensor System of Flexible Manipulator. *Journal of Intelligent & Robotic Systems*, 77(1) :187–213, jan 2015. ISSN 0921-0296. doi : 10.1007/s10846-014-0071-4.

T. Laliberté and C. Gosselin. Low-Impedance Displacement Sensors for Intuitive Physical Human–Robot Interaction : Motion Guidance, Design, and Prototyping. *IEEE Transactions on Robotics*, 38(3) :1518–1530, jun 2022. ISSN 1552-3098. doi : 10.1109/TRO.2021.3121610.

D. P. Losey, C. G. McDonald, E. Battaglia, and M. K. O'Malley. A Review of Intent Detection, Arbitration, and Communication Aspects of Shared Control for Physical Human–Robot Interaction. *Applied Mechanics Reviews*, 70(1), jan 2018. ISSN 0003-6900. doi : 10.1115/1.4039145.

K. Merckaert, A. De Beir, N. Adriaens, I. El Makrini, R. Van Ham, and B. Vanderborght. Independent load carrying and measurement manipulator robot arm for improved payload to mass ratio. *Robotics and Computer-Integrated Manufacturing*, 53 :135–140, oct 2018. ISSN 0736-5845. doi : 10.1016/J.RCIM.2018.04.001.

F. Muller, J. Jakel, J. Suchy, and U. Thomas. Stability of Nonlinear Time-Delay Systems Describing Human–Robot Interaction. *IEEE/ASME Transactions on Mechatronics*, 24(6) : 2696–2705, dec 2019. ISSN 1083-4435. doi : 10.1109/TMECH.2019.2939907.

C. Ott. Modeling of Flexible Joint Robots. In *Cartesian Impedance Control of Redundant and Flexible-Joint Robots*, pages 13–27. Springer Berlin Heidelberg, Berlin, Heidelberg, 2008. doi : 10.1007/978-3-540-69255-3_2.

M. Safeea, P. Neto, and R. Bearee. Precise hand-guiding of redundant manipulators with null space control for in-contact obstacle navigation. In *IECON 2019 - 45th Annual Conference of the IEEE Industrial Electronics Society*, pages 693–698. IEEE, oct 2019. ISBN 978-1-7281-4878-6. doi : 10.1109/IECON.2019.8927766.

T. Steinecker, A. Kurdas, N. Mansfeld, M. Hamad, R. J. Kirschner, S. Abdolshah, and S. Haddadin. Mean Reflected Mass : A Physically Interpretable Metric for Safety Assessment and Posture Optimization in Human-Robot Interaction. In *2022 International Conference on Robotics and Automation (ICRA)*, pages 11209–11215. IEEE, may 2022. ISBN 978-1-7281-9681-7. doi : 10.1109/ICRA46639.2022.9811582.

B. Subudhi and A. Morris. Dynamic modelling, simulation and control of a manipulator with flexible links and joints. *Robotics and Autonomous Systems*, 41(4) :257–270, dec 2002. ISSN 09218890. doi : 10.1016/S0921-8890(02)00295-6.

M. Teyssier, B. Parilusyan, A. Roudaut, and J. Steimle. Human-Like Artificial Skin Sensor for Physical Human-Robot Interaction. In *2021 IEEE International Conference on Robotics*

and Automation (ICRA), pages 3626–3633. IEEE, may 2021. ISBN 978-1-7281-9077-8. doi : 10.1109/ICRA48506.2021.9561152.

K. Wen, T. S. Nguyen, D. Harton, T. Laliberté, and C. Gosselin. A Backdrivable Kinematically Redundant (6+3)-Degree-of-Freedom Hybrid Parallel Robot for Intuitive Sensorless Physical Human–Robot Interaction. *IEEE Transactions on Robotics*, 37(4) :1222–1238, aug 2021. ISSN 1552-3098. doi : 10.1109/TRO.2020.3043723.

S. Yamada and H. Fujimoto. Position-based High Backdrivable Control Using Load-side Encoder and Backlash. *IEEJ Journal of Industry Applications*, 10(2) :142–152, mar 2021. ISSN 2187-1094. doi : 10.1541/ieejjia.20004583.

Chapitre 3

Generalising Series Elastic Actuation to n-dof Flexible-Link Flexible-Joint Robot Control Using End-Point Sensing

3.1 Résumé

Cet article présente une généralisation des concepts reliés aux actionneurs a élasticité en série (*series elastic actuators*, SEA) pour la commande en force de manipulateurs à articulations et membrures flexibles à plusieurs degrés de liberté. En utilisant la mesure de la pose de l'organe terminal, toute la structure d'un manipulateur peut être considérée comme un SEA. Une approche par éléments de raideur localisés (*lumped stiffness*) est proposée pour modéliser la raideur du manipulateur. Une méthodologie simple est proposée pour identifier les paramètres du modèle de raideur. Ce faisant, les schémas de commande développés pour l'interaction physique humain-robot avec les SEA peuvent être transposés à la commande en impédance de manipulateurs flexibles. De plus, la méthode proposée permet d'interagir physiquement avec le robot à n'importe quel endroit sur sa structure. Un résultat connu sur la raideur maximale passivement réalisable avec les SEA à un degré de liberté est généralisé pour les structures flexibles à plusieurs degrés de liberté. Finalement, les schémas de commande proposés sont validés expérimentalement à l'aide d'un manipulateur à membrures et articulations flexibles à trois degrés de liberté.

3.2 Abstract

This paper proposes a task-space generalisation of series elastic actuation concepts for flexible-link flexible-joint robots with any number of degrees of freedom. Using end-point sensing,

the whole body of the flexible manipulator can effectively be considered a task-space series elastic actuator (SEA). A lumped stiffness approach based on the virtual joint method is used to establish an elastostatic model of the flexible manipulator. A simple methodology is proposed in order to identify the elastostatic model parameters. This allows force control of the robot, with notable applications in physical human-robot interaction through admittance and impedance control schemes. Moreover, the proposed method allows whole-body interaction: physical interactions are not limited to the end-effector and can take place at any point on the robot structure. A known result on the maximum passively renderable stiffness for single degree-of-freedom (dof) SEAs is generalised to n-dof flexible structures, providing bounds on the renderable stiffness matrix that apply to any causal controller. Finally, the task-space control schemes derived from the SEA literature are implemented and validated on a 3-dof flexible-link flexible-joint manipulator prototype.

3.3 Introduction

As robots reach more and more environments outside the typical industrial plant, they are bound to increasingly interact with humans and unknown environments. This drive for more flexible and resilient robots has sparked interest in lightweight and physically compliant robotic manipulators. Indeed, flexible components can be seen as a way to encode safety considerations in robots at the hardware level. In this regard, one of the most useful properties of flexible robots is the inertial decoupling of the actuators and the links (De Luca and Book, 2016; Haddadin and Croft, 2016). This ensures that the very large inertia of the actuators is not directly reflected at the end-effector, nor at any point of interaction on the robot.

This philosophy has led to research thrusts exploring the deliberate inclusion of flexible components in robots, with influential works such as Pratt and Williamson (1995) in the field of series elastic actuators (SEAs). Interaction control with SEAs was investigated (Pratt et al., 2004), yielding more specific interesting applications in physical human-robot interaction (pHRI) (Vallery et al., 2008). The passivity limitations and renderable dynamics in such contexts have been an active research topic for the past decades (Tagliamonte and Accoto, 2014; Horibe et al., 2016; Treadway et al., 2017; Losey and O'Malley, 2017) (see Calanca et al. (2017) for a review), with new results still being published (Tosun and Patoglu, 2020; Mengilli et al., 2021; Kenanoglu and Patoglu, 2023; Kenanoglu et al., 2023).

The change of paradigm toward flexible robots also offers the possibility of lowering the mass of robotic manipulators (Merckaert et al., 2018; Garant and Gosselin, 2023) by circumventing the high-stiffness design criterion. This has important implications, notably in the context of pHRI, where mobile mass is one of the main determinants of safety (Haddadin et al., 2008; Haddadin and Croft, 2016; Steinecker et al., 2022).

Unfortunately, model-based control of flexible robots is notoriously difficult, in part due to their very nonlinear and non-minimum phase dynamics (Cannon and Schmitz, 1984; Sayahkarajy et al., 2016; Berger and Lanza, 2021). This has led many research initatives to focus on feedback control of flexible manipulators (see Kiang et al. (2015) for the latest review).

Malzahn *et al.* (Malzahn and Bertram, 2014; Malzahn et al., 2015) were among the first to suggest the idea of leveraging the compliance of robot links for physical interaction, via additional feedback (strain gauges in this case). More recently, the concept of "series elastic links" was introduced in Calanca et al. (2019, 2023). In their approach, link flexibility is lumped at the joint, yielding a model sharing similarities with SEAs. This allows accurate control of the output torque of the device, when combined with a stiffness model of the link. This approach is however currently limited to single-dof systems and torque controlled motors. As a consequence, it is also not clear, given this approach, how to deal with out-of-plane bending of the flexible links.

Therefore, in this paper, in a similar fashion, we propose to leverage the SEA framework for the task-space interaction control of flexible robots. Similarly to classical SEAs, our approach uses end-point sensing along with actuator-side joint positions and a stiffness model of the manipulator to control the interaction force between the end-effector and the environment. This method is applicable to manipulators with any number and any arrangement of dofs, with flexible links, flexible joints, or both. It is also not limited to torque controlled robots and does not require strain feedback.

The generalisation of the SEA concept introduced in this paper does not prescribe a specific end-effector pose measuring technique. Notable examples include computer vision (Sahu et al., 2020; Li et al., 2022) and laser tracking (Tso et al., 2003; Cvitanic et al., 2022). Nevertheless, the present investigation is motivated in part by the authors' previous work, in which a practical "mechanical" end-point sensor (Garant and Gosselin, 2023) was developed for multi-dof flexible manipulators. This sensor system is a passive serial chain of encoders and lightweight links, mounted in parallel with the manipulator, as illustrated in Figure 3.1. This system is well adapted for pHRI applications, where it notably does not suffer from the typical problem of visual occlusions by a human operator (De Luca and Book, 2016). It can also easily accommodate the high sampling rate required for reactive real-time control, which can be challenging with vision systems.

This paper is structured as follows. In Section 3.4, the parallels between SEA control and flexible manipulator control are laid out. An elastostatic model for flexible-joint flexible-link robots is introduced in Section 3.5. Section 3.6 then proposes a methodology for the identification of the elastostatic model parameters. Control methods for pHRI, and their limitations, are discussed in Section 3.7 and Section 3.8 respectively. The experimental setup

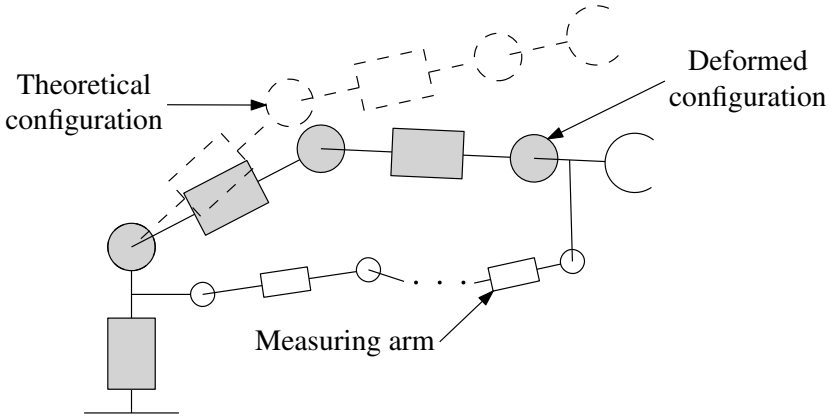

Figure 3.1 – Schematic representation of a flexible manipulator in a theoretical configuration (dashed white), deformed configuration under load (solid grey) and measuring arm (solid white), from Garant and Gosselin (2023).

and results are presented in Section 3.9. Conclusions are drawn in Section 3.10.

3.4 Series Elasticity Analogy

Series elastic actuators integrate a flexible element, generally a spring, between the motor and the driven load. When the link-side position is measured and the stiffness properties of the elastic element are known, the value of the applied force or torque on the load can be inferred according to the relationship

$$\tau_s = k_m(\theta - q) \tag{3.1}$$

where θ is the motor position, q is the link-side position and k_m is the stiffness of the elastic component.

It is proposed that with the help of end-point sensing, the whole body of the manipulator can be considered a task-space series elastic actuator. Indeed, as shown in Figure 3.2, when linearising at the point of operation, the generalised elastic forces acting on the load can be expressed as

$$\mathbf{F}_s = \mathbf{K}_x(\boldsymbol{\theta})[\mathbf{x}(\boldsymbol{\theta}) - \mathbf{x}_f] \tag{3.2}$$

where $\boldsymbol{\theta}$ are the motor positions, $\mathbf{K}_x(\boldsymbol{\theta})$ is the configuration dependent task-space stiffness matrix, $\mathbf{x}(\boldsymbol{\theta})$ is the virtual task-space motor position given by the forward kinematics of the rigid manipulator model, and $\mathbf{x}_f$ is the actual measured end-effector pose.

If we again consider $\mathbf{K}_x$ to be constant at the point of operation, equation (3.2) can be diagonalised, since the stiffness matrix is symmetric by definition. Therefore, we obtain a system of decoupled 1-dof equations and the vast body of literature on SEAs and their analysis can be directly transposed to the problem at hand.

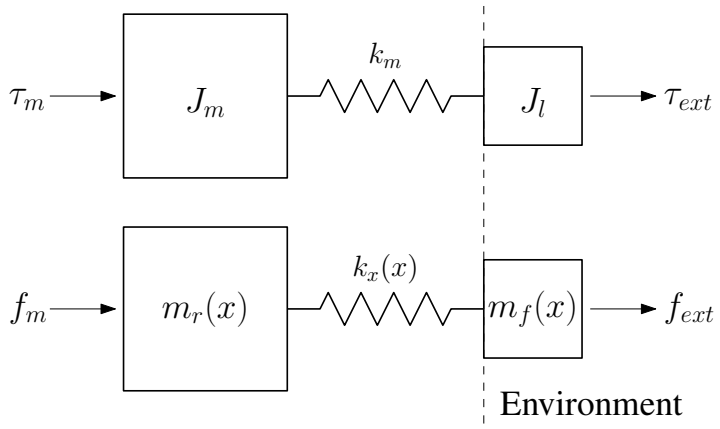

Figure 3.2 – Analogy between a SEA (top) and a flexible manipulator with end-point sensing (bottom). In the SEA case, τ_m is the torque acting on the motor with inertia J_m, k_m is the torsional stiffness of the spring element, and J_l is the inertia of the sprung load, upon which an external torque τ_{ext} can act. In the linearised flexible manipulator, f_m is the force acting on the reflected "rigid" mass (motor rotors) $m_r(x)$ in task-space, $k_x(x)$ is the task-space stiffness of the manipulator, and $m_f(x)$ is the reflected "flexible" mass (mobile links and payload) in task-space, upon which an external force f_{ext} can act.

For the remainder of this paper, it is assumed that the manipulator is neither in a singular configuration, nor near a singularity. In other words, it is assumed that the Jacobian matrix of the manipulator $\mathbf{J}$ is well-conditioned.

3.5 Lumped Stiffness Model

As expressed in Section 3.4, a condition for the application of the SEA framework to the control of flexible robots with end-point sensing is the knowledge of the task-space stiffness matrix of the manipulator. This matrix, $\mathbf{K}_x$, is however configuration dependent and a stiffness model must therefore be established.

While flexible-joint manipulators stiffness models are straightforward, flexible-link manipulators are notoriously challenging in that regard (Subedi et al., 2020; Della Santina, 2021).

The flexible-link flexible-joint manipulator elastostatic model proposed in this paper is established using the virtual joint model (VJM) (Wu et al., 2022). The manipulator is therefore modelled as an augmented flexible-joint rigid-link model, where link stiffness is lumped in equivalent torsional springs at virtual joints.

In the proposed flexible model, each actuated joint of the robot is replaced by a virtual 3-dof (spherical) joint which lumps joint compliance and link deformation (in-plane bending, out-of-plane bending and torsion). The virtual axis coincident with the actuated joint combines joint deformation and one of the deformation modes of the following link. When torsion

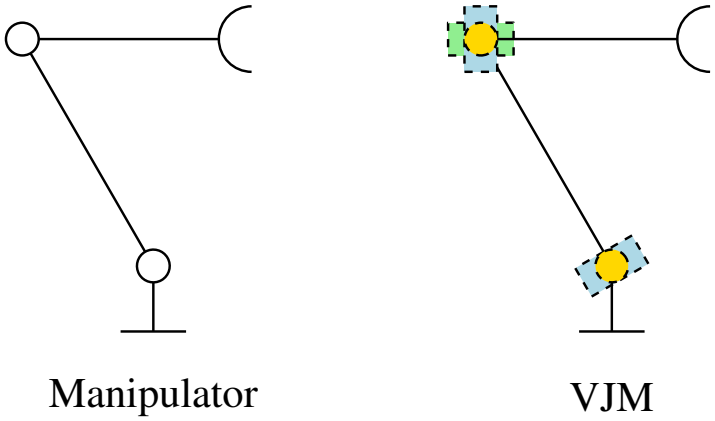

Figure 3.3 – Example elastostatic model (right) of a 2-dof flexible link flexible-joint manipulator (left) using the VJM. The yellow virtual joints lump the compliance of the actuated joints and in-plane link bending. The light blue virtual joints model out-of-plane link bending. The light green virtual joint models the longitudinal torsion of the distal link. In this example, the torsion of the proximal link is neglected.

of the links is neglected, one of the virtual axes can generally be removed, and the virtual joint reduces to two dofs. A simple example is shown in Figure 3.3. The 3-dof VJM was investigated in Abele et al. (2008) and proved suitable for the identification of the elastostatic model of serial manipulators.

The VJM allows a straightforward representation of the manipulator's stiffness properties with the configuration invariant and symmetric virtual joint stiffness matrix $\mathbf{K}_q$. The task-space stiffness matrix of the manipulator is then defined as

$$\mathbf{K}_x = \mathbf{J}_v^{-T} \mathbf{K}_q \mathbf{J}_v^{-1} \tag{3.3}$$

where $\mathbf{J}_v(\boldsymbol{\theta}_v)$ is the Jacobian matrix of the VJM manipulator, computed with the array of virtual joint values $\boldsymbol{\theta}_v$. By definition, the VJM almost always results in more joint-space dofs than task-space dofs, yielding a rectangular matrix $\mathbf{J}_v$. Therefore, a more convenient approach uses the task-space compliance matrix $\mathbf{C}_x$, expressed as

$$\mathbf{C}_x = \mathbf{J}_v \mathbf{C}_q \mathbf{J}_v^T \tag{3.4}$$

where $\mathbf{C}_q = \mathbf{K}_q^{-1}$ is the symmetric virtual joint compliance matrix and

$$\mathbf{K}_x = \mathbf{C}_x^{-1} \tag{3.5}$$

by definition.

3.6 Model Identification

Whenever the equivalent lumped torsional stiffness of the links cannot be modelled with classical methods (such as in Calanca et al. (2019)) or through finite element analysis (FEA),

the lumped model parameters must be experimentally identified.

The proposed identification method uses an end-effector mounted force-torque (FT) sensor and takes advantage of the available end-point displacement measurements. End-point sensing simplifies the identification of the stiffness parameters by providing the $\Delta\mathbf{x}_f$ displacement *from static equilibrium* corresponding to an applied force $\mathbf{F}$, according to the task-space force-displacement relationship

$$\Delta\mathbf{x}_f = \mathbf{C}_x\mathbf{F}. \tag{3.6}$$

The vector of task-space forces and torques $\mathbf{F}$ is then provided by the FT sensor reading, as long as the manipulator is in static equilibrium. Otherwise, due to the 'distal' positioning of the FT sensor at the end-effector, inertial effects and damping forces would distort the readings.

Substituting (3.4) in (3.6) makes the $\mathbf{C}_q$ parameters explicit, yielding

$$\Delta\mathbf{x}_f = \mathbf{J}_v\mathbf{C}_q\mathbf{J}_v^T\mathbf{F}. \tag{3.7}$$

The identification problem then reduces to finding values of $\mathbf{C}_q$ which minimise the norm of the residual error. However, as expressed in Klimchik et al. (2015), without additional constraints on $\mathbf{C}_q$, the identified matrix may notably lose its positive definiteness and symmetry properties, in contradiction with the physical sense. Therefore, the problem becomes

$$\begin{aligned} \min_{\mathbf{C}_q} \quad & \sum_{k=1}^{p} ||\Delta\mathbf{x}_{f,k} - \mathbf{J}_{v,k}\mathbf{C}_q\mathbf{J}_{v,k}^T\mathbf{F}_k||^2 \\ \text{s.t.} \quad & \mathbf{C}_q = \mathbf{C}_q^T \\ & c_{q,ii} > 0, \quad i = 1 \dots n \end{aligned} \tag{3.8}$$

where p is the number of data points and n is the number of joints in the VJM. In essence, this objective function is equivalent to taking the square of the Frobenius norm of the difference between two p-column dataset matrices, except that it keeps $\mathbf{C}_q$ explicit without complex block matrix multiplications.

If $\mathbf{C}_q$ is assumed to be diagonal, that is, if there is no kinematic coupling between the joints, the problem further reduces to

$$\begin{aligned} \min_{\mathbf{c}_q} \quad & \sum_{k=1}^{p} ||\Delta\mathbf{x}_{f,k} - \mathbf{J}_{v,k}\text{diag}(\mathbf{c}_q)\mathbf{J}_{v,k}^T\mathbf{F}_k||^2 \\ \text{s.t.} \quad & \mathbf{c}_q > 0 \end{aligned} \tag{3.9}$$

where $\mathbf{c}_q$ is the array of the diagonal components of $\mathbf{C}_q$.

Naturally, for a proper identification of the model parameters, the dataset must cover a range of typical manipulator configurations and must include force measurements in all directions

for each of these configurations. It should also be noted that joint stiffness and in-plane link stiffness cannot be separately identified when they are lumped at the same virtual joint axis: a single combined virtual joint stiffness is identified. For further practical considerations, we refer the reader to Klimchik et al. (2015); Wu et al. (2022).

Finally, with the proper dataset, the problem can be solved using a constrained nonlinear optimisation algorithm. The implementation of such algorithms is readily available in commercial computer packages such as MATLAB's `fmincon` function. Once the elastostatic model parameters have been identified, the FT sensor is no longer required.

3.7 Control Methods for pHRI

The SEA framework is of particular interest when dealing with interaction control for pHRI. The SEA control schemes for pHRI generally consist of an outer loop governing the desired interaction dynamics and an inner torque or velocity loop for low-level control of the actuator.

Even though there exist notable examples of robots with torque controlled actuators, such as the KUKA LBR, they remain an exception. Likewise, direct-drive (Wen et al., 2021) or quasi-direct drive actuators (Gealy et al., 2019) are also good candidates for low-level torque control (through current control) because they are less subject to the effect of nonlinearities such as friction and backlash in the transmission. However, due to their lower torque density, they are difficult to implement in serial robots. The practicality of the inner torque loop is therefore limited.

The inner velocity loop has the advantage of reducing the effect of friction in the transmission, effectively making the actuators a pure motion source, rather than a torque source. The interaction controllers using low-level velocity control are therefore applicable to a wider range of actuators. For this reason, this paper focuses on the two most common realisations of such controllers which are velocity-sourced impedance control (VSIC) and admittance control.

3.7.1 Admittance Control

The SEA implementation of admittance control, in contrast with its rigid counterpart (see Keemink et al. (2018)), does not require a FT sensor. The force input can instead be provided by a collocated position sensor, a spring compression sensor, and knowledge of the spring stiffness, as first investigated in Pratt et al. (2004).

The practical implementation of this admittance controller for a n-dof flexible manipulator is shown in Figure 3.4. At each time step, the estimated task-space compliance of the manipulator $\tilde{\mathbf{C}}_x$ is computed using the VJM and (3.4). The interaction force is then computed using (3.2), in which $\mathbf{x}_f$ is directly measured by the end-point position sensor. The interaction force is fed to the desired admittance $\mathbf{Z}^{-1}$ in order to prescribe a desired task-space

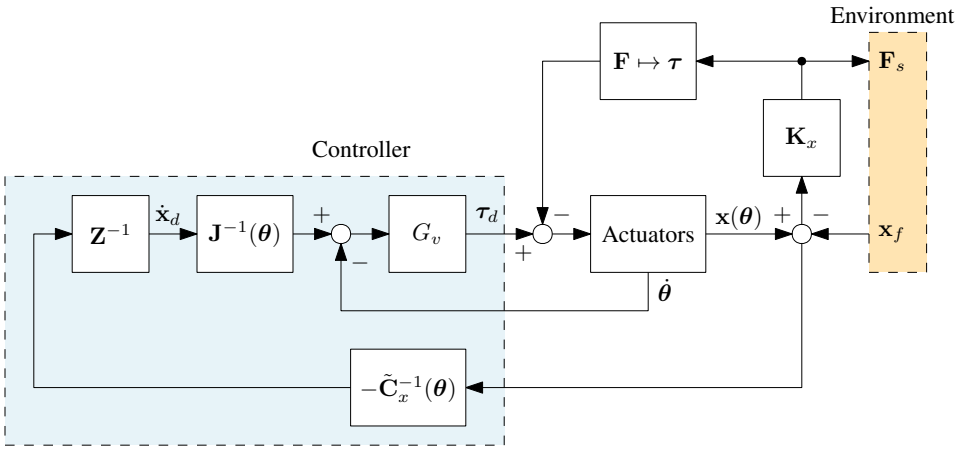

Figure 3.4 – Practical implementation of the SEA admittance control scheme on a n-dof flexible manipulator. An outer force loop shapes the apparent admittance. An inner loop controls the position or velocity with collocated feedback.

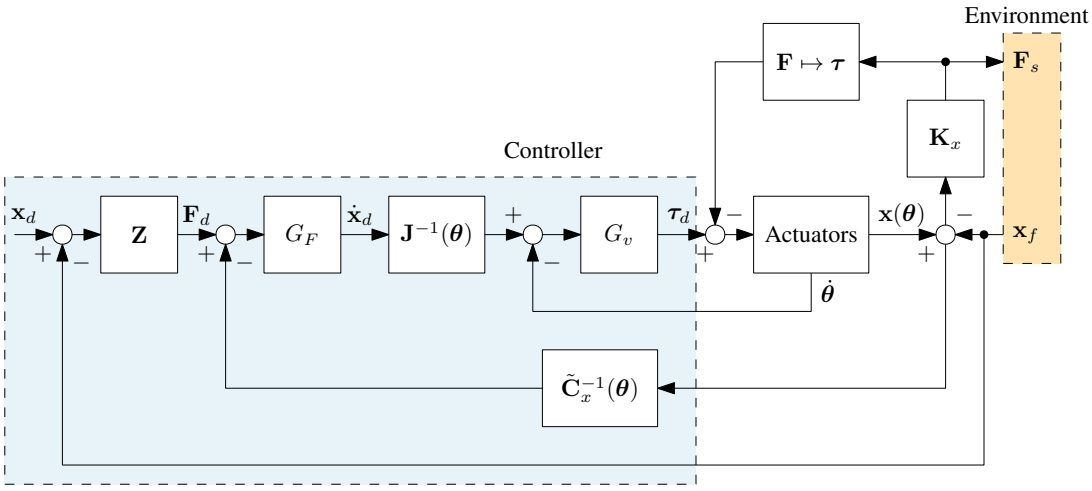

Figure 3.5 – Practical implementation of the SEA VSIC control scheme on a n-dof flexible manipulator. An outer loop shapes the apparent impedance. An inner force loop regulates the spring interaction force through a cascaded velocity control loop with collocated feedback.

velocity $\dot{\mathbf{x}}_d$. The desired task-space velocity is mapped to joint velocities via the inverse of the Jacobian matrix. These are then fed to a joint velocity controller G_v. This controller generally includes proportional and integral (PI) action, and can also include any required feedforward term, such as gravity compensation torques.

3.7.2 Velocity-Sourced Impedance Control

Velocity-sourced impedance control uses a slightly different approach to interaction control. The practical implementation of this impedance controller for a n-dof flexible manipulator is shown in Figure 3.5. In this approach, the environment induces a displacement from a desired

set-point, which dictates the desired interaction force according to the desired impedance $\mathbf{Z}$. The actual interaction force between the environment and the actuators is estimated with the VJM and (3.4). Due to friction, direct and accurate force control of the actuators is not possible. The interaction force is therefore indirectly controlled by a force controller G_F and a joint velocity controller G_v, in cascade. The force controller (generally proportional or proportional-integral) outputs a desired task-space velocity, which is then mapped onto the joint space and fed to the inner velocity loop. The gravity compensation torques can be included in the G_v velocity controller when required.

3.8 Passivity, Coupled Stability and Limitations

Proving the coupled stability of a flexible robot interacting with an arbitrary environment is challenging. In the case of pHRI, a typical conservative approach in the literature involves the concept of passivity and the assumption that the human behaves passively. If the two ports of the coupled system, respectively the human and the robot, are passive, then the whole system can be considered passive and stable (Tagliamonte and Accoto, 2014).

The passivity of the manipulator port depends on its inherent dynamics, the type of control used and, in the case of pHRI, the desired end-point dynamics. Several studies have investigated the passivity of single-dof SEAs (Tagliamonte and Accoto, 2014; Losey and O'Malley, 2017; Kenanoglu et al., 2023; Kenanoglu and Patoglu, 2023) and their results are directly applicable to the task-space control of flexible manipulators with end-point feedback. For the sake of conciseness, only the main conclusions are reported here and the reader is referred to the respective studies for the mathematical proofs and details.

3.8.1 Maximum Apparent Stiffness

Under the passivity framework, the maximum desired apparent stiffness $\mathbf{K}_d$, rendered at the non-collocated position $\mathbf{x}_f$, is bounded by the actual stiffness $\mathbf{K}_x$ of the manipulator.

This has been proven in the past for various specific SEA control architectures with only one output variable (Calanca et al., 2017). Recently, it was proven that in the 1-dof case, the passivity condition

$$k_d \leq k_x \tag{3.10}$$

holds *for all causal control architectures* (Kenanoglu and Patoglu, 2023). To the best of the authors' knowledge, this result has not yet been generalised to higher dof spaces. The following derivation is thus relevant for applications in interaction control of multi-dof flexible structures.

A corollary to (3.10) is that, for a given arbitrary displacement Δx, the potential energy U_d associated with the apparent stiffness must always be less than or equal to the potential

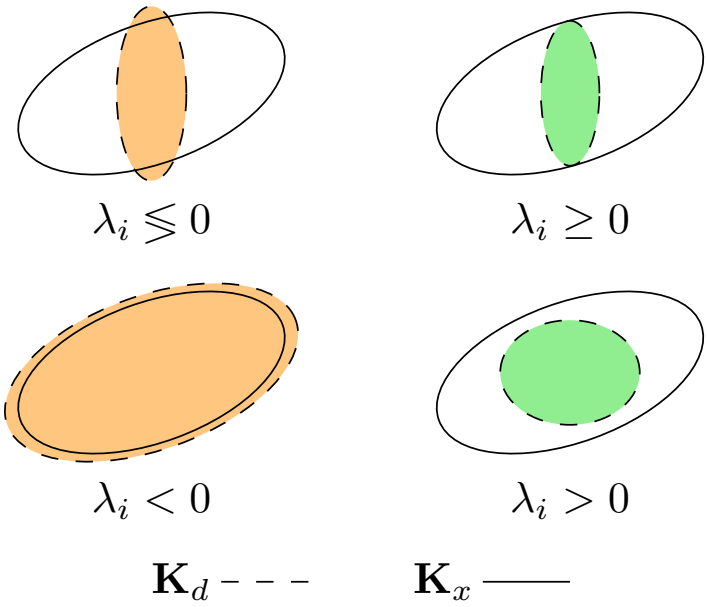

Figure 3.6 – Stiffness ellipsoids of $\mathbf{K}_x$ (actual stiffness, solid line) and $\mathbf{K}_d$ (desired stiffness, dashed line), with the corresponding eigenvalues λ_i of $\mathbf{S} = \mathbf{K}_x - \mathbf{K}_d$. Under passivity, only the upper right and lower right examples are allowed.

energy U_x associated with the physical system stiffness, such that

$$U_x - U_d \geq 0. \tag{3.11}$$

In matrix form, (3.11) can be written as

$$\begin{aligned} \frac{1}{2}\Delta\mathbf{x}^T\mathbf{K}_x\Delta\mathbf{x} - \frac{1}{2}\Delta\mathbf{x}^T\mathbf{K}_d\Delta\mathbf{x} &\geq 0 \\ \frac{1}{2}\Delta\mathbf{x}^T[\mathbf{K}_x - \mathbf{K}_d]\Delta\mathbf{x} &\geq 0 \\ \frac{1}{2}\Delta\mathbf{x}^T\mathbf{S}\Delta\mathbf{x} &\geq 0 \end{aligned} \tag{3.12}$$

where $\mathbf{S}$ is a "stiffness difference matrix" (Khanna, 1965; Khanna and Hooley, 1966). From (3.12), we can conclude that the maximum stiffness condition, alternatively expressed as an energy condition in (3.11), is fulfilled if and only if $\mathbf{S}$ is positive definite or positive semi-definite. Equivalently, (3.12) is valid if and only if all of the eigenvalues of $\mathbf{S} = \mathbf{K}_x - \mathbf{K}_d$ are greater than or equal to zero.

In more visual terms, and perhaps more intuitively, condition (3.12) ensures that the ellipsoid represented by the mapping of unit displacements to efforts through $\mathbf{K}_d$ is fully inscribed within the similar ellipsoid represented by $\mathbf{K}_x$. This is illustrated in Figure 3.6. The ellipsoid condition was hinted at in Vallery et al. (2008), but was based on the mapping of the joint stiffness matrix to task-space. The energy approach developed here is more general, directly applicable to any task-space stiffness matrix, and makes no assumption on the source of the compliance.

Moreover, causality is implied in interaction control, since a disturbance cannot be acted upon unless it is first measured. Therefore, *in an interaction context, a flexible robot cannot passively render an apparent task-space stiffness that is greater than its inherent task-space stiffness.* The only exception is if link-side damping is considered Lee et al. (2021).

3.8.2 Other Limitations

1. At high frequency, the closed-loop impedance of the system converges to the physical stiffness of the flexible manipulator (Vallery et al., 2008; Treadway et al., 2017). This is again true for all causal controllers, due to high-frequency roll-off (Kenanoglu and Patoglu, 2023).
2. Except during quasi-static operation, a user interacting with the robot does not directly feel the elastic forces acting on the "environment" as defined in (3.2). Specifically, by inspection, we observe that the external force also depends on the inertial effects of the payload and the reflected inertia of the links. This is due to the force sensing element being the robot's structure itself, which is positioned in-between the actuators and the reflected inertia (Sensinger and Ff. Weir, 2006), as shown in Figure 3.2. The "post-sensor inertia" (as defined in Keemink et al. (2018)) is therefore always felt by the user.
3. Neither VSIC nor admittance control can passively render pure Voigt model (VM) dynamics (parallel spring-damper) at the non-collocated coordinates $\mathbf{x}_f$ (Calanca et al., 2017). In the context of pHRI, VSIC is notably limited to rendering pure spring models or null impedance. Comparatively, admittance control can render an approximated VM where stiffness acts on the non-collocated position and damping acts on the collocated velocities, such that

$$\mathbf{F}_d = \mathbf{K}_d[\mathbf{x}_d - \mathbf{x}_f] + \mathbf{D}_d[-\dot{\mathbf{x}}(\dot{\boldsymbol{\theta}})] + \mathbf{F}_g(\boldsymbol{\theta}) \tag{3.13}$$

   where $\mathbf{D}_d$ is the desired task-space damping, and $\mathbf{F}_g(\boldsymbol{\theta})$ are the gravity compensation forces. Admittance control can also render a pure spring and null impedance.

3.8.3 Controller Equivalence

The admittance control scheme introduced above, first proposed in Pratt et al. (2004) and referred to as "collocated admittance control" (CAC) in Calanca et al. (2017), is in many cases a direct equivalent to VSIC. To the best of the authors' knowledge, they were nonetheless treated as separate methods in the literature, up to now.

Let us assume that a pure virtual stiffness is to be rendered using VSIC (omitting gravity compensation for the sake of clarity), such that

$$\mathbf{F}_d = \mathbf{K}_d[\mathbf{x}_d - \mathbf{x}_f]. \tag{3.14}$$

The use of an integral term in the force controller G_F has been proven to not significantly affect the system response while also having the potential to jeopardize passivity (Tosun and Patoglu, 2020). Thus, if the force controller G_F only uses proportional action, the prescribed velocity can then be computed as

$$\dot{\mathbf{x}}_d = \mathbf{G}_F[\mathbf{F}_d - \mathbf{F}_s] \tag{3.15}$$

$$\dot{\mathbf{x}}_d = \mathbf{G}_F[\mathbf{K}_d[\mathbf{x}_d - \mathbf{x}_f] - \mathbf{K}_x[\mathbf{x}(\boldsymbol{\theta}) - \mathbf{x}_f]] \tag{3.16}$$

where $\mathbf{G}_F$ is a diagonal matrix of proportional gains to be tuned.

Let us then assume that an approximate VM is to be rendered with CAC. In this case, the prescribed velocity is computed from the desired dynamics as

$$\dot{\mathbf{x}}_d = \mathbf{D}_d^{-1}[\mathbf{K}_d[\mathbf{x}_d - \mathbf{x}_f] - \mathbf{F}_s] \tag{3.17}$$

$$\dot{\mathbf{x}}_d = \mathbf{D}_d^{-1}[\mathbf{K}_d[\mathbf{x}_d - \mathbf{x}_f] - \mathbf{K}_x[\mathbf{x}(\boldsymbol{\theta}) - \mathbf{x}_f]]. \tag{3.18}$$

We can clearly see that the proportional gain $\mathbf{G}_F$ in VSIC, when rendering a pure stiffness, is directly equivalent to the inverse of the desired collocated damping matrix $\mathbf{D}_d$ of the approximate VM in CAC. This result has an intuitive interpretation: as the proportional gain in VSIC is increased, the dynamics tend towards a pure spring, exhibiting less damping, and vice versa when the gain is decreased. In other words, increasing $\mathbf{G}_F$ is akin to lowering $\mathbf{D}_d$. For the remainder of this paper, VSIC and CAC are therefore treated as equivalent.

3.9 Experiment

3.9.1 Experimental Setup

In this section, an experimental validation of the proposed solution is carried out on a physical prototype. The integrated robotic unit, shown in Figure 3.7, comprises a 3-DoF positioning manipulator with flexible links and joints, and a 5-DoF measuring arm. The measuring arm is connected to the manipulator's end-effector through a spherical joint. This restricts the measurements to position only (no orientation) but ensures that the robotic unit can move and deflect freely in all spatial directions, while also ensuring that the measuring arm has two redundant DoFs. The end-point measurement is given by the forward kinematics of the measuring arm, with a precision of 0.2 to 0.4 mm depending on the configuration.

The first joint and first mobile link of the robot are considered rigid because their stiffness is much larger than that of the subsequent links and joints. The second link is connected to the second actuator through a flexible coupling with a torsional stiffness rated at 2600 Nm/rad. The third link is connected to the third actuator through a series of synchronous belt transmissions, yielding an equivalent computed torsional stiffness of 1300 Nm/rad at the third joint. For comparison, joint stiffness values above 10^5 Nm/rad can generally be considered

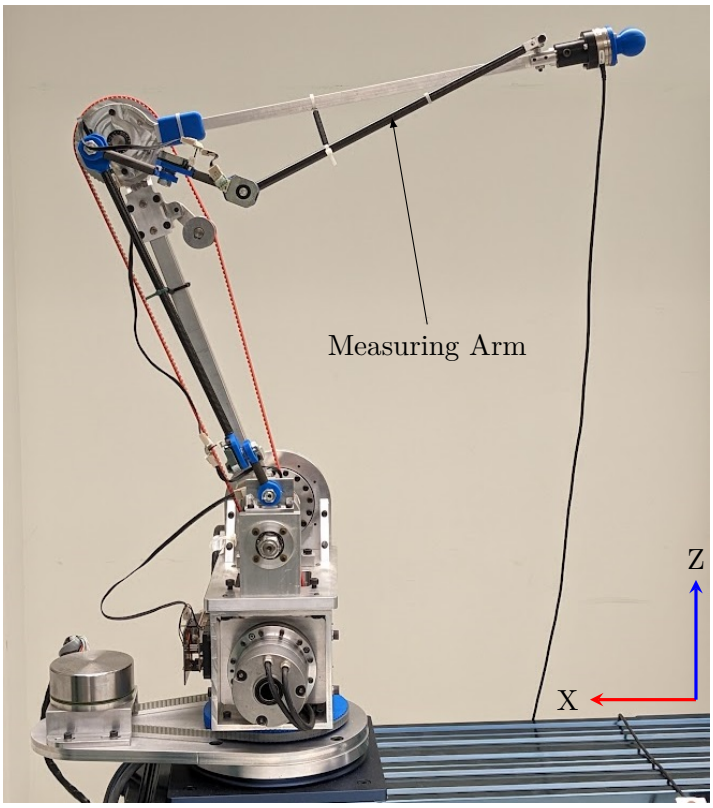

Figure 3.7 – Robotic unit prototype in working configuration. The FT sensor mounted on the end-effector provides ground truth measurement and is not used in the controller.

rigid (Zollo et al., 2005). The slender links of the manipulator were purposely designed to allow up to approximately 2 cm of deflection at the tip in the worst conditions (fully extended, 5 kg payload).

The first actuator is a Maxon EC-90 direct drive motor coupled to a 4.54:1 synchronous belt reducer. The second actuator is a Harmonic Drive SHA-25 with a 121:1 integrated gearbox. The third actuator is a Harmonic Drive SHA-20 with a 81:1 built-in reducer coupled to a synchronous belt transmission, yielding an effective ratio of 90:1 at the third joint. More details on the design of the prototype and measuring arm are provided in the authors' previous work (Garant and Gosselin, 2023).

The control schemes are implemented on a real-time computer running at 1 kHz and communicating with the hardware through an EtherCat network. The user-applied force is measured with an ATI Mini40 sensor mounted at the end-effector. The FT sensor is *not* used to control the robot.

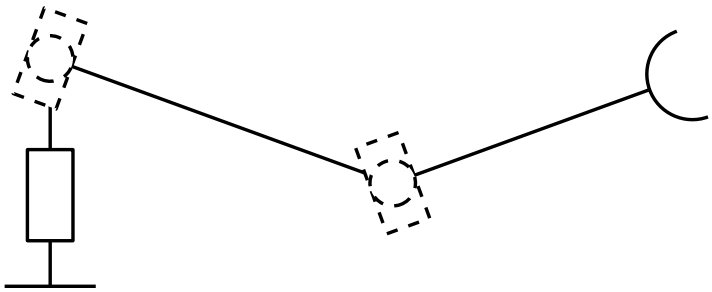

Figure 3.8 – Virtual joint model of the experimental prototype. A virtual joint is added at the origin of the second and third actuated joints to model out-of-plane link bending.

3.9.2 Elastostatic Model Identification

The elastostatic model of the manipulator was identified using the VJM as described in Section 3.5. The first joint and first link were considered rigid. Longitudinal torsion of the links was neglected. Two virtual dofs were therefore added to model the out-of-plane bending of the distal links. The in-plane bending stiffness of the distal links was lumped with the joint torsional stiffness. The resulting virtual joint model is shown in Figure 3.8. The identified stiffness matrix of the four virtual flexible joints, in Nm/rad, is

$$\mathbf{K}_q = \begin{bmatrix} 2370.5 & 0 & 0 & 0 \\ 0 & 844.9 & 0 & 0 \\ 0 & 0 & 493.3 & 0 \\ 0 & 0 & 0 & 619.4 \end{bmatrix}. \tag{3.19}$$

For the experiments, the robot is positioned in a typical working configuration. This configuration is shown in Figure 3.7. The actual task-space stiffness of the manipulator in N/m in this configuration, according to the identified VJM and (3.4) is

$$\mathbf{K}_x = \begin{bmatrix} 8733.4 & -591.1 & -2088.7 \\ -591.1 & 2057.3 & 292.3 \\ -2088.7 & 292.3 & 2917.1 \end{bmatrix}. \tag{3.20}$$

From (3.20), we see that the physical stiffness values of the manipulator in this configuration are strongly coupled in the X and Z directions, with weaker but non-negligible couplings in the other directions.

3.9.3 Results

As a first proof of concept, the experiment is aimed at assessing the ability of the controller to render a prescribed stiffness. A user physically interacts with the manipulator through an end-effector mounted FT sensor by applying forces in every spatial direction. The experiment is carried out in quasi-static conditions to neglect damping and inertial effects. This allows

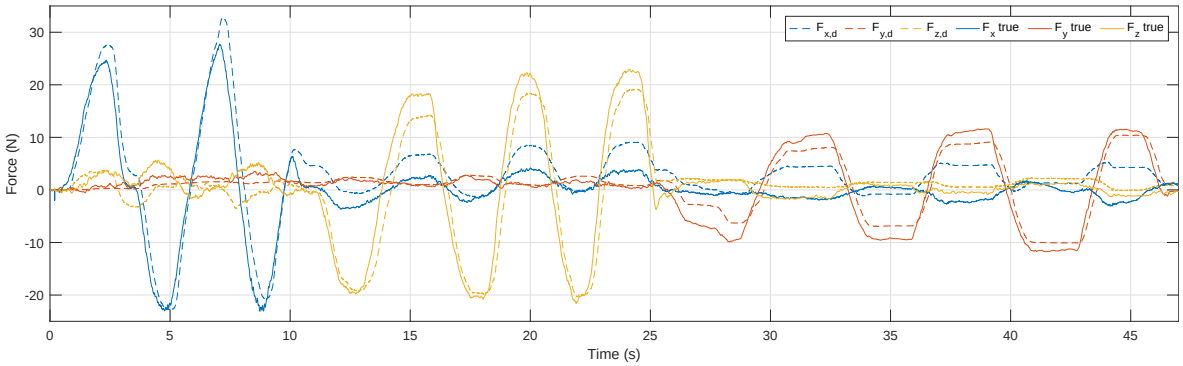

Figure 3.9 – Force versus time for a desired stiffness of 1000 N/m, 400 N/m and 1000 N/m respectively in the X,Y and Z directions. Actual force measurements from a FT sensor are plotted with solid lines. Desired forces, computed as $\mathbf{K}_d[\mathbf{x}_d - \mathbf{x}_f]$ are plotted with dashed lines.

the comparison of the actual ground truth force measurements from the FT sensor against end-effector displacement values.

In the first case, the manipulator is tasked with rendering a stiffness of

$$\mathbf{K}_d = \begin{bmatrix} 1000 & 0 & 0 \\ 0 & 400 & 0 \\ 0 & 0 & 1000 \end{bmatrix} \tag{3.21}$$

in N/m, where the lower value of 400 N/m in the Y direction is selected to prevent the torque saturation of the weaker base actuator of this specific prototype. An example dataset for a scenario where forces are applied sequentially in each of the Cartesian directions is shown in Figure 3.9.

In the second case, the manipulator is tasked with rendering a lower stiffness of

$$\mathbf{K}_d = \begin{bmatrix} 500 & 0 & 0 \\ 0 & 300 & 0 \\ 0 & 0 & 500 \end{bmatrix} \tag{3.22}$$

in N/m. An example dataset for a scenario where forces are applied sequentially in each of the Cartesian directions is shown in Figure 3.10.

The RMS and mean error values for each dataset are shown in Table 3.1. The error at each time step k is computed as

$$e = ||\mathbf{K}_d \Delta\mathbf{x}_{f,k} - \mathbf{F}_k|| \tag{3.23}$$

where the data for $\Delta\mathbf{x}_{f,k}$ and $\mathbf{F}_k$ are provided respectively by the measuring arm and the FT sensor at 1 kHz.

Relative error analysis is impractical due to the numerous zero-crossings of the reference signals. Therefore, as an additional proxy for the accuracy of control method, the rendered

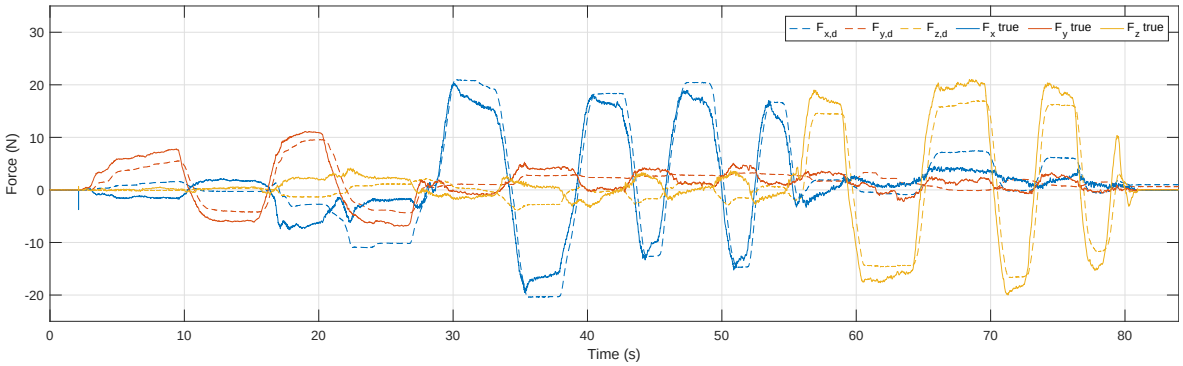

Figure 3.10 – Force versus time for a desired stiffness of 500 N/m, 300 N/m and 500 N/m respectively in the X,Y and Z directions. Actual force measurements from a FT sensor are plotted with solid lines. Desired forces, computed as $\mathbf{K}_d[\mathbf{x}_d - \mathbf{x}_f]$ are plotted with dashed lines.

Table 3.1 – RMS and mean error for each dataset

Desired Stiffness (N/m)	**Mean Error (N)**	**RMS Error (N)**
diag(1000, 400, 1000)	4.72	5.26
diag(500, 300, 500)	4.44	4.90

stiffness is identified using the methodology from Section 3.6. The overall resulting task-space stiffness under interaction control $\mathbf{K}_{d,r}$ is computed with

$$\begin{aligned} \min_{\mathbf{K}_{d,r}} \quad & \sum_{k=1}^{p} ||\mathbf{K}_{d,r}\Delta\mathbf{x}_{f,k} - \mathbf{F}_k||^2 \\ \text{s.t.} \quad & \mathbf{K}_{d,r} = \mathbf{K}_{d,r}^T \\ & k_{d,ii} > 0, \quad i = 1 \dots n \end{aligned} \tag{3.24}$$

where p is again the number of data points in the dataset.

The resulting best-fit task-space stiffness matrix for the first dataset is

$$\mathbf{K}_{d,r} = \begin{bmatrix} 806.6 & -112.0 & -45.9 \\ -112.0 & 478.6 & 18.8 \\ -45.9 & 18.8 & 1039.1 \end{bmatrix} \tag{3.25}$$

in N/m, with 47000 samples. The resulting effective stiffness matrix $\mathbf{K}_{d,r}$ is as desired very weakly coupled, compared to the actual intrinsic stiffness $\mathbf{K}_x$ of the manipulator. This is especially notable in the XZ off-diagonal elements, which were lowered from an absolute value of over 2000 N/m to less than 50 N/m through control methods, as shown in Figure 3.11. The identified stiffness is 19.4% lower than the desired stiffness in the X direction, 19.6% higher in the Y direction, and 3.9% higher in the Z direction.

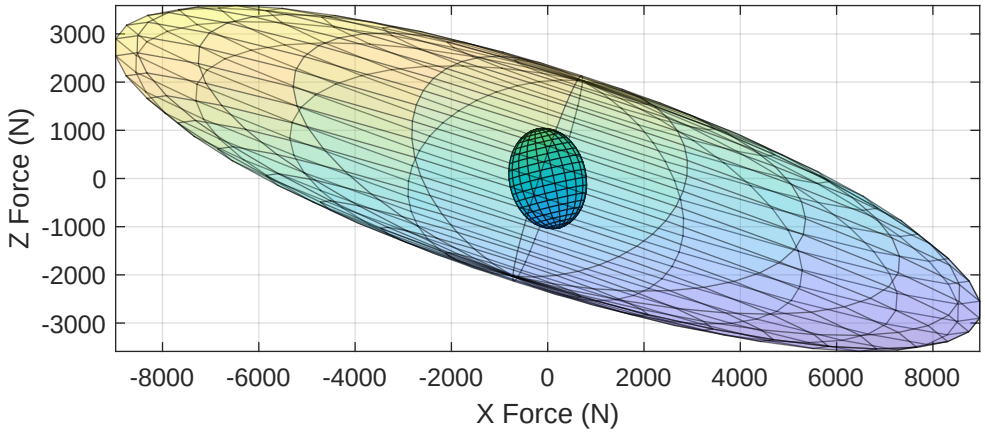

Figure 3.11 – Ellipsoid of the intrinsic stiffness $\mathbf{K}_x$ (outer, transparent) and of the resulting stiffness $\mathbf{K}_{d,r}$ (inscribed, solid), for $\mathbf{K}_d = \text{diag}(1000, 400, 1000)$. The view facing the XZ plane is shown, highlighting the weak coupling in $\mathbf{K}_{d,r}$, whereas the rotated ellipsoid of $\mathbf{K}_x$ indicates strong XZ coupling.

The best-fit task-space stiffness matrix for the second dataset is

$$\mathbf{K}_{d,r} = \begin{bmatrix} 411.7 & -62.1 & -58.8 \\ -62.1 & 365.4 & 84.9 \\ -58.8 & 84.9 & 576.6 \end{bmatrix} \tag{3.26}$$

in N/m, with 84000 samples. The resulting stiffness matrix is again weakly coupled, and similar deviations of -16.3%, -19.3% and $+15.5\%$ from the desired values respectively along the X, Y, and Z directions can be observed.

The force versus displacement values are plotted in Figure 3.12 and 3.13. The dry and viscous friction of the actuators, combined with the (low but present) desired damping $\mathbf{D}_d$, result in a clear hysteresis that can be observed in the force-displacement data. Again, mainly due to static friction, the rendered stiffness is not accurate for very small displacements in the order of 0-5 mm. This is consistent with the results in Table 3.1. For larger displacements, the slope of the hysteresis closely matches the desired stiffness value.

Various error sources contribute to the difference between desired and measured force values. First, in theory, perfect rendering of the desired stiffness for a wide range of frequencies, in every Cartesian direction, is only possible with high proportional gain values in $\mathbf{G}_F$ or low damping $\mathbf{D}_d$. Such values however amplify the resonant peaks in the dynamic system response, yielding a lower stability margin. Second, in practice, the FT sensor readings include "post-sensor" effects which skew the error metrics when transitioning from one steady-state position to another. Indeed, the 'desired' force values are derived from displacement values, which naturally lag behind the force signal in these instances. Moreover, the high (and highly

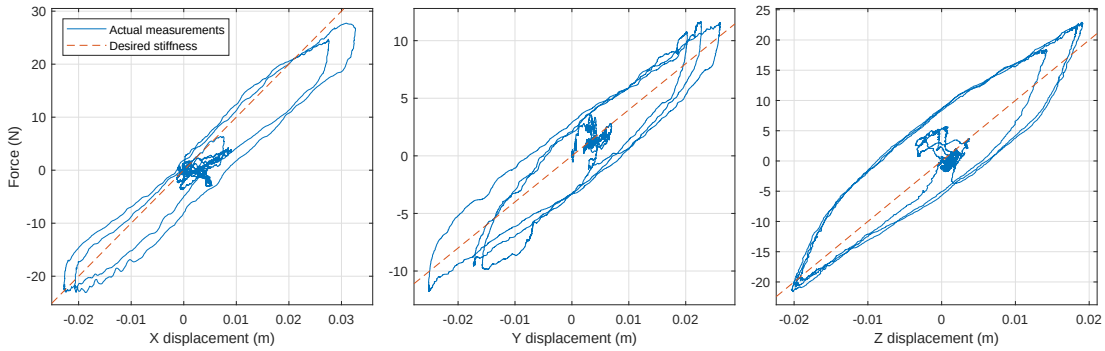

Figure 3.12 – Force versus displacement for a desired stiffness of 1000 N/m, 400 N/m and 1000 N/m respectively in the X,Y and Z directions. Actual measurements are plotted with a solid line. The desired theoretical stiffness slope is plotted with a dashed line.

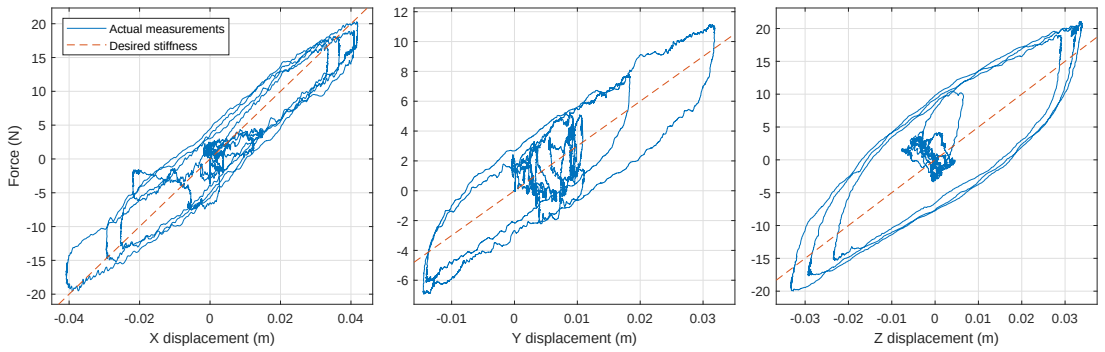

Figure 3.13 – Force versus displacement for a desired stiffness of 500 N/m, 300 N/m and 500 N/m respectively in the X,Y and Z directions. Actual measurements are plotted with a solid line. The desired theoretical stiffness slope is plotted with a dashed line.

nonlinear) friction of the actuators make indirect force control via position/velocity control very challenging, even with a very fast inner loop. Finally, these error sources are also present in the elastostatic model identification. Given this perspective, the results presented in this section are considered satisfactory, in the context of an initial proof of concept.

3.10 Conclusion

This paper presented an interaction control method for flexible-link flexible-joint serial manipulators. The method relies on end-point sensing, which allows indirect force sensing when combined with a manipulator stiffness model. A lumped stiffness approach was proposed for straightforward modelling and identification of the manipulator elastostatic parameters. The proposed control schemes and their stability and passivity analyses were drawn from the established SEA framework in the literature. Through a corollary energy condition, a fundamental result limiting the passively renderable stiffness to the system's intrinsic stiffness was

generalised from 1-dof SEAs to n-dof flexible structures. Velocity-sourced impedance control (VSIC) and admittance control were shown to be equivalent when considering their respective range of renderable dynamics under passivity constraints. Finally, this equivalent task-space impedance/admittance control scheme was implemented on a 3-dof flexible-link flexible-joint manipulator prototype. As a proof of concept, the manipulator successfully rendered two decoupled task-space stiffness matrices, whereas its intrinsic reflected stiffness (without control) was strongly coupled.

While the current accuracy achieved with the prototype can be considered suitable for pHRI and for an initial proof of concept, future work could notably investigate ways to improve the accuracy for more demanding force control applications.

3.11 Bibliographie

E. Abele, S. Rothenbücher, and M. Weigold. Cartesian compliance model for industrial robots using virtual joints. *Production Engineering*, 2(3) :339–343, sep 2008. ISSN 0944-6524. doi : 10.1007/s11740-008-0118-0.

T. Berger and L. Lanza. Output tracking for a non-minimum phase robotic manipulator. *IFAC-PapersOnLine*, 54(9) :178–185, 2021. ISSN 24058963. doi : 10.1016/j.ifacol.2021.06.074.

A. Calanca, R. Muradore, and P. Fiorini. Impedance control of series elastic actuators : Passivity and acceleration-based control. *Mechatronics*, 47 :37–48, nov 2017. ISSN 09574158. doi : 10.1016/j.mechatronics.2017.08.010.

A. Calanca, E. Dimo, R. Vicario, P. Fiorini, M. Serpelloni, and G. Legnani. Introducing Series Elastic Links for Affordable Torque-Controlled Robots. *IEEE Robotics and Automation Letters*, 4(1) :137–144, jan 2019. ISSN 2377-3766. doi : 10.1109/LRA.2018.2878353.

A. Calanca, E. Sartori, and B. Maris. Force control of lightweight series elastic systems using enhanced disturbance observers. *Robotics and Autonomous Systems*, 164 :104407, jun 2023. ISSN 09218890. doi : 10.1016/j.robot.2023.104407.

R. H. Cannon and E. Schmitz. Initial Experiments on the End-Point Control of a Flexible One-Link Robot. *The International Journal of Robotics Research*, 3(3) :62–75, sep 1984. ISSN 0278-3649. doi : 10.1177/027836498400300303.

T. Cvitanic, S. Melkote, and S. Balakirsky. Improved state estimation of a robot end-effector using laser tracker and inertial sensor fusion. *CIRP Journal of Manufacturing Science and Technology*, 38 :51–61, aug 2022. ISSN 17555817. doi : 10.1016/j.cirpj.2022.03.011.

A. De Luca and W. J. Book. Robots with Flexible Elements. In Siciliano Bruno, , and O. Khatib, editors, *Springer Handbook of Robotics*, pages 243–282. Springer International Publishing, Cham, 2016. doi : 10.1007/978-3-319-32552-1_11.

C. Della Santina. Flexible Manipulators. In *Encyclopedia of Robotics*, pages 1–15. Springer Berlin Heidelberg, Berlin, Heidelberg, 2021. doi : 10.1007/978-3-642-41610-1_182-1.

X. Garant and C. Gosselin. Noncollocated Proprioceptive Sensing for Lightweight Flexible Robotic Manipulators. *IEEE/ASME Transactions on Mechatronics*, pages 1–12, 2023. ISSN 1083-4435. doi : 10.1109/TMECH.2023.3263108.

D. V. Gealy, S. McKinley, B. Yi, P. Wu, P. R. Downey, G. Balke, A. Zhao, M. Guo, R. Thomasson, A. Sinclair, P. Cuellar, Z. McCarthy, and P. Abbeel. Quasi-direct drive for low-cost compliant robotic manipulation. *Proceedings - IEEE International Conference on Robotics and Automation*, 2019-May :437–443, may 2019. doi : 10.1109/ICRA.2019.8794236.

S. Haddadin and E. Croft. Physical Human–Robot Interaction. In O. Siciliano Bruno and Khatib, editor, *Springer Handbook of Robotics*, pages 1835–1874. Springer International Publishing, Cham, 2016. ISBN 978-3-319-32552-1. doi : 10.1007/978-3-319-32552-1_69.

S. Haddadin, A. Albu-Schaffer, and G. Hirzinger. The role of the robot mass and velocity in physical human-robot interaction - Part I : Non-constrained blunt impacts. In *2008 IEEE International Conference on Robotics and Automation*, pages 1331–1338. IEEE, may 2008. ISBN 978-1-4244-1646-2. doi : 10.1109/ROBOT.2008.4543388.

T. Horibe, E. Treadway, and R. B. Gillespie. Comparing Series Elasticity and Admittance Control for Haptic Rendering. pages 240–250. 2016. doi : 10.1007/978-3-319-42321-0_22.

A. Q. Keemink, H. van der Kooij, and A. H. Stienen. Admittance control for physical human–robot interaction. *The International Journal of Robotics Research*, 37(11) :1421–1444, sep 2018. ISSN 0278-3649. doi : 10.1177/0278364918768950.

C. U. Kenanoglu and V. Patoglu. A Fundamental Limitation of Passive Spring Rendering With Series Elastic Actuation. *IEEE Transactions on Haptics*, pages 1–6, 2023. ISSN 1939-1412. doi : 10.1109/TOH.2023.3260063.

O. T. Kenanoglu, C. U. Kenanoglu, and V. Patoglu. Effect of Low-Pass Filtering on Passivity and Rendering Performance of Series Elastic Actuation. *IEEE Transactions on Haptics*, pages 1–6, 2023. ISSN 1939-1412. doi : 10.1109/TOH.2023.3273168.

J. Khanna. Criterion for selecting stiffness matrices. *AIAA Journal*, 3(10) :1976–1976, oct 1965. ISSN 0001-1452. doi : 10.2514/3.3303.

J. Khanna and R. F. Hooley. Comparison and evaluation of stiffness matrices. *AIAA Journal*, 4(12) :2105–2111, dec 1966. ISSN 0001-1452. doi : 10.2514/3.3862.

C. T. Kiang, A. Spowage, and C. K. Yoong. Review of Control and Sensor System of Flexible Manipulator. *Journal of Intelligent & Robotic Systems*, 77(1) :187–213, jan 2015. ISSN 0921-0296. doi : 10.1007/s10846-014-0071-4.

A. Klimchik, B. Furet, S. Caro, and A. Pashkevich. Identification of the manipulator stiffness model parameters in industrial environment. *Mechanism and Machine Theory*, 90 :1–22, aug 2015. ISSN 0094114X. doi : 10.1016/j.mechmachtheory.2015.03.002.

H. Lee, J.-H. Ryu, J. Lee, and S. Oh. Passivity Controller Based on Load-Side Damping Assignment for High Stiffness Controlled Series Elastic Actuators. *IEEE Transactions on Industrial Electronics*, 68(1) :871–881, jan 2021. ISSN 0278-0046. doi : 10.1109/TIE.2020.3013751.

K. Li, H. Wang, X. Liang, and Y. Miao. Visual Servoing of Flexible-Link Manipulators by Considering Vibration Suppression Without Deformation Measurements. *IEEE*

Transactions on Cybernetics, 52(11) :12454–12463, nov 2022. ISSN 2168-2267. doi : 10.1109/TCYB.2021.3072779.

D. P. Losey and M. K. O'Malley. Effects of discretization on the K-width of series elastic actuators. In *2017 IEEE International Conference on Robotics and Automation (ICRA)*, pages 421–426. IEEE, may 2017. ISBN 978-1-5090-4633-1. doi : 10.1109/ICRA.2017.7989054.

J. Malzahn and T. Bertram. Collision Detection and Reaction for a Multi-Elastic-Link Robot Arm. *IFAC Proceedings Volumes*, 47(3) :320–325, 2014. ISSN 14746670. doi : 10.3182/20140824-6-ZA-1003.01545.

J. Malzahn, R. Schloss, and T. Bertram. Link elasticity exploited for payload estimation and force control. In *2015 IEEE/RSJ International Conference on Intelligent Robots and Systems (IROS)*, pages 1508–1513. IEEE, sep 2015. ISBN 978-1-4799-9994-1. doi : 10.1109/IROS.2015.7353567.

U. Mengilli, Z. O. Orhan, U. Caliskan, and V. Patoglu. Passivity of Series Damped Elastic Actuation under Velocity-Sourced Impedance Control. In *2021 IEEE World Haptics Conference (WHC)*, pages 379–384. IEEE, jul 2021. ISBN 978-1-6654-1871-3. doi : 10.1109/WHC49131.2021.9517159.

K. Merckaert, A. De Beir, N. Adriaens, I. El Makrini, R. Van Ham, and B. Vanderborght. Independent load carrying and measurement manipulator robot arm for improved payload to mass ratio. *Robotics and Computer-Integrated Manufacturing*, 53 :135–140, oct 2018. ISSN 0736-5845. doi : 10.1016/J.RCIM.2018.04.001.

G. Pratt and M. Williamson. Series elastic actuators. In *Proceedings 1995 IEEE/RSJ International Conference on Intelligent Robots and Systems. Human Robot Interaction and Cooperative Robots*, volume 1, pages 399–406. IEEE Comput. Soc. Press, 1995. ISBN 0-8186-7108-4. doi : 10.1109/IROS.1995.525827.

G. Pratt, P. Willisson, C. Bolton, and A. Hofman. Late motor processing in low-impedance robots : impedance control of series-elastic actuators. In *Proceedings of the 2004 American Control Conference*, pages 3245–3251 vol.4. IEEE, 2004. ISBN 0-7803-8335-4. doi : 10.23919/ACC.2004.1384410.

U. K. Sahu, D. Patra, and B. Subudhi. Vision-based tip position tracking control of two-link flexible manipulator. *IET Cyber-Systems and Robotics*, 2(2) :53–66, jun 2020. ISSN 2631-6315. doi : 10.1049/iet-csr.2019.0035.

M. Sayahkarajy, Z. Mohamed, and A. A. Mohd Faudzi. Review of modelling and control of flexible-link manipulators. *Proceedings of the Institution of Mechanical Engineers, Part I : Journal of Systems and Control Engineering*, 230(8) :861–873, sep 2016. ISSN 0959-6518. doi : 10.1177/0959651816642099.

J. Sensinger and R. Ff. Weir. Improvements to Series Elastic Actuators. In *2006 2nd IEEE/ASME International Conference on Mechatronics and Embedded Systems and Applications*, pages 1–7. IEEE, aug 2006. ISBN 0-7803-9721-5. doi : 10.1109/MESA.2006.296927.

T. Steinecker, A. Kurdas, N. Mansfeld, M. Hamad, R. J. Kirschner, S. Abdolshah, and S. Haddadin. Mean Reflected Mass : A Physically Interpretable Metric for Safety Assessment and Posture Optimization in Human-Robot Interaction. In *2022 International Conference on Robotics and Automation (ICRA)*, pages 11209–11215. IEEE, may 2022. ISBN 978-1-7281-9681-7. doi : 10.1109/ICRA46639.2022.9811582.

D. Subedi, I. Tyapin, and G. Hovland. Review on Modeling and Control of Flexible Link Manipulators. *Modeling, Identification and Control : A Norwegian Research Bulletin*, 41 (3) :141–163, 2020. ISSN 0332-7353. doi : 10.4173/mic.2020.3.2.

N. L. Tagliamonte and D. Accoto. Passivity constraints for the impedance control of series elastic actuators. *Proceedings of the Institution of Mechanical Engineers, Part I : Journal of Systems and Control Engineering*, 228(3) :138–153, mar 2014. ISSN 0959-6518. doi : 10.1177/0959651813511615.

F. E. Tosun and V. Patoglu. Necessary and Sufficient Conditions for the Passivity of Impedance Rendering With Velocity-Sourced Series Elastic Actuation. *IEEE Transactions on Robotics*, 36(3) :757–772, jun 2020. ISSN 1552-3098. doi : 10.1109/TRO.2019.2962332.

E. Treadway, Y. Yang, and R. B. Gillespie. Decomposing the performance of admittance and series elastic haptic rendering architectures. In *2017 IEEE World Haptics Conference (WHC)*, pages 346–351. IEEE, jun 2017. ISBN 978-1-5090-1425-5. doi : 10.1109/WHC.2017.7989926.

S. Tso, T. Yang, W. Xu, and Z. Sun. Vibration control for a flexible-link robot arm with deflection feedback. *International Journal of Non-Linear Mechanics*, 38(1) :51–62, jan 2003. ISSN 0020-7462. doi : 10.1016/S0020-7462(01)00040-3.

H. Vallery, J. Veneman, E. van Asseldonk, R. Ekkelenkamp, M. Buss, and H. van Der Kooij. Compliant actuation of rehabilitation robots. *IEEE Robotics & Automation Magazine*, 15 (3) :60–69, sep 2008. ISSN 1070-9932. doi : 10.1109/MRA.2008.927689.

K. Wen, T. S. Nguyen, D. Harton, T. Laliberté, and C. Gosselin. A Backdrivable Kinematically Redundant (6+3)-Degree-of-Freedom Hybrid Parallel Robot for Intuitive Sensorless Physical Human–Robot Interaction. *IEEE Transactions on Robotics*, 37(4) :1222–1238, aug 2021. ISSN 1552-3098. doi : 10.1109/TRO.2020.3043723.

K. Wu, J. Li, H. Zhao, and Y. Zhong. Review of Industrial Robot Stiffness Identification and Modelling. *Applied Sciences*, 12(17) :8719, aug 2022. ISSN 2076-3417. doi : 10.3390/app12178719.

L. Zollo, B. Siciliano, A. De Luca, E. Guglielmelli, and P. Dario. Compliance Control for an Anthropomorphic Robot with Elastic Joints : Theory and Experiments. *Journal of Dynamic Systems, Measurement, and Control*, 127(3) :321–328, sep 2005. ISSN 0022-0434. doi : 10.1115/1.1978911.

Conclusion

Cette thèse avait pour objectif l'élaboration d'une méthode de proprioception alternative pour les manipulateurs robotiques sériels, ainsi que la conception de méthodes de commande mettant à profit cette rétroaction supplémentaire. Dans un contexte de collaboration humain-robot et, plus spécifiquement, d'interaction physique humain-robot, cela permet d'envisager un paradigme de conception différent, menant à des manipulateurs intrinsèquement plus sécuritaires grâce à leur masse réduite et à leur flexiblité.

Le premier chapitre a permis de présenter la solution proposée et de démontrer sa faisabilité technique. Cette solution est une chaîne de mesure passive disposée en parallèle avec le manipulateur. Des lignes directrices ont été élaborées dans le but de contourner les obstacles de conception découlant de la cinématique. Ces lignes directrices sont, notamment, l'utilisation de la redondance cinématique et la fixation de la base de la chaîne de mesure sur le premier corps mobile du robot. La fabrication mécanique d'un prototype a finalement achevé de démontrer la faisabilité technique du dispositif avec les moyens technologiques actuels. Grâce à cette nouvelle source de rétroaction, un schéma de commande de la position réelle du manipulateur a pu être élaboré. Cette méthode de commande a été validée en simulation et également de manière expérimentale, avec un prototype de manipulateur léger.

Le second chapitre a exploré l'idée de se servir de la mesure de la position réelle d'un manipulateur pour transformer le défaut apparent de la déformation structurelle en avantage pour l'interaction physique humain-robot. Cette méthode exploite le découplage entre l'inertie réflétée des membrures et des actionneurs. Ainsi, il a été possible de créer une méthode de commande simple où la consigne de vitesse envoyée aux actionneurs correspond à la vitesse cartésienne mesurée, puis rapportée dans l'espace articulaire. Cela permet notamment à un humain de guider le robot par des mouvements libres nécessitant de faibles forces d'interaction, par rapport à une solution commerciale connue. La méthode, qui ne requiert par ailleurs aucun capteur d'effort, permet également à un opérateur d'interagir à n'importe quel endroit sur le robot.

Le troisième chapitre a repris l'idée de tirer profit de la déformation du robot, mais, dans ce cas-ci, dans une perspective de commande de la force d'interaction. Pour y arriver, le cadre théorique des actionneurs à élasticité en série (SEA) a été généralisé à la commande des

manipulateurs flexibles. Le modèle de raideur du manipulateur a été obtenu par la méthode des articulations virtuelles, avec des éléments de raideur localisés. Grâce à ce modèle de raideur, la force d'interaction (non colocalisée) peut être indirectement asservie par la commande des vitesses colocalisées. Cela permet notamment de reproduire le comportement dynamique d'un ressort à l'organe terminal. Finalement, la méthode de commande a été validée sur le montage expérimental. Le manipulateur flexible a ainsi été en mesure de reproduire des raideurs cartésiennes commandées avec des valeurs découplées dans chaque direction.

Les principales limitations d'un tel système ont été abordées au chapitre 3. Notamment, il convient de rappeler que la raideur simulée par le robot ne peut excéder sa raideur intrinsèque pour respecter le critère de passivité. Ce résultat a par ailleurs été développé en plusieurs dimensions pour la première fois, menant à une interprétation intuitive par les ellipsoïdes de raideur. De plus, à haute fréquence, le comportement dynamique du robot lors de l'interaction revient à sa raideur intrinsèque. Autrement dit, le comportement dynamique commandé n'est applicable que jusqu'à une certaine fréquence critique.

Les travaux présentés dans cet ouvrage sont un premier pas et les réponses apportées soulèvent naturellement presque autant de questions. Concrètement, il pourrait être pertinent d'analyser plus formellement la dynamique d'un robot flexible asservi par la méthode proposée dans une bande de fréquences plus large que celle associée à l'interaction humain-robot, qui demeure relativement étroite. Par exemple, bien que la limite théorique de raideur simulable soit la même que celle d'un SEA, il pourrait être pertinent d'évaluer si, en pratique, un manipulateur complet pourrait être encore plus limité, à cause de sa dynamique plus complexe.

Plus largement, les travaux présentés posent d'autres questions intéressantes. Notamment, est-il intéressant ou pertinent de combiner flexibilité et actionnement direct ou quasi-direct ? Certes, ces actionneurs permettent d'estimer le couple à leur sortie, mais la flexiblité nous empêche alors d'en déduire directement des efforts résultants à l'organe terminal. Autrement dit, en termes mathématiques, la solution idéale, si elle existe, est-elle l'intersection ou la différence symétrique de ces deux ensembles ?

Finalement, d'un point de vue plus large encore, il est intéressant de se questionner sur l'existence, dans notre façon de concevoir les robots, de caractéristiques supplémentaires ayant l'apparence de défauts, mais derrière lesquelles se cacherait une fonctionnalité insoupçonnée, pour peu que l'on y réfléchisse. À ce chapitre, sur une note plus légère, nous aurions potentiellement beaucoup à apprendre du domaine de l'ingénierie logicielle, où cette philosophie est célébrée depuis déjà fort longtemps.

Bibliographie générale

S. L. Aaron and R. B. Stein. Comparison of an EMG-controlled prosthesis and the normal human biceps brachii muscle. *American journal of physical medicine*, 55(1) :1–14, feb 1976. ISSN 0002-9491.

M. Abdallah, A. Chen, A. Campeau-Lecours, and C. Gosselin. How to reduce the impedance for pHRI : Admittance control or underactuation ? *Mechatronics*, 84 :102768, jun 2022. ISSN 09574158. doi : 10.1016/j.mechatronics.2022.102768.

E. Abele, S. Rothenbücher, and M. Weigold. Cartesian compliance model for industrial robots using virtual joints. *Production Engineering*, 2(3) :339–343, sep 2008. ISSN 0944-6524. doi : 10.1007/s11740-008-0118-0.

T. Berger and L. Lanza. Output tracking for a non-minimum phase robotic manipulator. *IFAC-PapersOnLine*, 54(9) :178–185, 2021. ISSN 24058963. doi : 10.1016/j.ifacol.2021.06.074.

G. Boucher, T. Laliberté, and C. Gosselin. Mechanical Design of a Low-Impedance 6-Degree-of-Freedom Displacement Sensor for Intuitive Physical Human–Robot Interaction. *Journal of Mechanisms and Robotics*, 13(2), apr 2021. ISSN 1942-4302. doi : 10.1115/1.4049191.

S. R. Buss and J.-S. Kim. Selectively Damped Least Squares for Inverse Kinematics. *Journal of Graphics Tools*, 10(3) :37–49, jan 2005. ISSN 1086-7651. doi : 10.1080/2151237X.2005.10129202.

A. Calanca, R. Muradore, and P. Fiorini. Impedance control of series elastic actuators : Passivity and acceleration-based control. *Mechatronics*, 47 :37–48, nov 2017. ISSN 09574158. doi : 10.1016/j.mechatronics.2017.08.010.

A. Calanca, E. Dimo, R. Vicario, P. Fiorini, M. Serpelloni, and G. Legnani. Introducing Series Elastic Links for Affordable Torque-Controlled Robots. *IEEE Robotics and Automation Letters*, 4(1) :137–144, jan 2019. ISSN 2377-3766. doi : 10.1109/LRA.2018.2878353.

A. Calanca, E. Sartori, and B. Maris. Force control of lightweight series elastic systems using enhanced disturbance observers. *Robotics and Autonomous Systems*, 164 :104407, jun 2023. ISSN 09218890. doi : 10.1016/j.robot.2023.104407.

R. H. Cannon and E. Schmitz. Initial Experiments on the End-Point Control of a Flexible One-Link Robot. *The International Journal of Robotics Research*, 3(3) :62–75, sep 1984. ISSN 0278-3649. doi : 10.1177/027836498400300303.

P. Cardou, S. Bouchard, and C. Gosselin. Kinematic-sensitivity indices for dimensionally nonhomogeneous jacobian matrices. *IEEE Transactions on Robotics*, 26(1) :166–173, feb 2010. doi : 10.1109/TRO.2009.2037252.

A. Chen, R. Yin, L. Cao, C. Yuan, H. Ding, and W. Zhang. Soft robotics : Definition and research issues. In *2017 24th International Conference on Mechatronics and Machine Vision in Practice (M2VIP)*, pages 366–370. IEEE, nov 2017. ISBN 978-1-5090-6546-2. doi : 10.1109/M2VIP.2017.8267170.

T. Cvitanic, S. Melkote, and S. Balakirsky. Improved state estimation of a robot end-effector using laser tracker and inertial sensor fusion. *CIRP Journal of Manufacturing Science and Technology*, 38 :51–61, aug 2022. ISSN 17555817. doi : 10.1016/j.cirpj.2022.03.011.

A. De Luca and W. J. Book. Robots with Flexible Elements. In Siciliano Bruno, , and O. Khatib, editors, *Springer Handbook of Robotics*, pages 243–282. Springer International Publishing, Cham, 2016. doi : 10.1007/978-3-319-32552-1_11.

A. De Luca and B. Siciliano. An asymptotically stable joint PD controller for robot arms with flexible links under gravity. In *[1992] Proceedings of the 31st IEEE Conference on Decision and Control*, pages 325–326. IEEE, 1992. ISBN 0-7803-0872-7. doi : 10.1109/CDC.1992.371728.

A. De Santis, B. Siciliano, A. De Luca, and A. Bicchi. An atlas of physical human–robot interaction. *Mechanism and Machine Theory*, 43(3) :253–270, mar 2008. ISSN 0094114X. doi : 10.1016/j.mechmachtheory.2007.03.003.

N. Dehio, J. Smith, D. L. Wigand, P. Mohammadi, M. Mistry, and J. J. Steil. Enabling impedance-based physical human–multi–robot collaboration : Experiments with four torque-controlled manipulators. *The International Journal of Robotics Research*, 41(1) :68–84, jan 2022. ISSN 0278-3649. doi : 10.1177/02783649211053650.

C. Della Santina. Flexible Manipulators. In *Encyclopedia of Robotics*, pages 1–15. Springer Berlin Heidelberg, Berlin, Heidelberg, 2021. doi : 10.1007/978-3-642-41610-1_182-1.

D. Feliu-Talegon and V. Feliu-Batlle. Control of Very Lightweight 2-DOF Single-Link Flexible Robots Robust to Strain Gauge Sensor Disturbances : A Fractional-Order Approach. *IEEE Transactions on Control Systems Technology*, 2021. doi : 10.1109/TCST.2021.3053857.

J. P. W. Flemming. Monitoring the location of a robot hand. U.S. Patent 4119212A, jul 1977.

X. Garant and C. Gosselin. Noncollocated Proprioceptive Sensing for Lightweight Flexible Robotic Manipulators. *IEEE/ASME Transactions on Mechatronics*, pages 1–12, 2023. ISSN 1083-4435. doi : 10.1109/TMECH.2023.3263108.

P. L. García, S. Crispel, E. Saerens, T. Verstraten, and D. Lefeber. Compact Gearboxes for Modern Robotics : A Review. *Frontiers in Robotics and AI*, 7 :103, aug 2020. ISSN 2296-9144. doi : 10.3389/frobt.2020.00103.

D. V. Gealy, S. McKinley, B. Yi, P. Wu, P. R. Downey, G. Balke, A. Zhao, M. Guo, R. Thomasson, A. Sinclair, P. Cuellar, Z. McCarthy, and P. Abbeel. Quasi-direct drive for low-cost compliant robotic manipulation. *Proceedings - IEEE International Conference on Robotics and Automation*, 2019-May :437–443, may 2019. doi : 10.1109/ICRA.2019.8794236.

S. Gong. A novel ultra-precision integrated robotic system. *Robotica*, 23(4) :501–513, jul 2005. ISSN 0263-5747. doi : 10.1017/S0263574704001171.

A. Grädener and L. Rokeach. Arrangement for an articulated arm robot and method for determining the positioning of a mount for an end effector of an articulated arm robot. International Patent WO2019011381A1, jan 2019.

S. Haddadin and E. Croft. Physical Human–Robot Interaction. In O. Siciliano Bruno and Khatib, editor, *Springer Handbook of Robotics*, pages 1835–1874. Springer International Publishing, Cham, 2016. ISBN 978-3-319-32552-1. doi : 10.1007/978-3-319-32552-1_69.

S. Haddadin, A. Albu-Schaffer, and G. Hirzinger. The role of the robot mass and velocity in physical human-robot interaction - Part I : Non-constrained blunt impacts. In *2008 IEEE International Conference on Robotics and Automation*, pages 1331–1338. IEEE, may 2008. ISBN 978-1-4244-1646-2. doi : 10.1109/ROBOT.2008.4543388.

S. Haddadin, K. Krieger, N. Mansfeld, and A. Albu-Schaffer. On impact decoupling properties of elastic robots and time optimal velocity maximization on joint level. In *2012 IEEE/RSJ International Conference on Intelligent Robots and Systems*, pages 5089–5096. IEEE, oct 2012. ISBN 978-1-4673-1736-8. doi : 10.1109/IROS.2012.6385913.

T. Horibe, E. Treadway, and R. B. Gillespie. Comparing Series Elasticity and Admittance Control for Haptic Rendering. pages 240–250. 2016. doi : 10.1007/978-3-319-42321-0_22.

M. Hussein. A review on vision-based control of flexible manipulators. *Advanced Robotics*, 29 (24) :1575–1585, dec 2015. doi : 10.1080/01691864.2015.1078743.

A. Q. Keemink, H. van der Kooij, and A. H. Stienen. Admittance control for physical human–robot interaction. *The International Journal of Robotics Research*, 37(11) :1421–1444, sep 2018. ISSN 0278-3649. doi : 10.1177/0278364918768950.

C. U. Kenanoglu and V. Patoglu. A Fundamental Limitation of Passive Spring Rendering With Series Elastic Actuation. *IEEE Transactions on Haptics*, pages 1–6, 2023. ISSN 1939-1412. doi : 10.1109/TOH.2023.3260063.

O. T. Kenanoglu, C. U. Kenanoglu, and V. Patoglu. Effect of Low-Pass Filtering on Passivity and Rendering Performance of Series Elastic Actuation. *IEEE Transactions on Haptics*, pages 1–6, 2023. ISSN 1939-1412. doi : 10.1109/TOH.2023.3273168.

J. Khanna. Criterion for selecting stiffness matrices. *AIAA Journal*, 3(10) :1976–1976, oct 1965. ISSN 0001-1452. doi : 10.2514/3.3303.

J. Khanna and R. F. Hooley. Comparison and evaluation of stiffness matrices. *AIAA Journal*, 4(12) :2105–2111, dec 1966. ISSN 0001-1452. doi : 10.2514/3.3862.

C. T. Kiang, A. Spowage, and C. K. Yoong. Review of Control and Sensor System of Flexible Manipulator. *Journal of Intelligent & Robotic Systems*, 77(1) :187–213, jan 2015. ISSN 0921-0296. doi : 10.1007/s10846-014-0071-4.

A. Klimchik, B. Furet, S. Caro, and A. Pashkevich. Identification of the manipulator stiffness model parameters in industrial environment. *Mechanism and Machine Theory*, 90 :1–22, aug 2015. ISSN 0094114X. doi : 10.1016/j.mechmachtheory.2015.03.002.

T. Laliberté and C. Gosselin. Low-Impedance Displacement Sensors for Intuitive Physical Human–Robot Interaction : Motion Guidance, Design, and Prototyping. *IEEE Transactions on Robotics*, 38(3) :1518–1530, jun 2022. ISSN 1552-3098. doi : 10.1109/TRO.2021.3121610.

H. Lee, J.-H. Ryu, J. Lee, and S. Oh. Passivity Controller Based on Load-Side Damping Assignment for High Stiffness Controlled Series Elastic Actuators. *IEEE Transactions on Industrial Electronics*, 68(1) :871–881, jan 2021. ISSN 0278-0046. doi : 10.1109/TIE.2020.3013751.

K. Li, H. Wang, X. Liang, and Y. Miao. Visual Servoing of Flexible-Link Manipulators by Considering Vibration Suppression Without Deformation Measurements. *IEEE Transactions on Cybernetics*, 52(11) :12454–12463, nov 2022. ISSN 2168-2267. doi : 10.1109/TCYB.2021.3072779.

D. P. Losey and M. K. O'Malley. Effects of discretization on the K-width of series elastic actuators. In *2017 IEEE International Conference on Robotics and Automation (ICRA)*, pages 421–426. IEEE, may 2017. ISBN 978-1-5090-4633-1. doi : 10.1109/ICRA.2017.7989054.

D. P. Losey, C. G. McDonald, E. Battaglia, and M. K. O'Malley. A Review of Intent Detection, Arbitration, and Communication Aspects of Shared Control for Physical Human–Robot Interaction. *Applied Mechanics Reviews*, 70(1), jan 2018. ISSN 0003-6900. doi : 10.1115/1.4039145.

J. Malzahn and T. Bertram. Collision Detection and Reaction for a Multi-Elastic-Link Robot Arm. *IFAC Proceedings Volumes*, 47(3) :320–325, 2014. ISSN 14746670. doi : 10.3182/20140824-6-ZA-1003.01545.

J. Malzahn, R. Schloss, and T. Bertram. Link elasticity exploited for payload estimation and force control. In *2015 IEEE/RSJ International Conference on Intelligent Robots and Systems (IROS)*, pages 1508–1513. IEEE, sep 2015. ISBN 978-1-4799-9994-1. doi : 10.1109/IROS.2015.7353567.

U. Mengilli, Z. O. Orhan, U. Caliskan, and V. Patoglu. Passivity of Series Damped Elastic Actuation under Velocity-Sourced Impedance Control. In *2021 IEEE World Haptics Conference (WHC)*, pages 379–384. IEEE, jul 2021. ISBN 978-1-6654-1871-3. doi : 10.1109/WHC49131.2021.9517159.

K. Merckaert, A. De Beir, N. Adriaens, I. El Makrini, R. Van Ham, and B. Vanderborght. Independent load carrying and measurement manipulator robot arm for improved payload to mass ratio. *Robotics and Computer-Integrated Manufacturing*, 53 :135–140, oct 2018. ISSN 0736-5845. doi : 10.1016/J.RCIM.2018.04.001.

F. Muller, J. Jakel, J. Suchy, and U. Thomas. Stability of Nonlinear Time-Delay Systems Describing Human–Robot Interaction. *IEEE/ASME Transactions on Mechatronics*, 24(6) : 2696–2705, dec 2019. ISSN 1083-4435. doi : 10.1109/TMECH.2019.2939907.

J. Oliveira, A. Ferreira, and J. C. Reis. Design and experiments on an inflatable link robot with a built-in vision sensor. *Mechatronics*, 65 :102305, feb 2020. ISSN 09574158. doi : 10.1016/j.mechatronics.2019.102305.

C. Ott. Modeling of Flexible Joint Robots. In *Cartesian Impedance Control of Redundant and Flexible-Joint Robots*, pages 13–27. Springer Berlin Heidelberg, Berlin, Heidelberg, 2008. doi : 10.1007/978-3-540-69255-3_2.

G. Pratt and M. Williamson. Series elastic actuators. In *Proceedings 1995 IEEE/RSJ International Conference on Intelligent Robots and Systems. Human Robot Interaction and Cooperative Robots*, volume 1, pages 399–406. IEEE Comput. Soc. Press, 1995. ISBN 0-8186-7108-4. doi : 10.1109/IROS.1995.525827.

G. Pratt, P. Willisson, C. Bolton, and A. Hofman. Late motor processing in low-impedance robots : impedance control of series-elastic actuators. In *Proceedings of the 2004 American Control Conference*, pages 3245–3251 vol.4. IEEE, 2004. ISBN 0-7803-8335-4. doi : 10.23919/ACC.2004.1384410.

M. Safeea, P. Neto, and R. Bearee. Precise hand-guiding of redundant manipulators with null space control for in-contact obstacle navigation. In *IECON 2019 - 45th Annual Conference*

of the IEEE Industrial Electronics Society, pages 693–698. IEEE, oct 2019. ISBN 978-1-7281-4878-6. doi : 10.1109/IECON.2019.8927766.

U. K. Sahu, D. Patra, and B. Subudhi. Vision-based tip position tracking control of two-link flexible manipulator. *IET Cyber-Systems and Robotics*, 2(2) :53–66, jun 2020. ISSN 2631-6315. doi : 10.1049/iet-csr.2019.0035.

M. Sayahkarajy, Z. Mohamed, and A. A. Mohd Faudzi. Review of modelling and control of flexible-link manipulators. *Proceedings of the Institution of Mechanical Engineers, Part I : Journal of Systems and Control Engineering*, 230(8) :861–873, sep 2016. ISSN 0959-6518. doi : 10.1177/0959651816642099.

J. Sensinger and R. Ff. Weir. Improvements to Series Elastic Actuators. In *2006 2nd IEEE/ASME International Conference on Mechatronics and Embedded Systems and Applications*, pages 1–7. IEEE, aug 2006. ISBN 0-7803-9721-5. doi : 10.1109/MESA.2006.296927.

A. H. Slocum. Mechanism to determine position and orientation in space. U.S. Patent 4606696A, jun 1984.

P. Staufer and H. Gattringer. State estimation on flexible robots using accelerometers and angular rate sensors. *Mechatronics*, 22(8) :1043–1049, dec 2012. ISSN 0957-4158. doi : 10.1016/J.MECHATRONICS.2012.08.009.

T. Steinecker, A. Kurdas, N. Mansfeld, M. Hamad, R. J. Kirschner, S. Abdolshah, and S. Haddadin. Mean Reflected Mass : A Physically Interpretable Metric for Safety Assessment and Posture Optimization in Human-Robot Interaction. In *2022 International Conference on Robotics and Automation (ICRA)*, pages 11209–11215. IEEE, may 2022. ISBN 978-1-7281-9681-7. doi : 10.1109/ICRA46639.2022.9811582.

D. Subedi, I. Tyapin, and G. Hovland. Review on Modeling and Control of Flexible Link Manipulators. *Modeling, Identification and Control : A Norwegian Research Bulletin*, 41 (3) :141–163, 2020. ISSN 0332-7353. doi : 10.4173/mic.2020.3.2.

D. Subedi, T. N. Aune, I. Tyapin, and G. Hovland. Static Deflection Compensation of Multi-Link Flexible Manipulators Under Gravity. *IEEE Access*, 10 :9658–9667, 2022. ISSN 21693536. doi : 10.1109/ACCESS.2022.3144404.

B. Subudhi and A. Morris. Dynamic modelling, simulation and control of a manipulator with flexible links and joints. *Robotics and Autonomous Systems*, 41(4) :257–270, dec 2002. ISSN 09218890. doi : 10.1016/S0921-8890(02)00295-6.

N. L. Tagliamonte and D. Accoto. Passivity constraints for the impedance control of series elastic actuators. *Proceedings of the Institution of Mechanical Engineers, Part I : Journal of Systems and Control Engineering*, 228(3) :138–153, mar 2014. ISSN 0959-6518. doi : 10.1177/0959651813511615.

M. Teyssier, B. Parilusyan, A. Roudaut, and J. Steimle. Human-Like Artificial Skin Sensor for Physical Human-Robot Interaction. In *2021 IEEE International Conference on Robotics and Automation (ICRA)*, pages 3626–3633. IEEE, may 2021. ISBN 978-1-7281-9077-8. doi : 10.1109/ICRA48506.2021.9561152.

F. E. Tosun and V. Patoglu. Necessary and Sufficient Conditions for the Passivity of Impedance Rendering With Velocity-Sourced Series Elastic Actuation. *IEEE Transactions on Robotics*, 36(3) :757–772, jun 2020. ISSN 1552-3098. doi : 10.1109/TRO.2019.2962332.

S. Toxiri, A. Calanca, J. Ortiz, P. Fiorini, and D. G. Caldwell. A Parallel-Elastic Actuator for a Torque-Controlled Back-Support Exoskeleton. *IEEE Robotics and Automation Letters*, 3 (1) :492–499, jan 2018. ISSN 2377-3766. doi : 10.1109/LRA.2017.2768120.

E. Treadway, Y. Yang, and R. B. Gillespie. Decomposing the performance of admittance and series elastic haptic rendering architectures. In *2017 IEEE World Haptics Conference (WHC)*, pages 346–351. IEEE, jun 2017. ISBN 978-1-5090-1425-5. doi : 10.1109/WHC.2017.7989926.

S. Tso, T. Yang, W. Xu, and Z. Sun. Vibration control for a flexible-link robot arm with deflection feedback. *International Journal of Non-Linear Mechanics*, 38(1) :51–62, jan 2003. ISSN 0020-7462. doi : 10.1016/S0020-7462(01)00040-3.

H. Vallery, J. Veneman, E. van Asseldonk, R. Ekkelenkamp, M. Buss, and H. van Der Kooij. Compliant actuation of rehabilitation robots. *IEEE Robotics & Automation Magazine*, 15 (3) :60–69, sep 2008. ISSN 1070-9932. doi : 10.1109/MRA.2008.927689.

K. Wen, T. S. Nguyen, D. Harton, T. Laliberté, and C. Gosselin. A Backdrivable Kinematically Redundant (6+3)-Degree-of-Freedom Hybrid Parallel Robot for Intuitive Sensorless Physical Human–Robot Interaction. *IEEE Transactions on Robotics*, 37(4) :1222–1238, aug 2021. ISSN 1552-3098. doi : 10.1109/TRO.2020.3043723.

K. Wu, J. Li, H. Zhao, and Y. Zhong. Review of Industrial Robot Stiffness Identification and Modelling. *Applied Sciences*, 12(17) :8719, aug 2022. ISSN 2076-3417. doi : 10.3390/app12178719.

S. Yamada and H. Fujimoto. Position-based High Backdrivable Control Using Load-side Encoder and Backlash. *IEEJ Journal of Industry Applications*, 10(2) :142–152, mar 2021. ISSN 2187-1094. doi : 10.1541/ieejjia.20004583.

L. Zollo, B. Siciliano, A. De Luca, E. Guglielmelli, and P. Dario. Compliance Control for an Anthropomorphic Robot with Elastic Joints : Theory and Experiments. *Journal of Dynamic Systems, Measurement, and Control*, 127(3) :321–328, sep 2005. ISSN 0022-0434. doi : 10.1115/1.1978911.